Chemical and Physical Methods of the Templated Direction of Block Copolymers

By

Samuel M. Nicaise

B.S. Electrical Engineering
University of Kentucky, 2010

SUBMITTED TO THE DEPARTMENT OF ELECTRICAL ENGINEERING AND COMPUTER SCIENCE IN PARTIAL FULFILLMENT OF THE REQUIREMENTS FOR THE DEGREE OF

MASTER OF SCIENCE IN ELECTRICAL ENGINEERING
AT THE
MASSACHUSETTS INSTITUTE OF TECHNOLOGY

SEPTEMBER 2012

© 2012 Massachusetts Institute of Technology. All rights reserved.

ARCHIVES
MASSACHUSETTS INSTITUTE OF TECHNOLOGY
OCT 24 2012
LIBRARIES

The author hereby grants to MIT permission to reproduce
and to distribute publicly paper and electronic
copies of this thesis document in whole or in part
in any medium now known or hereafter created.

Signature of Author: ______________________________

Department of Electrical Engineering and Computer Science
August 31, 2012

Certified by: ______________________________

Karl K. Berggren
Associate Professor of Electrical Engineering
Thesis Supervisor

Accepted by: ______________________________

Professor Leslie A. Kolodziejski
Professor of Electrical Engineering and Computer Science
Chairman of the Committee on Graduate Students

Chemical and Physical Methods of the Templated Direction of Block Copolymers

by

Samuel M. Nicaise

Submitted to the Department of Electrical Engineering and Computer Science on 31 August, 2012, in partial fulfillment of the requirements for the degree of Master of Science in Electrical Engineering at the Massachusetts Institute of Technology

Abstract

This thesis discusses the investigation of various aspects of templated self-assembly of block copolymer (BCP) thin films for nanofeature fabrication. Two chapters outline the research of a combined physical and chemical templating method with two BCPs. The method was not effective in templating poly(styrene-block-methyl methacrylate) (PS-b-PMMA) BCP because of limited template wettability. The method effectively templated poly(octofluro pentamethacrylate-block-hydroxystyrene) (OFPMA-b-HSM) BCP to fabricate orthogonally-directed lamellar microdomains and nanohole-mesh arrays. Chapter 4 discusses the achievement of a mean overlay accuracy of 52 nm and 0° for two electron-beam-based lithographic features as a result of an investigated overlay process. Lastly, the thesis reports the fabrication of a wide-range of nanofeatures – from two-dimensional and three dimensional nanoholes arrays to elliptical and cylindrical meshes – by the sacrificial-post templating method with poly(styrene-block-dimethylsiloxane) (PS-b-PDMS) BCP.

Thesis Supervisor: Prof. Karl K. Berggren

Title: Associate Professor of Electrical Engineering

Acknowledgements

The funding for this thesis work was provided by the DuPont-MIT Alliance, NSF Graduate Research Fellowship Program, MIT Energy Initiative, Semiconductor Research Alliance, and Taiwan Semiconductor Manufacturing Corporation.

This thesis was 2 years of hard, interesting, hair-pulling, and enlightening work. It didn't happen at my hands alone, and required significant input from a large number of other people. To all of them I give considerable thanks and appreciation. Upon the shoulders of giants science sits, and those who perform science are also built only on the foundation of those who support the development of those scientists.

Karl, you have been incredibly important in this process. Your insight never ceases to amaze me and you've had my back at every turn of the process. Not only have you supported my research pursuits, but also your guidance has helped me develop as a student and a professional.

Much thanks to my other professional role models including, but not limited to, Caroline Ross, Ted Fedynyshyn, Hank Smith, Jim Dailey, and Mark Mondol. You have been incredibly open and supportive through every step of the process. Furthermore, all of the teachers of my classes at MIT have been stellar and kept me academically on track.

A special thanks to all of my research "peers", a collection of extremely knowledgeable researchers. I depended on your intuition, past failures, headaches, and successes. Especially, I cannot thank you enough Amir. Though we didn't always agree, you were one of my most important support beams through this thesis, and I owe you considerably. Beyond Amir, all my friends in the QNN Group and NSL are awesome. You made me realize that I am not in this alone. Lastly, Mauro, you made a hard day easy and a down day up.

Outside of the lab so many friends have made my experience at MIT envious. I absolutely love the comfort and camaraderie of my roommates and cats at Pleasant House. The down-to-earth nature of the Arlington/UMass-Amherst crew is so relaxing. All of my classmates in EECS and around the MIT

campus are way too fun. And of course, the cyclists and triathletes at MIT...without you people, I would have quit MIT long ago. You keep me sane and motivated on a daily basis.

Mom and Dad, you are everything to me. All 356 day so of the year I am grateful for how you raised me and the model you have provided. As hard as it is to be geographically so far away from you, I know that you are so proud of me which gives me energy to keep going. Now...if only I could convince you to retire and come to Boston ;)

List of Contents

Chapter 1: Introduction: Block Copolymer Thin Films and their Templated Self-Assembly

1.1 Block Copolymer Thin Films....16

1.2 Templated Self Assembly of BCPs....18

1.3 Electron Beam Lithography....23

1.4 Prior Work....27

1.5 Objectives and Challenges....28

1.6 Applications....28

1.7 Overview of Thesis Work....29

References....30

Chapter 2: Multiple Surface Energy Substrates for PS-b-PMMA Self-Assembly

2.1 PS-b-PMMA Self-Assembly with Surface Energy Modification....33

2.2 Single-SAM Sample Modification for PS-b-PMMA Self-Assembly....39

2.3 Multiple-SAM Sample Modification for PS-b-PMMA Self-Assembly....43

2.4 Conclusions....47

References....49

Chapter 3: Assembly and Direction of a High-χ Polymer

3.1 Discussion of High-χ....51

3.2 Description of Synthesized Polymers....52

3.3 Thermal Annealing....56

3.4 Chemical Templating....58

3.5 Physical Templating....60

3.6 Summary and Conclusion....66

References....67

Chapter 4: Lithographic Overlay of Negative-tone Resist Features

4.1 Combined Templating Objective....68

4.2 Investigation of Overlay....................69

4.3 Process Description....................70

4.4 Results....................73

4.5 Conclusions....................76

References....................77

Chapter 5: Sacrificial Templates PS-b-PDMS Self-Assembly

5.1 Prior work: DSA of PS-b-PDMS....................78

5.2 Processing Steps....................79

5.3 PMMA Resist....................80

5.4 Templating for 2D Nanostructures....................82

5.5 Templating for 3D Nanostructures....................87

5.6 Conclusions....................88

References....................90

Appendix I: Contrast Measurement of Neon-Ion-Beam-Lithography with Hydrogen Silsesquioxane

A.1 Background....................91

A.2 Results....................91

A.3 Discuss....................93

A.4 Summary....................93

References....................95

List of Figures

Chapter 1: Introduction: Block Copolymer Thin Films and their Templated Self-Assembly

1.1 Cartoons of different polymers and interaction as BCP..............................17

1.2 Schematics of different morphologies of BCP..18

1.3 Phase (or morphology) diagram for conventional BCPs showing the position of different morphologies hography...18

1.4 Cartoon showing the BCP natural pitch, L_0..19

1.5 SEMs of thin films of BCP on Si substrates..20

1.6 Schematics of physical and chemical templates of substrates.......................21

1.7 Schematics of the template preferentiality with respect to different polymer blocks..22

1.8 Schematics and scanning-electron-micrograph of templates exemplifying the commensurate condition..23

1.9 Schematics of pattern transfer with BCP...24

1.10 Schematic for fabrication process of negative-tone lithographic features..25

1.11 Schematic of SEBL microscope column...26

1.12 Resist Remaining vs. Dose Delivered curve..27

Chapter 2: Multiple Surface Energy Substrates for PS-b-PMMA Self-Assembly

2.1 Schematic diagram of poly(styrene-b-methylmethacrylate)................. 33

2.2 Schematics of self-assembled monolayers..35

2.3 Top- and side-view of an ideal example combined templating method...37

2.4 Major steps of the fabrication process. 38

2.5 Microscope image of a water droplet on a sample in the goniometer...39

2.6 HSQ Posts fallen over and standing on a substrate...................................40

2.7 SEMs of PS-block of PS-b-PMMA on SAM-coated Si substrate...............43

2.8 Top-down scanning electron micrograph of templated PS-b-PMMA BCP with the single SAM system of BTS........44

2.9 Top-down scanning electron micrographs of PS-block of PS-b-PMMA on SAM-coated Si substrate........46

2.10 Scanning-electron micrographs of PS-block of PS-b-PMMA on SAM-coated Si substrate........47

2.11 Scanning-electron micrographs of PS-block of PS-b-PMMA on SAM-coated Si substrate........47

2.12 SEMs of templated PS-b-PMMA BCP self-assembly with various different templating schemes........48

Chapter 3: Assembly and Direction of a High-χ Polymer

3.1 Major Steps of the fabrication process........55

3.2 Top-down scanning-electron micrographs of ObAL60 BCP after different methacrylate-block removal steps........57

3.3 Top-down scanning-electron micrograph of ObAL60 BCP for different ramp-down times during thermal annealing........58

3.4 Scanning-electron micrographs of self-assembled thin films of all synthesized BCPs and measurements of the BCP nature pitches (L_0)........59

3.5 Schematic of line grating array used for chemical templating........60

3.6 Scanning-electron micrograph of ObAL60 templated by a chemical line grating array as outlined in red........61

3.7 Schematics of template schemes (a) line-grating array and (b) dot array........62

3.8 Scanning-electron micrographs of ObAL60 with HSQ physical templates........63

3.9 Scanning-electron micrographs of BCPs templated by various physical templates........64

3.10 Top-down scanning-electron micrographs of ObAL80 and ObAL50 templated by short HSQ post-arrays........65

3.11 Top-down scanning-electron micrographs of BCPs templated by various

physical templates..........66

3.12 Top-down scanning-electron micrographs of BCPs templated by various physical templates..........67

Chapter 4: Lithographic Overlay of Negative-tone Resist Features

4.1 Schematic of a double pattern of combined chemical and physical templating..........70

4.2 Schematics of the first and second write-patterns, and common overlay errors..........71

4.3 Major steps of the fabrication process..........72

4.4 Snapshot of the design for the first and second writes..........73

4.5 Top-down scanning-electron micrograph example of an overlay of the first and second write patterns in HSQ without process improvements..........75

4.6 Top-down scanning-electron micrograph examples of overlays of the first and second writes in HSQ after process improvements..........76

Chapter 5: Sacrificial Templates PS-b-PDMS Self-Assembly

5.1 Major Steps of the fabrication process..........81

5.2 Top-down scanning electron micrographs of PMMA post features..........82

5.3 Top-down scanning electron micrograph of a final BCP nanopattern from hexagonal post template arrays..........83

5.4 Top-down scanning electron micrographs of different 2D nanopatterns formed by the sacrificial-post templating method..........84

5.5 Top-down scanning electron micrograph of hexagonal array of nanholes formed by the sacrificial-post templating method..........85

5.6 Top-down scanning electron micrographs of different 2D nanopatterns formed by the sacrificial-post templating method..........85

5.7 Graph of nanohole diameter versus post diameter and pitch..........86

5.8 Examples of Matlab steps for determining the size of a-c) generated-holes and d-f) post-holes..........87

5.9 Top-down scanning electron micrographs of 3D nanoholes meshes templated by the sacrificial-post templating method..........89

Appendix I: Contrast Measurement of Neon-Ion-Beam-Lithography with Hydrogen Silsesquioxane

A1 Measurements of the height of HSQ remaining for an example pad feature....................93

A2 Height of HSQ remaining as a function of areal dose density..................94

List of Tables

2.1 List of the SAMs used in the presented results..36

2.2 Contact angle measurements for a number of different processing conditions..42

2.3 Contact angle measurements for a number of different processing conditions..45

3.1 List of common and of-interest homopolymers and their respective measured surface energies..53

3.2 Characteristics of the different synthesized BCPs.....................................54

Chapter 1: Introduction: Block Copolymer Thin Films and their Templated Self-Assembly

This thesis summarizes a number of experiments related to templated self-assembly (TSA) of block copolymers (BCPs). The immediate impact of TSA of BCPs is on the science and industry of nanofabrication. Nanofabrication involves the understanding, design, and fabrication of nanoscale patterns, structures, objects and devices. Nanofabrication is important to a variety of different applications, including, but not limited to, nanoelectronics, energy devices, biosensing, plasmonics, nano-electronic and mechanical systems (NEMS) and surface energy engineering[1-6]. Fabrication at the nanoscale is typically carried out in a top-down manner. An example of top-down includes the making the material on the top of a substrate into a particular pattern based on a design. The patterning for this design is typically input from an external machine or system, as opposed to generated from within the material. Alternatively, fabrication at the nanoscale can also be carried out from the bottom up. In this manner, the design evolves from a certain more homogenous material to a structure that has more organization (eg. spatial organization with more periodization, long-range order, or locally complex shapes). Self-assembly is a type of bottom-up nanofabrication. Generally, self-assembly involves smaller components that organize to build a more complex final system. Final systems can include organized domains, objects, or particles of a characteristic size, spacing, and physical/chemical property). Though bottom-up fabrication with self-assembly is typically more difficult to control than top-down fabrication, it is a parallel process, and therefore a faster form of processing for many applications. Furthermore, the characteristics of self-assembly can be more predictable than top-down fabrication. In order to increase the control over bottom-up fabrication, directed self-assembly with top-down-fabricated templates have been investigated. By combining both top-down and bottom-up fabrication, higher throughput, control, and predictability can be achieved.

1.1 Block Copolymer Thin Films

A diblock copolymer (BCP) is a polymer chain comprised of two blocks of two different polymers covalently bonded in the middle. As is shown in Figure 1.1a and 1.1b, a chain of polymer A and a chain of polymer B are bonded in the middle. This bonding makes the polymer chemically inseparable, and therefore the BCP assumes new micro and macro characteristics not present in the two separate polymers. Each of the polymers contributes their distinct chemical, physical and electrical properties. Importantly, when the polymers are chemically dissimilar, the chains will separate such that polymer A blocks are attracted to similar blocks, and polymer B blocks are attracted to similar blocks, as is shown in Figure 1.1c. In this way, the BCP self-assembles to form regions of mostly polymer A and regions of mostly polymer B. The measure of this dissimilarity of called the Flory-Huggins interaction parameter, χ[7].

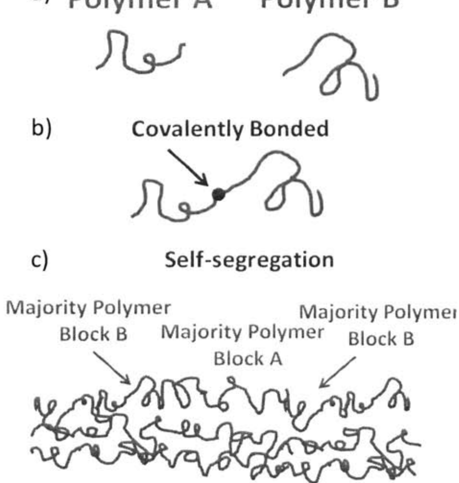

Figure 1.1. Cartoons of different polymers and interaction as BCP. a) polymer A and polymer B are examples of two chemically distinct polymer chains. b) polymers A and B form a BCP if they are covalently bonded together. c) Many BCP chains near each other will self-segregate such that polymer A is attracted to polymer A, and likewise, polymer B is attracted to polymer B.

For bulk BCP, different morphologies (or shapes) have been reported. Typical morphologies include spherical, cylindrical, gyroidal, and lamellar (Figure 1.2a). For spherical, cylindrical and gyroidal, one of the two blocks has less volume and forms the morphology's mesh. The second block has more volume, and forms the bulk, surrounding region. For lamellae, both of the blocks have similar volume, and

therefore are layered with alternating blocks. The gyroidal morphology has not been typically used in templated self-assembly or for nanostructure fabrication, and therefore is not highlighted.

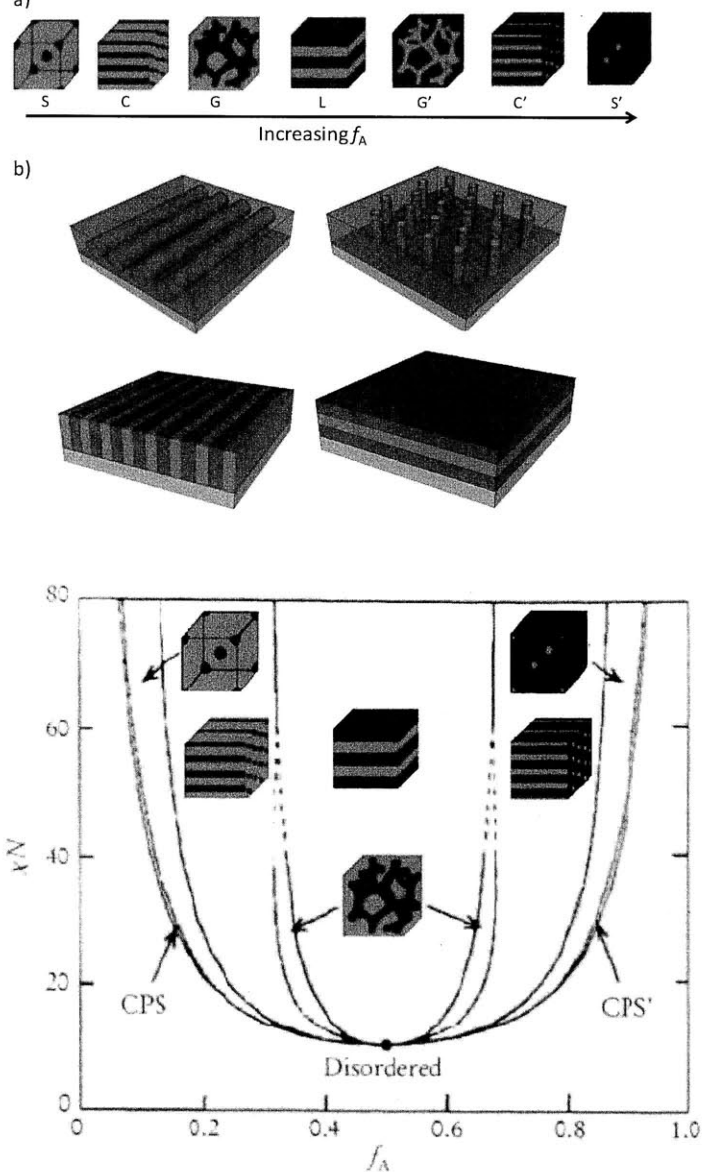

Figure 1.2. Schematics of different morphologies of BCP. a) Morphologies are shown: S: spherical, C: cylindrical, G: gyroidal, L: lamellae (and the inverse, G', C' and S'). As the volume ratio of polymer A is increased, f_A, is increased, these morphology are cycled through[8]. b) 3-dimensional renderings of different BCP thin film morphologies: (clockwise from top-left) parallel cylinders, perpendicular cylinders, parallel lamellae, and perpendicular lamellae. In a thin film, the orientation in which the polymer microdomains lie with respect to the substrate is important. For example, parallel cylinders are significantly different from parallel cylinders.

Figure 1.3 Phase (or morphology) diagram for conventional BCPs showing the position of different morphologies. The y-axis is the product of χ and N (the length of the polymer chain). Larger χN give leads to less disordered region, and therefore the BCP phase-separates more readily. The x-axis is f, the volumetric fraction of block A to the total volume. When f = 0.5, the blocks are equal volume, and the morphology is lamellae. When the volume of block A is increased or decreased, the morphology changes to cylindrical and spherical (with a smaller region of gyroidal)[8].

The spatial separation between two similar nanodomains (for example, two adjacent spheres in the spherical morphology) is λ, the characteristic spacing (aka natural pitch or L_0) (as is shown in Figure 1.4). For the BCPs of interest, L0 is 10s-of-nms and therefore BCPs are useful for nanofabrication[9]. The size of

individual nanodomains is typically half the natural pitch. For nanofabrication, thin films of BCP are used, typically 5-100 nm thick[10]. This thickness is similar to L_0 and therefore only 1-3 nanodomains are stacked on top of the substrate, as is shown in Figure 1.2.b with 1.5 nanodomains.

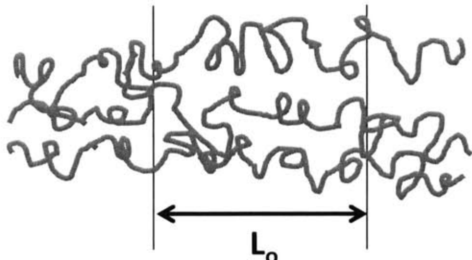

Figure 1.4. Cartoon showing the BCP natural pitch, L_0. When the BCP phase-separates, the distance between two blocks is a key characteristics of the resulting self-assembly. This spacing is called the BCP natural pitch or Lo. It is measurable and a key parameter in the design of templates.

1.2 Templated Self Assembly of BCPs

Researchers have investigated methods for overcoming drawbacks of self-assembly such as short coherence length and local defects. When thin films of BCP self-assemble on the substrate, the nanophase separation leads to an increase in order. The ordering of the nanodomains is typically spatially repeated for a few L_0, but may not be coherent at longer ranges. As is shown in Figure 1.5.a, a distance of a few-hundred nanometers is ordered BCP, but the ordering does not extend farther. The distance over which this ordering occurs is called the coherence length and long coherence is typically desired for nanofabrication. Furthermore, self-assembly minimizes local free-energy and therefore may result in defects.

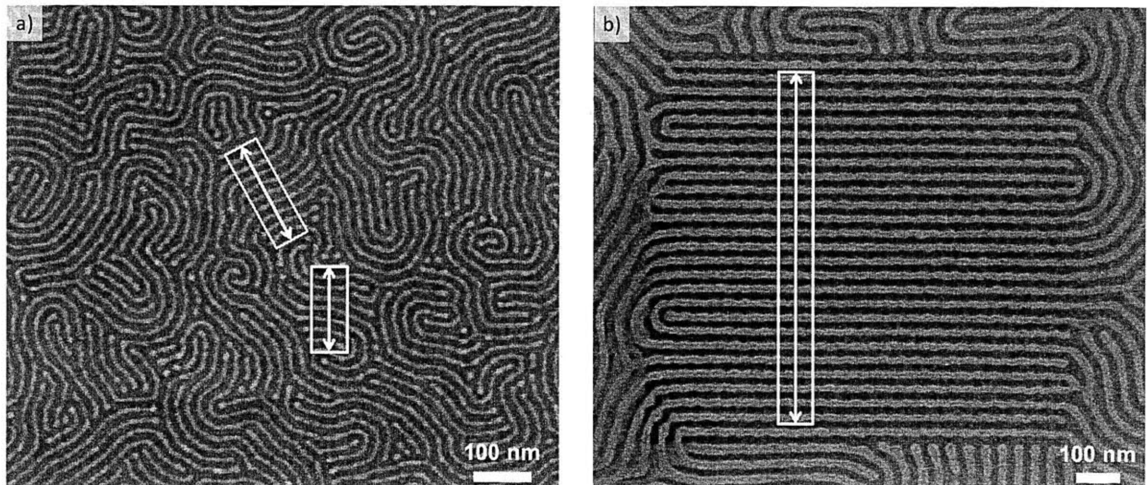

Figure 1.5. SEMs of thin films of BCP on Si substrates. The difference in coherence length is highlighted. a) SEM of a thin film of self-assembled, untemplated poly(styrene-b-dimethylsiloxane) (PS-b-PDMS) BCP. The arrowed-boxes show regions of ordered BCP. These regions are small and the length is short. b) SEM of a thin film of self-assembled, templated PS-b-PDMS BCP (template removed). The arrowed-box shows a region of highly ordered BCP. Compared to a), this region is larger and the length is a longer as a results of the template directing the self-assembly. For all of these SEMs, thick lighter regions are PDMS-block, and darker interstitial regions the substrate.

Templating the self-assembly of the BCP has been used to increase the coherence length for long-range order and induce local control with reduced defects[11-14]. Figure 1.5b shows a micrograph of poly(styrene-b-dimethylsiloxane) (PS-b-PDMS) BCP where the coherence length is increased through the use of templating. Templated self-assembly is capable of increasing coherence length over ultra-large regions[15-16]. Furthermore, templates can provide complex, local control over the BCP self-assembly. The template type (eg. chemical or physical) and material (eg. polymer brush or organic resist) are the two important characteristics that lead to the control over the BCP self-assembly.

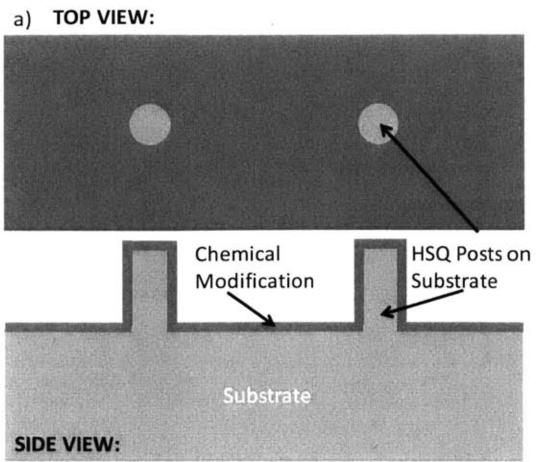

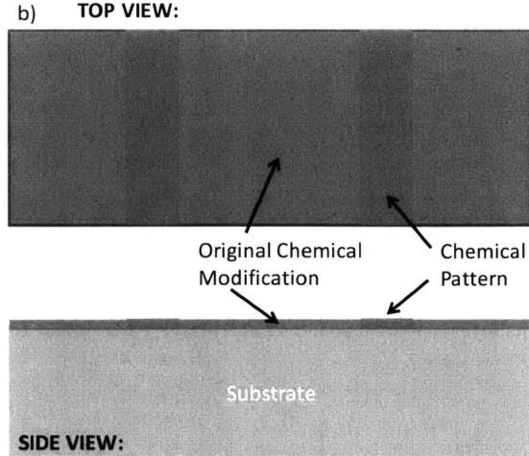

Figure 1.6. Schematics of physical and chemical templates of substrates. a) Top- and side-views of an example physical template on a substrate. In this example, posts of HSQ are patterned on the substrate surface. These posts act as a physical template because a thin film of BCP must assemble around the posts, and therefore the posts physically impede or motivate self-assembly. The entire template is coated with a chemical modification (blue) to give it a uniform chemical nature. b) Top- and side-views of a chemical template on a substrate. In this example, stripes (red) are patterned to be chemically distinct from the surrounding region. These stripes interact with the BCP in a differènt way than the unpatterned (blue) region and therefore serve as a chemical template.

Firstly, there are two main types of templates, physical and chemical templates which are shown Figure 1.6 schematics. Physical templates are hills, valleys, posts, or holes in the topography of the substrate surface in which the BCP thin film must physically integrate. Chemical templates are regions on the substrate surface that are chemically distinct from the adjacent regions (schematic in Figure 1.6.b). For both templates, the surfaces are typically chemically modified such that one of the two blocks of the BCP has a preference to it. As Figure 1.7 depicts, it will be energetically favorable for the preferential BCP block to face towards the modified surface, and the other block to be repelled by the surface. When this happens, the preferential nanodomain will typically align with the design of the template. Alternatively the substrate surface can be chemically modified to be neutral to both blocks, therefore nonpreferential, and the templating features will be the only preferential regions.

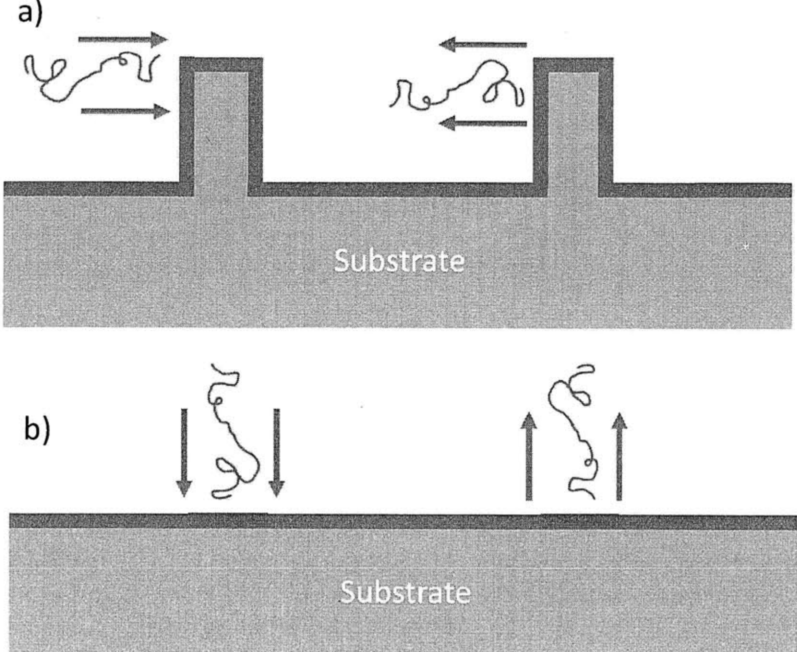

Figure 1.7. Schematics of the template preferentiality with respect to different polymer blocks. a) For physical templates, the posts are chemically modified to be preferential to one of the two polymer blocks. In this example, the posts are preferential to the blue block. Therefore, the blue end of the BCP will likely be attracted to the templating post, whereas the red block will be repelled by the post. b) For chemical templates, regions are chemically different than the surrounding regions. In this example the patterned stripes are chemically similar to the red block of the BCP, and therefore attract the red block. They therefore repel the blue block.

Secondly, the template can be commensurate with the natural pitch of the BCP such that the templating features are spaced an integer number of BCP pitch lengths apart (NL_0). Examples of this are shown in Figure 1.8. If the template is commensurate with the BCP, the block-preferentiality will drive the BCP to be ordered similar to the template. If the template is not commensurate with the BCP, the preferential block will not line up with the template, and therefore will be strained to “fit” into the template. Achieving a commensurate condition between the template and the BCP will induce long-range order in the BCP self-assembly if the template spans a large area[14,17]. An example in Figure 1.8a shows a trench template in which the trench is an integer number of BCP pitches wide (N=4). Similarly, Figure 1.8.b shows a chemical template with chemical patterns that are also an integer number of BCP pitches wide (N=2). These ideas similarly hold for physical post templates, shown in Figure 1.8c. For a

template's effect on the local, complex control of the BCP self-assembly, both commensurability and chemical preference seem to play a role.

a) Trench Template

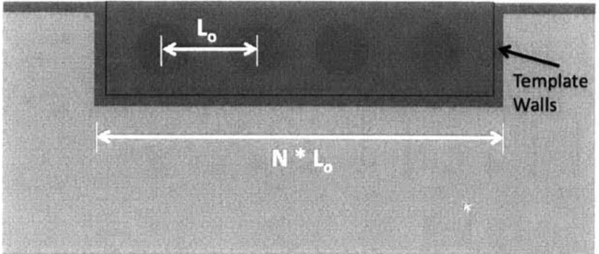

b) Chemical Template

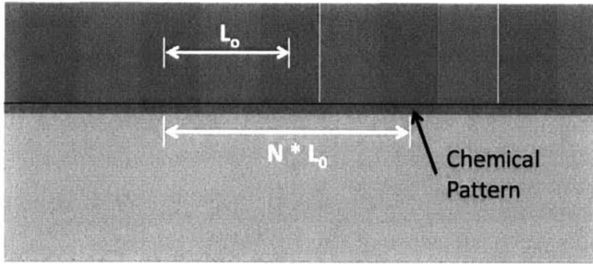

c) Post Template

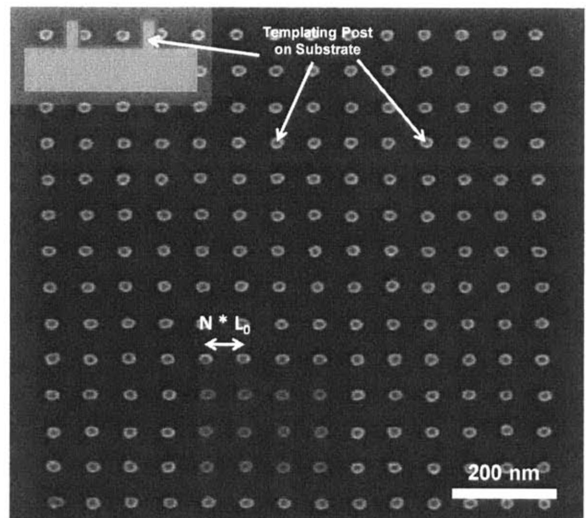

Figure 1.8. Schematics and scanning-electron-micrograph of templates exemplifying the commensurate condition. a) Side-view schematic of a trench template with parallel cylindrical BCP lying within the trench. The trench has a width of $4L_o$ and therefore satisfies a commensurate condition with the BCP (four cylinder nanodomains are directed parallel to the trench). b) Side-view schematic of chemical template with perpendicular lamellae BCP aligning with the chemical patterns. The patterned stripes are spaced by $2L_o$ and therefore satisfy a commensurate condition with the BCP. c) A top-down SEM of a post physical template array. The x-axis spacing between the posts can be $1L_o$ and therefore a single cylinder nanodomain can form over every column of post templates. Blue lines give examples of where the BCP domains may lie within the templating posts.

A thin film of self-assembled BCP, templated or untemplated, can serve as a pattern that can be transferred for the fabrication of other nanofeatures (Figure 1.9) or serve as a functional material. A common pattern transfer process for this application begins with the physio-chemical removal of one of

the two blocks[18-19]. The remaining block can serve as an etch-mask, through which another material below on the substrate can be etched. Furthermore, it is possible for one of the two blocks to be functional (eg. magnetically or electrically), and therefore the thin film serves immediately as an active nanopatterns[20-21].

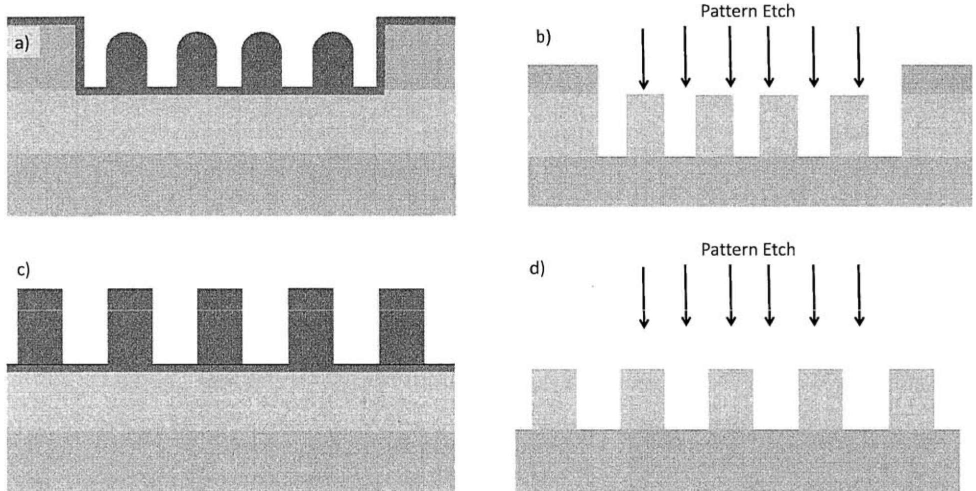

Figure 1.9: Schematics of pattern transfer with BCP (side-view). a) Most of the majority block (blue) has been physio-chemically removed, to leave only the minority block (red) and the physical template exposed. b) top-down etching can transfer the BCP pattern as well as the template into the underlying material (gold) for a final transferred pattern. c) Similar to (a), the blue block has been removed to leave only the red block. d) This is the same as (b), though in this case, the (chemical) template is removed.

1.3 Electron Beam Lithography

To digress, templates can be fabricated with a number of different methods, and scanning-electron-beam lithography (SEBL) was used predominantly for this thesis. SEBL is capable of making templates of arbitrary design, a large variety of shapes and sizes, and with many different materials. Figure 1.10 shows the major steps of the process for negative-tone lithography, as opposed to positive-tone lithography which is used in other applications. Generally, an organic resist is coated on a planar substrate surface. From the top down, a desired pattern is exposed in the resist by exposure to spatially localized energetic radiation.

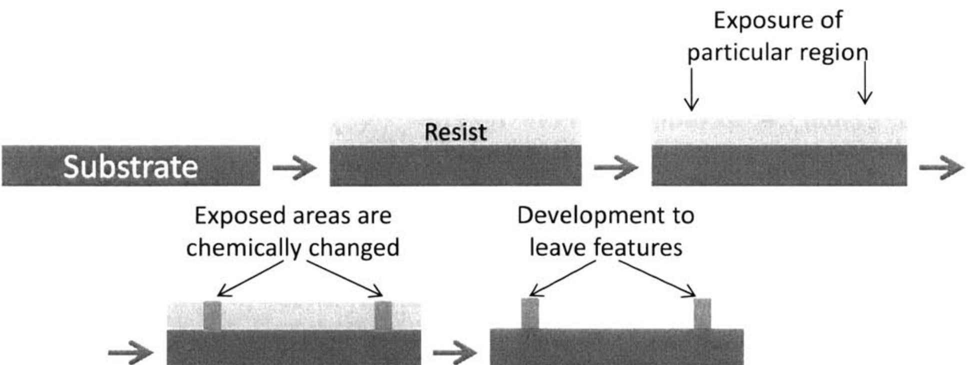

Figure 1.10: Schematic for fabrication process of negative-tone lithographic features. A substrate has a resist deposited on it in a planar form across the surface. Regions of the resist are exposed by energetic radiation, typically light of a certain wavelength or a beam of particles. The exposed region is chemically changed by this radiation. In the case of negative-tone lithography, this chemical change makes the regions resistant to a developer solution. The solution otherwise washes away the undeveloped regions. This whole process leaves features (posts, lines, pads) on the surface that are similarly shaped to the to-down exposure

Scanning-electron-beam lithography is a form of lithography in which the organic resist on the substrate is exposed by a focused beam of electrons from the top down. The beam is essentially similar to what is used for scanning-electron microscopy and a beam column schematic is shown in Figure 1.11. Electrons are accelerated with a desired voltage away from the electron gun at the top of the gun. As the beam of electrons passes through the gun, the beam is focused by a set of permanent magnet lenses and then steered by another set of lenses. At the bottom, the electron beam collides with the substrate where the energy from the electrons is deposited. As the beam scans an area of the sample, a beam blanker can interfere the path of the electrons in order to selectively expose, or not expose, a region on the substrate.

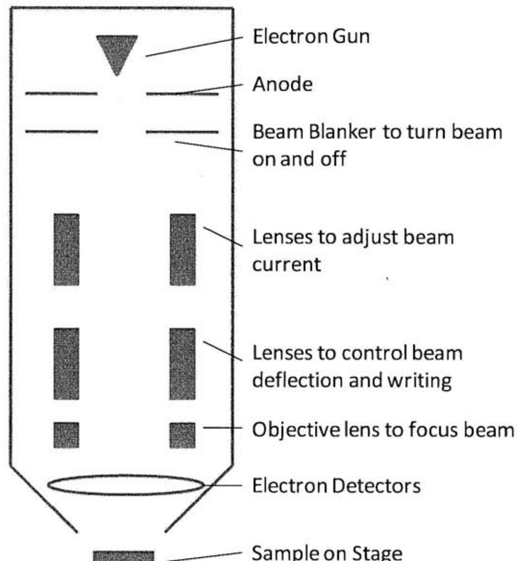

Figure 1.11: Schematic of SEBL microscope column. Electrons are accelerated from the electron gun by the voltage generated by the anode. The beam blanker is open or close which allows or prevents the passage of electrons. A stack of lenses control the current, raster, roundness, writing, and focus of the electron beam as it travels down the column. The beam collides with the sample at the bottom. Other electrons are generated and can be collected in the electron detectors to image the sample.

One important characteristics of the electron beam in SEBL is accelerating voltage. Electrons are accelerated away from the electron gun at high energies, reported as 1-100 keV[22-23]. The electrons collide with the substrate at similar energies, and therefore electrically and physically react in different manners. Lower energy electrons travel slower, have more time to deliver their energy in the resist film, and therefore more efficiently expose the resist. Higher energy electrons travel faster, have less time to deliver their energy to the resist molecules, and therefore less efficiently expose the resist. Alternatively, the interaction volume (three-dimensional region over which the electron deposits its energy) is smaller for high-energy electrons than for low-energy electrons[25]. These aspects mean that it takes fewer electrons to expose a region at low-energies, but the features will not be as small as is achievable at high-energies.

Two important characteristics of the feature fabrication in SEBL are resist sensitivity and contrast, as are shown in Figure 1.12. The sensitivity is the minimum number of electrons required to leave behind some amount of resist (or remove away some resist for positive tone). This has to do with the accelerating voltage and electron efficiency as stated above. Furthermore, other factors impact the sensitivity such as beam-particle type, resist material, and development solution, temperature, time. With higher sensitivity,

the chemical changes of exposure will happen with fewer particles, and an entire design can be patterned relatively faster. Contrast measures the amount of resist left behind as a function of delivered dose. If a small change in delivered dose results in a large change in the amount of resist left behind, then the contrast is high. A high contrast will lead to a more binary exposure process in which exactly the exposed regions result in lithographic features. Alternatively, lower contrast will give features with angled side-wall and more of a grey-scale exposure result.

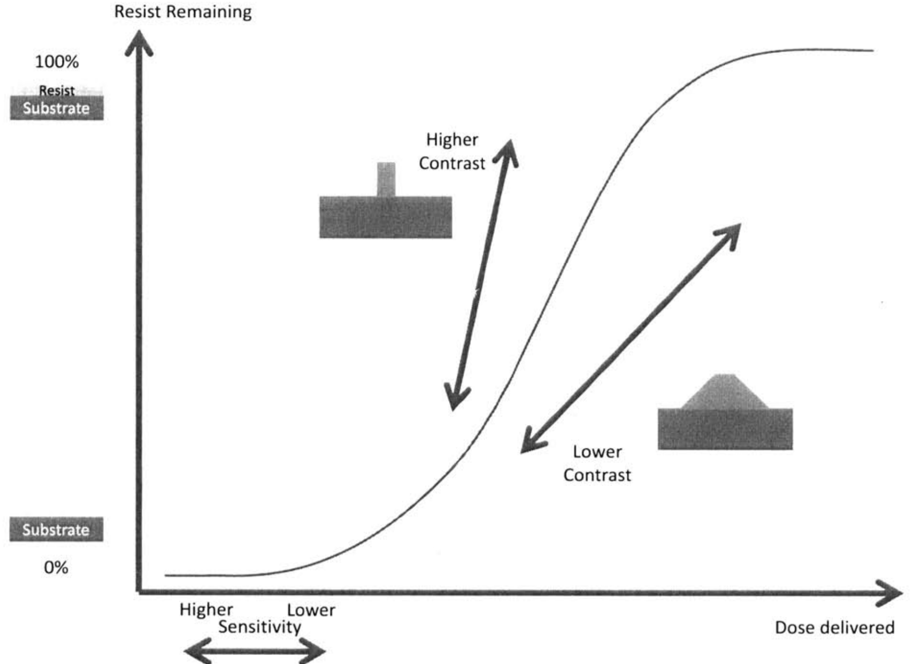

Figure 1.12: Resist Remaining vs. Dose Delivered curve. For a negative-tone resist, all of the resist is typically washed away during development. As the radiation dose delivered to a region is increased, the amount of resist remaining after development is increased, up to 100% of the original resist thickness. Sensitivity: high sensitivity leaves some resist remaining with a lower dose while lower sensitivity leaves some resist remaining with a higher dose. Contrast: The contrast is represented by the slope of this curve. For higher contrast, a small change in delivered dose results in a large change in remaining resist and lithographic features with steeper sidewalls. For lower contrast, a small change in delivered dose results in a small change in remaining resist and lithographic features with sloped sidewalls. To achieve high resolution lithographic features, higher contrast is desired.

Though the chapters in this theses don't discuss an investigation into the science of lithography, experimental work was dependent on previous advances in lithography technology. Most specifically the work completed at MIT has supported the fabrication of high-resolution features of different materials. A salty developer solution was determined for producing high-resolution features in hydrogen

silsesquioxane (HSQ) resist[26]. Poly(methyl methacrylate) (PMMA) was found to act as a negative-tone resist (as opposed to the typical positive tone) when exposed to high electron-beam doses[27]. Furthermore, the Appendix specifically discusses the sensitivity of Neon-Ion-Beam Lithography and was supported by previous research in the area of scanning-ion-beam lithography[27].

1.4 Prior Work

Significant work has been accomplished in the area of templated self-assembly of BCPs with chemical templates. The canonic example has the chemically patterned region preferential to one of the polymer blocks, and the surrounding region non-preferential, or neutral, to both of the polymer blocks[17,28]. When the spacing between patterned stripes was commensurate with the BCP pitch, then the BCP assembled parallel to an array of such patterned regions (similar to Figure 1.8a). Furthermore, when the patterned regions made bends, or junctions, it was possible for the preferred polymer block to follow the bends and junctions[29].

Also, much research has been performed to template the self-assembly of BCPs with physical templates. Initial work in this area relied on topographical trenches on the substrate in which the BCP would self-assemble[30] (similar to Figure 1.8b). When the trench width was commensurate with the BCP pitch, the nanodomains ordered well within the trench. This work was expanded to include other types of topographical templates such as atomic crystal edges and other BCPs[31], as well as a large effort in fabrication of templates with nanoimprint lithography[32].

More complex physical templating was introduced in the form of arrays of posts, fences, or holes. These template features occupied key positions within the BCP lattice to provide complex, local control over the self-assembly. In extension, the array of features matched the BCP commensurate condition in off-axis directions such that the BCP lattice oriented in this same off-axis direction[33-34].

1.5 Objectives and Challenges

The investigation of templated self-assembly of block copolymers is directed towards 3 major objectives and challenges:

Increased Long-Range Order – As was discussed earlier, a thin film of self-assembled BCP doesn't necessarily exhibit long-range order. Templated self-assembly is directed at efficiently and effectively increasing the order over large areas. To increase the impact of this objective, the challenge is to achieve defect-free order over wafer-scale areas with highly-efficient patterning of the templates.

Complex and Local Control – When BCP thin films self-assemble, they can create complex patterns, but control of these patterns requires a template. It is an objective to develop ways to control the BCP locally such that complex patterns can be directed through templating. Research has the challenge of templating the self-assembly of BCPs to achieve bends, junctions and crosses, in single and multiple layers, and with highly local control.

Understanding of Self-Assembly Characteristics – Templates can be used to help understand how BCPs self-assemble. This includes the associated energies of interaction with different interfaces, stress and strain energies, and thermal kinetics. Templating can eliminate certain analytical variables, or provide a larger degree of predictability to test against theory/models. Reverse-engineering of templates is a challenging objective: inputting a desired nanopattern, and using models and simulations to output a needed template to achieve the nanopatterns.

1.6 Applications

Nanopatterns that result from templated self-assembly of BCP have many important applications. They can be used in the fabrication of bit-patterned-media for memory recording devices[20]. A large application is in the semiconductor fabrication area for manufacturing of integrated circuits. The nanopatterns may be used as mask for the deposition steps in producing transistors and RAM[19]. Nanopatterns generated by templated self-assembly have been useful in applications such as nanoelectronics, energy devices,

biosensing, plasmonics, nano-electronic and mechanical systems (NEMS) and surface energy engineering[1-6].

1.7 Overview of Thesis Work

This thesis covers work in the area of templated self-assembly of block copolymers. Each Chapter is a separate investigation, but they each generally relate to one of the above 3 objectives and challenges.

Chapter 2: Multiple Surface Energy Substrates for PS-b-PMMA Self-Assembly – The self-assembly and templated self-assembly of lamellae-morphology PS-b-PMMA is tested on samples modified with a single or two different self-assembled monolayers

Chapter 3: Assembly and Direction of a High-χ BCP – The self-assembly and templated self-assembly of a lamellae-morphology high-χ BCP was tested for varying annealing, block-removal, and surface energy characteristics. A wide variety of physical templates was tested with the target of long-range and complex, local control.

Chapter 4: Lithographic Overlay of Negative-tone Resist Features – The overlay metric of the Raith 150 system was determined by patterning of HSQ negative-tone resist patterns in two separate electron-beam-lithography writes.

Chapter 5: Sacrificial Templates for PS-b-PDMS Self-Assembly – Templating of 2D and 3D nanopatterns with PS-b-PDMS cylindrical BCP with PMMA as a sacrificial, negative-tone resist. PMMA was investigated for its removal and effectiveness in replicating similar results with HSQ resist.

Appendix I: Measurement of Neon-Ion-Beam Lithography Contrast Curve – NIBL was tested with HSQ negative-tone resist. Pads were patterned and the remaining HSQ resist was measured by AFM. These measurements were used to determine the sensitivity of NIBL with HSQ.

References

1. W. Lu, and C. Lieber, Nanoelectronics from the Bottom up. *Nat. Mater.*, 6, 841 (2007).
2. J. Baxter, Z. Bian, G. Chen, D. Danielson, M. S. Dresselhaus, A. G. Fedorov, T. S. Fisher, C. W. Jones, E. Maginn, U. Kortshagen, A. Manthiram, A. Nozik, D. R. Rolison, T. Sands, L. Shi, D. Sholl, and Y. We, Nanoscale Design to Enable the Revolution in Renewable Energy. *Energy Environ. Sci.*, 2, 559 (2009).
3. J. L. Arlett, E. B. Myers, and M. L. Roukes, Comparative Advantages of Mechanical Biosensors. *Nat. Nanotechnol.*, 6, 203 (2011).
4. E. Ozbay, Plasmonics: Merging Photonics and Electronics at Nanoscale Dimensions. *Science*, 311(5758), 189 (2006).
5. J. S. Bunch, *Nat. Nanotechnol.*, NEMS: Putting a Damper on Nanoresonators. 6, 331 (2011).
6. Y. Yang, C. Hsua, T. Chang, L. Kuo, and P. Chen, Study on Wetting Properties of Periodical Nanopatterns by a Combinative Technique of Photolithography and Laser Interference Lithography. *Appl. Surf. Sci.*, 256(11), 3683 (2010).
7. Bates, F. S., & Fredrickson, G. H. *Annual* Block Copolymer Thermodynamics: Theory and Experiment. *Review of Physical Chemistry*, *41*(1), 525–557 (1990).
8. Reprinted with permission from Bates, F. S., & Fredrickson, G. H., *Physics Today*, *52*(2), 32 (1999). Copyright 1999, American Institute of Physics.
9. Cushen, J. D., Otsuka, I., Bates, C. M., Halila, S., Fort, S., Rochas, C., Easley, J. A. Oligosaccharide/Silicon-Containing Block Copolymers with 5 nm Features for Lithographic Applications. *ACS nano*, *6*(4), 3424–3433 (2012).
10. Hawker, C. J., & Russell, T. P. Block copolymer lithography: Merging "bottom-up" with "top-down" processes. *MRS Bulletin*, 30(12), 952–966 (2005).
11. Kim, S. O., Solak, H. H., Stoykovich, M. P., Ferrier, N. J., De Pablo, J. J., & Nealey, P. F. Epitaxial self-assembly of block copolymers on lithographically defined nanopatterned substrates. *Nature*, *424*(6947), 411–414 (2003).
12. Bita, I., Yang, J. K. W., Jung, Y. S., Ross, C. A., Thomas, E. L., & Berggren, K. K., Graphoepitaxy of self-assembled block copolymers on two-dimensional periodic patterned templates. *Science*, *321*(5891), 939–943 (2008).
13. Jung, Y. S., Jung, W., & Ross, C. A., Nanofabricated concentric ring structures by templated self-assembly of a diblock copolymer. *Nano Letters*, *8*(9), 2975–2981 (2008).
14. Park, S., Lee, D. H., Xu, J., Kim, B., Hong, S. W., Jeong, U., Xu, T., Macroscopic 10-terabit-per-square-inch arrays from block copolymers with lateral order. *Science*, *323*(5917), 1030–1033 (2009).
15. S. Park, D. H. Lee, J. Xu, B. Kim, S. W. Hong, U. Jeong, T. Xu, T. P. Russell, Macroscopic 10-Terabit–per–Square-Inch Arrays from Block Copolymers with Lateral Order. *Science* 323, 1030 (2009).
16. Jeong, S.-J., Moon, H.-S., Kim, B. H., Kim, J. Y., Yu, J., Lee, S., Lee, M. G. Ultralarge-area block copolymer lithography enabled by disposable photoresist prepatterning. *ACS nano*, *4*(9), 5181–5186 (2010).
17. Ruiz, R., Kang, H., Detcheverry, F. A., Dobisz, E., & Kercher, D. S., Density multiplication and improved lithography by directed block copolymer. *Science* (2008).
18. Yuk-Hong Ting, Sang-Min Park, Chi-Chun Liu, Xiaosong Liu, F. J. Himpsel. Plasma etch removal of poly(methyl methacrylate) in block copolymer lithography. *J. Vac. Sci. Technol. B*, 26, 1684 (2008).
19. Xiao, S., Yang, X., Edwards, E. W., La, Y.-H., & Nealey, P. F. Graphoepitaxy of cylinder-forming block copolymers for use as templates to pattern magnetic metal dot arrays. *Nanotechnology*, *16*(7), S324–S329 (2005).
20. Hellwig, O., Bosworth, J. K., Dobisz, E., Kercher, D., Hauet, T., Zeltzer, G., Risner-Jamtgaard, J. D. Bit patterned media based on block copolymer directed assembly with narrow magnetic switching field distribution. *Applied Physics Letters*, *96*(5), 052511 (2010).
21. Kulkarni, P., McCullough, L. A., Kowalewski, T., & Porter, L. M. Investigation of electrical properties of nanostructured carbon films derived from block copolymers. *Synthetic Metals*, *159*(3-4), 177–181 (2009).
22. Vitor R. Manfrinato, Lin Lee Cheong, Huigao Duan, Donald Winston, Henry I. Smith, Karl K. Berggren, Sub-5 keV Electron-Beam Lithography in Hydrogen Silsesquioxane Resist. *Journal of Microelectronic Engineering*, 88, 3070-3074 (2011).

23. Vieu, C. Electron beam lithography: resolution limits and applications. *Applied Surface Science*, *164*(1-4), 111–117 (2000).
24. Ziegler, J. F., Ziegler, M. D., & Biersack, J. P. SRIM – The stopping and range of ions in matter. *Nuclear Instruments and Methods in Physics Research Section B: Beam Interactions with Materials and Atoms*, *268*(11-12), 1818–1823 (2010).
25. Joel K. W. Yang and Karl K. Berggren, Using high-contrast salty development of hydrogen silsesquioxane for sub-10-nm half-pitch lithography. *Journal of Vacuum Science and Technology B*, 25, 2025 (2007).
26. Huigao Duan, Donald Winston, Joel K. W. Yang, Bryan M. Cord, Vitor R. Manfrinato, and Karl K. Berggren, Sub-10-nm Half-Pitch Electron-Beam Lithography by Using PMMA as a Negative Resist *Journal of Vacuum Science and Technology B* 28 C6C58-C6C62 (2010).
27. Donald Winston , Vitor R Manfrinato , Samuel M Nicaise , Lin Lee Cheong , Huigao Duan , David Ferranti , Jeff Marshman , Shawn McVey , Lewis A Stern , John A Notte , and Karl Berggren, Neon Ion Beam Lithography (NIBL). *Nano Letters* 11(10) 4343-4347(2011).
28. Sang Ouk Kim, Harun H. Solak, Mark P. Stoykovich, Nicola J. Ferrier, Juan J. de Pablo & Paul F. Nealey, Epitaxial self-assembly of block copolymers on lithographically defined nanopatterned substrates. *Nature* 424, 411-414 (2003).
29. Stoykovich, M. P., Müller, M., Kim, S. O., Solak, H. H., Edwards, E. W., De Pablo, J. J., & Nealey, P. F. Directed assembly of block copolymer blends into nonregular device-oriented structures. *Science*, *308*(5727), 1442–1446 (2005).
30. J. Y. Cheng, C. Ross, E. L. Thomas, H. I. Smith, G. J. Vancso, Templated self-assembly of block copolymers: Effect of substrate topography. *Adv. Mater.* 15, 1599-1602 (2003).
31. L. Rockford, Y. Liu, P. Mansky, T. P. Russell, Polymers on nanoperiodic, heterogeneous surfaces. *Phys. Rev. Lett.* 82, 2602-2605 (1999).
32. Vincent S. D. Voet, Teresa E. Pick, Sang-Min Park, Manuel Moritz, Aaron T. Hammack, Jeffrey J. Urban,D. Frank Ogletree, Deirdre L. Olynick, and Brett A.Helms, Interface Segregating Fluoralkyl-Modified Polymers for High-Fidelity Block Copolymer Nanoimprint Lithography. *J. Am. Chem. Soc.*, 133(9), 2812–2815 (2011).
33. Joel K. W. Yang, Yeon Sik Jung, Jae-Byum Chang, R. A. Mickiewicz, A. Alexander-Katz, C. A. Ross and Karl K. Berggren, Complex self-assembled patterns using sparse commensurate templates with locally varying motifs. *Nature Nanotech.* 5, 256-260 (2010).
34. Ion Bita, Joel K. W. Yang, Yeon Sik Jung, Caroline A. Ross, Edwin L. Thomas, and Karl K. Berggren, Graphoepitaxy of Self-Assembled Block Copolymers on Two-Dimensional Periodic Patterned Templates. *Science* 321, 939 (2008).

Chapter 2: Multiple Surface Energy Substrates for PS-b-PMMA Self-Assembly

Previous reports have shown templated and untemplated self-assembly of poly(styrene-b-methyl methacrylate) (PS-b-PMMA) BCP (Figure 2.1)[1-3]. PS-b-PMMA readily nanophase separated into a lamellar morphology and the PMMA-block was removable for imaging and pattern transfer purposes. Previous reports have used thermal annealing at temperatures above 170°C at annealing times ranging from 1 hour to 7 days in order to achieve high-quality self-assembly of PS-b-PMMA thin films[1,4]. Chapter 2 outlines the investigation of PS-b-PMMA as a block copolymer for use in complex combined templating schemes. The objectives of this work was to develop templating for PS-b-PMMA that: 1) locally controlled the self-assembly of PS-b-PMMA for complex nanopatterns and 2) led to a better understanding of the polymer's self-assembly characteristics.

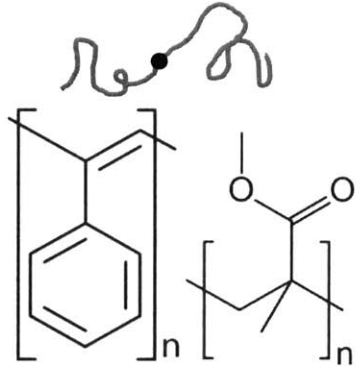

Figure 2.1: (top) Schematic diagram of poly(styrene-b-methylmethacrylate) where red on the left signifies PS and blue on the right signifies PMMA. (bottom) Molecular schematics for PS and PMMA .

2.1 PS-b-PMMA Self-Assembly with Surface Energy Modification

An important characteristic of the self-assembly of lamellar BCP is the surface energy (SE) of each polymer block, as well as the substrate surface and polymer-air interface. Bulk polystyrene and poly(methyl methacrylate) have measured surface energies of 31.7 and 38.4 dynes/cm, respectively. The used BCP naturally forms a lamellar morphology in thin films. For nanofabrication applications, perpendicular lamellae are preferential (See Figure 1.2b). Production of perpendicular lamellae necessitates substrate and atmosphere interfacial surface energies that are neutral to both the PS and PMMA blocks[2,3,5,6]. Alternatively, if the substrate SE is preferential to one of the polymer blocks (eg. the substrate SE is quantitatively closer to the PS block's SE), symmetric parallel lamellae may form. For perpendicularly-oriented lamella PS-b-PMMA, a surface energy between that of PS and PMMA is necessary (between 31.7 and 38.4 dynes cm^{-1}) for neutrality to be achieved.

In order to achieve neutrality, it is possible to chemically modify this surface with a self-assembled monolayer (SAM)[7]. The native oxide surface of a Si wafer has higher SE (about 45 dynes cm^{-1}). Therefore the native oxide surface is preferentially wetted by the PMMA-block of PS-b-PMMA, and is not neutral. A SAM, as shown in Figure 2.2, can be formed when a single-layer of short-chain molecules deposits on the substrate surface. The head of the molecule is one of the ends of the SAM that is able to chemically bond to the surface. The body of the molecule is the middle of the SAM and is typically a backbone of a 2-20 carbon atoms in length. The tail of the molecule (R) is the end opposite end of the SAM which populates the air-interface to act as a new surface. For well-deposited SAMs, the molecules chemically bond to the surface adjacent to each other, with high surface coverage, the molecules are oriented with the backbone of the SAM molecule perpendicular to the substrate surface and parallel to the adjacent molecule. The tails of the molecules populate the exposed top-surface of the monolayer (Figure 2.2b). For substrates modified with well-deposited SAMs, a uniform native oxide substrate surface can adopt the characteristic surface chemistry of the new monolayer.

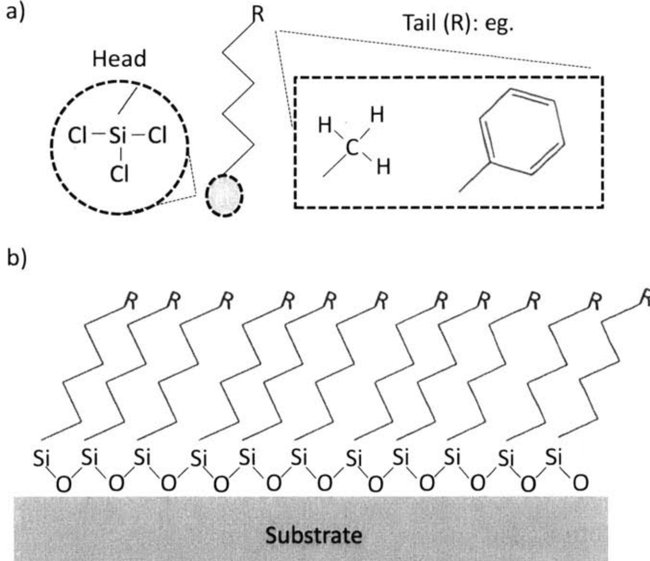

Figure 2.2: Schematics of self-assembled monolayers. a) Schematic of a trichlorosilane-based molecule for a self-assembled monolayer (SAM). The head is a trichlorosilane, attached to a carbon backbone. The reactive tail can be a number of different molecules, shown here with hydroxyl- and phenyl ring terminations. b) The head bonds to the silica-based substrate and many SAM molecules arrange to form an crystalline-ordered monolayer on the substrate surface.

This study used a number of trichlorosilane-based SAMs which have been previously used for PS-b-PMMA self-assembly and they are listed in Table 2.1[8]. ^{n}Butyltrichlorosilane (BTS) and Hexyltrichlorosilane (HTS) have hydrogen atoms as their terminating reactive species (R) and Phenethyltrichlorosilane (PTS) is terminated with a phenyl ring. SE measurements of these SAMs are reported and discussed below.

^{n}Butyltrichlorosilane	4 Carbon backbone, H-terminated	
Hexyltrichlorosilane	6-Carbon backbone, H-terminated	
Phenethyltrichlorosilane	2-Carbon backbone, Phenyl-terminated	

Table 2.1: List of the SAMs used in the presented results.

As discussed in Chapter 1, physical and chemical templates can be used to direct the self-assembly of BCPs. Publications have reported the separate employment of these two methods. When employed individually, each of the methods exhibits characteristic limitations. By developing a combined physical and chemical templating method, these characteristic limitations may be overcome. Furthermore, physical and chemically templating could contribute to the overall objectives and challenges of templated self-assembly of block copolymers. Although the work discussed in Chapter 2 focused on the separate development of these templating methods, this work was in preparation for the future combined method.

An example of the combined physical and chemical templating method is shown in Figure 2.3. In this case, an array of posts is fabricated on the substrate to act as a physical template. In conventional physical post templating, all of the posts are covered with a similar chemical modification such that they all have the same SE. In the combined method, the substrate is first chemically modified with a first SAM. The templating posts, comprised of a negative-tone resist hydrogen silsesquioxane (HSQ), are then fabricated

on top of this substrate. Then, the posts are chemically modified with a second SAM, which should not affect the first SAM. Consequently, the posts assume a different SE than the substrate, and can be used to combine physical and chemical templating.

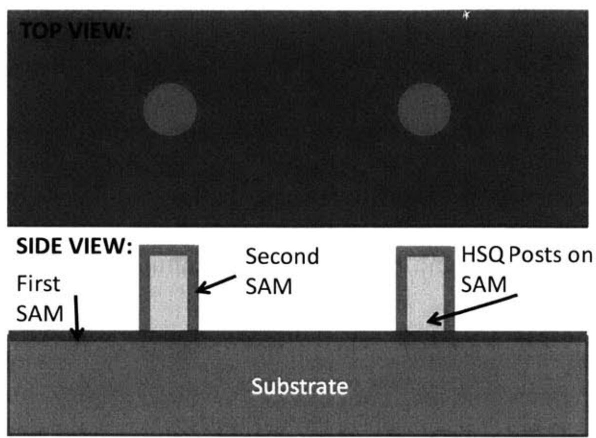

Figure 2.3: Top- and side-view of an ideal example combined templating method. The substrate is modified with a first SAM (blue) to assume a first chemical nature. HSQ posts are then patterned on the SAM-coated substrate (grey). The HSQ posts are modified with a second SAM (red) to assume a second chemical nature. In this manner, both physical and chemical templating are combined.

Figure 2.4 shows the major steps of the fabrication process. In some samples, only one SAM was deposited: HSQ physical post templates were first fabricated and then the SAM was deposited. In some samples, two SAMs were deposited: the first SAM was deposited, HSQ physical post templates fabricated, and then the second SAM deposited.

In order to produce HSQ physical template posts, a thin film of HSQ was first spun on the samples with no post-bake (thicknesses varied from 16 nm to 61 nm). Templates were exposed with scanning-electron-beam lithography (SEBL) on a Raith 150 (30keV, 30 μm objective aperture, 6mm working distance). After exposure, the samples were developed with a salty developer (4% NaCl / 1% NaOH in deionized water) at 24°C for 4 minutes and then rinsed with deionized water for 2 min and blown dry under N_2[9]. HSQ is a negative-tone resist, and therefore the unexposed resist is removed by the developer

solution. In certain experiments, SEBL exposure of the HSQ was "simulated". In these cases, HSQ was spun on the samples, stored in air for over 12 hours and developed as outlined above without electron-beam exposure via SEBL.

SAM deposition was initiated by soaking a prime Si wafer in a bath of CD26 (MICROPOSIT MF - CD-26 DEVELOPER, Dow Corning, Inc.), which contains a 2.5 wt. % tetramethylammonium hydroxide (TMAH) to fully hydroxyl-terminate the native silica surface. The wafer was rinsed with deionized water for 2 minutes, and blown dry under N_2. A SAM solution was prepared by mixing 100 μL of the desired SAM molecule (Gelest) in 100 mL toluene (J.T. Baker 99.9%) and matured for 10 minutes. The wafer was immersed in this solution for 20 minutes to deposit the SAM, rinsed with toluene, and then blown dry under N_2. Samples were baked on a hotplate at 120°C for 5 minutes. The ordering or crystallinity of the deposited SAM was not determined.

Most of the samples were exposed to UV/Ozone for varying periods of time (conditions noted in results below).

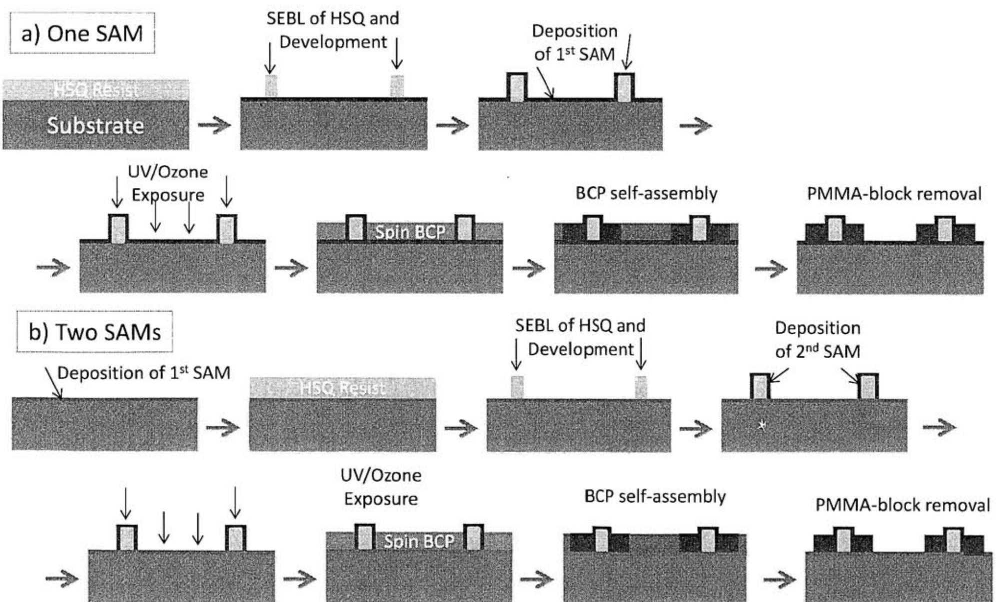

Figure 2.4: Major steps of the fabrication process. (a) Steps when only a single SAM is to be deposited. (b) Steps when two different SAMs are to be deposited.

PS-b-PMMA (1.85 wt. % in 2-heptanone) was spin-coated on the samples at typical speeds of 1750-2500 rpm (60 sec, 10 acceleration (a.u.)) to produce thin films with thickness of 30-50 nm. The lamellae-forming PS-b-PMMA was purchased from Polymer Source (P2355, 98.2kg/mol, L_o ~45 nm). The remaining solvent after spin-coating was evaporated by baking the samples on a hot plate (130°C, 1 min). For thermal annealing, the oven was purged with N_2 gas and then the heating elements turned on. The desired temperature (about 220°C) was achieved after about 1.5 hours and the oven turned off after a total time of 2-2.5 hours. The oven was then left to cool to room temperature over the course of about 6 hours. The PMMA block of the polymer was removed by exposing the samples to 1 minute of UV/Ozone, then rinsing in acetic acid for 1 minute and deionized water for 1 minute.

In order to determine the SE characteristics of substrates, the contact angle of deionized water droplets was measured with a goniometer (model?) (as shown in Figure 2.5). Static, advancing, and receding contact angles of a water droplet dispensed from a syringe were measured. Each reported angle data point is an average of the contact angle on both sides of the water droplet at 3 different places on the sample, for a total of 6 angles. These data points were not used to compute the exact SE of samples, but only taken as measures of relative SE.

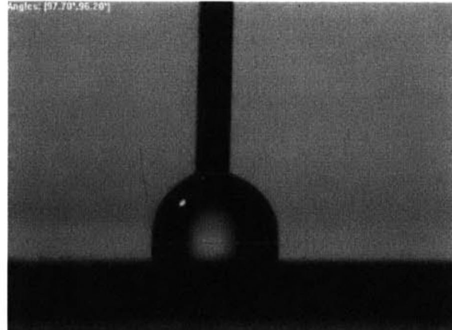

Figure 2.5: Microscope image of a water droplet on a sample in the goniometer. The syringe from the top dispenses the water onto the sample surface, and the microscope takes an image. This image is analyzed to determine the contact angle of the water on the surface.

Microscopy of samples was performed with a Raith 150 (10 keV, 30 μm aperture, 6 mm working distance). As a result of the post-processing after BCP annealing, the PMMA-block was removed and high image contrast was achieved between the PS-block and the PMMA-voids.

2.2 Single-SAM Sample Modification for PS-b-PMMA Self-Assembly

For physical templating, HSQ posts were achieved on SAM-modified substrates. The fabrication of posts on a non-oxide substrate differed from previous results because physical post templates are typically fabricated on bare Si substrates[10]. With the objective of future application in combined physical and chemical template, posts were written in the process step after the first SAM deposition. This SAM-deposited substrate had a lower SE and therefore a higher likelihood of post collapse[11] (lower adhesion of the post-base to the substrate), as is seen in Figure 2.6a. This effect was mitigated by reducing the HSQ resist thickness (hence post height) and therefore reducing torque on the post-base from the tall post (Figure 2.6b).

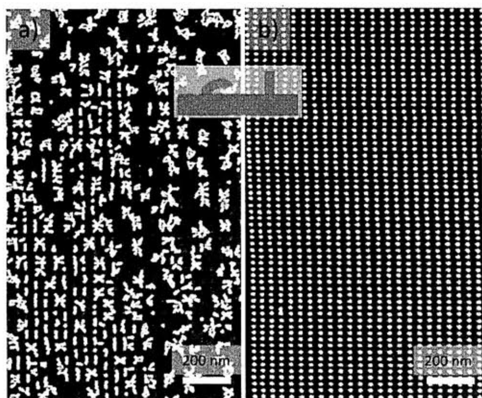

Figure 2.6: HSQ Posts fallen over and standing on a substrate. a) HSQ posts (white) are fallen over on the substrate due to capillary collapse. B) HSQ posts are standing on substrate surface, and therefore observed from the to-down as white dots. In this case, the thickness of the HSQ layer was lower, and therefore posts experienced

Dewetting of the BCP thin film was a significant issue, and it was determined that an ideal substrate surface energy (SE) was required to achieve a uniformly-wet BCP thin film. Therefore, a significant portion of the investigation focused on measuring contact angles and characterizing surface energy (SE) changes for different SAM deposition and processing conditions. Reported below are surface energy characteristics for different SAMs and process parameters. Templating of the PS-b-PMMA was carried out on many samples, though this Chapter only reports for samples where BCP thin film dewetting was overcome.

In many cases, the substrate was modified with one SAM and this process is as shown in Figure 2.4a. In these cases, the HSQ templates were first fabricated on a bare Si substrate. The SAM was then deposited over the entire substrate, including, if applicable, the fabricated HSQ template posts.

The contact angles (static, advancing, and receding) for a SAM of PTS are shown in Table 2.2. Angles are reported for various treatments such as development with different resist developers and UV/Ozone exposure times. The contact angle generally increased with longer development times and UV/Ozone exposure. This trend is opposite of what was expected, but is also within reasonable systematic error. Furthermore, TMAH developer increased the contact angle more than the salty developer, suggesting that the salty developer has less of an impact on the SAM. These experiments were performed to determine the effect of intermediate processes on the surface energy of the original SAM (PTS in these cases). It was important to understand that the contact angle of the original SAM did not remain constant as samples were put through many other processes. These processes could not be circumvented. For example, the development process was necessary for the HSQ physical post fabrication. Alternatively, UV/Ozone exposure was investigated as a strategic process step used to change the substrate contact angle. Though these contact angle investigations were only preliminary, they supported the assumption that intermediary processes significantly change the substrate contact angle and the effect must therefore be understood.

SAM Type	Conditions	Contact Angle (deg): Static	Advancing	Receding
PTS	1 min Salty Develop	89.05	-	70.7
	4 min Salty Develop	88.25	90.7	71.35
	6 min Salty Develop	92.15	92.95	74.475
	1 min Salty Develop 20sec UV/Ozone	76.775	76.925	52.025
	4 min Salty Develop 20sec UV/Ozone	74.575	73.45	49.05
	1 min TMAH Develop	97.075	97.9	72.225
	4 min TMAH Develop	96.575	97.225	73.225
	6 min TMAH Devleop	90.875	95.05	77.85

Table 2.2: Contact angle measurements for a number of different processing conditions. The conditions are for PTS deposition. Static, advancing, and receding contact angles are reported.

Before attempting templated self-assembly, it was important to determine simple BCP thin film self-assembly characteristics for substrates without any sort of template. In order to examine the self-assembly characteristics of PS-b-PMMA, BCP thin films were annealed on Si substrates coated with a BTS SAM. After deposition of the BTS, samples were exposed to UV/Ozone for varying amounts of time. This process degraded the SAM to increase in the substrate surface energy. With varying amounts of time, the SE was varied in order to find an ideal SE which achieved perpendicular lamellae. Resulting annealed BCP thin films are shown in Figure 2.7. 20 seconds of UV/Ozone exposure resulted in the best perpendicular lamellae BCP. Higher exposure times (higher surface energy) resulted in mostly parallel lamellae BCP, as is noted from the uniform gray-scale color of the 28- and 30-sec images.

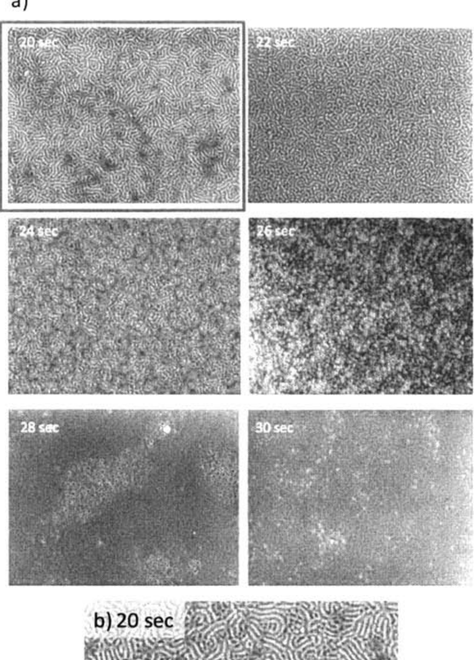

Figure 2.7: SEMs of PS-block of PS-b-PMMA on SAM-coated Si substrate. (a) Each sample was exposed to UV/Ozone for the designated seconds prior to BCP deposition and self-assembly. The best BCP assembly occurred for 20 sec of exposure to UV/Ozone (b). BCP was spun to a thickness of about 30 nm. The lighter regions are the PS-block and the darker regions are the removed PMMA-block to show the Si substrate

After determining the self-assembly characteristics on untemplated substrates, physical post templates were fabricated for templated self-assembly. Templates were fabricated and samples were coated with a BTS SAM and then modified with varying times of UV/Ozone exposure as noted above. PS-b-PMMA was shown to be templated by arrays of HSQ posts at rectangular-periodic spacing to a moderate degree. The result presented in Figure 2.8 shows a complex BCP pattern. PS domains are oriented predominantly in the y-direction, but exhibit 90° bends toward the middle of the templated region. This type of result was more predominant in Section 2.3 and will be highlighted.

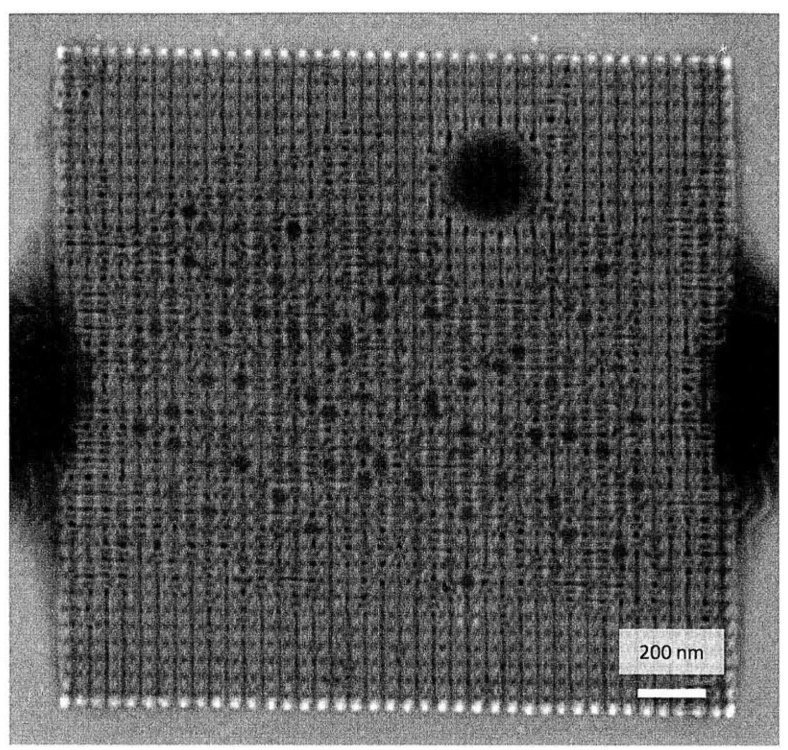

Figure 2.8: Top-down scanning electron micrograph of templated PS-b-PMMA BCP with the single SAM system of BTS. The sample was exposed to *** seconds of UV/Ozone, and HSQ template fabricated over the top of the SAM-coated substrate (50 x 50 nm rectangular post array).The PS-b-PMMA is templated by the posts to align predominantly in the y-direction, though much of the BCP aligns in the x-direction towards the middle of the template. For the SEM, the bright dots are HSQ templating posts, thick lighter regions are PS-block, and darker interstitial regions the removed-PMMA-block. BCP is dewet from the area surrounding the templated region.

2.3 Multiple-SAM Sample Modification for PS-b-PMMA Self-Assembly

In many cases, the substrate was modified with two different SAMs and this process is shown in Figure 2.4b. The motivation for multiple SAMs was discussed previously in Chapter 1, and is to achieve a combined physical and chemical template. This process gives a first surface energy on the substrate surface and a second surface energy on the physical templating posts. In these cases, the first SAM was deposited on a bare Si substrate. The HSQ templates were then fabricated, and the second SAM deposited on the templates.

Contact-angle measurements were taken for a number of SAM pairs and are shown in Table 2.3. The contact angles are shown for PTS as the first SAM, and either BTS or HTS as the second SAM. For all cases, a number of different processing conditions were tested. For PTS/BTS, longer salty development or UV/Ozone times generally led to lower contact angles (therefore higher SE). Similarly, for PTS/HTS, longer UV/Ozone times generally led to lower contact angle.

SAM Type / Order	Conditions	Contact Angle (deg): Static	Advancing	Receding
PTS/BTS	1 min salty development, 20 sec UV/Ozone in between SAMs	114.6	115.1	79.225
	4 min salty development, 20 sec UV/Ozone in between SAMs	108.35	104.8	78.6
	Simulate HSQ, 4 min salty development, then second SAM, then XX sec UV/Ozone	96.533	95.35	78.1
	Simulate HSQ, 4 min salty development, then second SAM, then 0 sec UV/Ozone	95.9	96.8	63.283
	Simulate HSQ, 4 min salty development, then second SAM, then 7 sec UV/Ozone	76.0167	76.683	53.3
	Simulate HSQ, 4 min salty development, then second SAM, then 16 sec UV/Ozone	75.33	77.383	52.8
	Simulate HSQ, 4 min salty development, then second SAM, then 20 sec UV/Ozone	67.716	71.683	45.9
	Simulate HSQ, 4 min salty development, then second SAM, then 40 sec UV/Ozone	67.216	68.616	44.5
PTS/HTS	Write HSQ, 4 min salty develop, 5 sec UV/Ozone in between SAMs	94.983	92.65	75.4
	Write HSQ, 4 min salty develop, 10 sec UV/Ozone in between SAMs	92.83	92.83	73.16
	Write HSQ, 4 min salty develop, 15 sec UV/Ozone in between SAMs	82.167	86.267	65.533

Table 2.3. Contact angle measurements for a number of different processing conditions. The top conditions are for PTS deposited first, and BTS deposited second. The bottom conditions are for PTS deposited first, and HTS deposited second.

Before templated self-assembly, it was important to determine BCP thin film self-assembly characteristics for substrates without physical post templates. Self-assembly results for two different SAM pairs (first/second: BTS/PTS and PTS/BTS) on Si substrates were achieved. For BTS/PTS in Figure 2.9, samples were exposed to varying times of UV/Ozone exposure between 0-32 sec in between the BTS and PTS SAM deposition steps. Exposure times of 24-32 seconds resulted in the best perpendicular lamellae PS-b-PMMA. To test the effect of HSQ on this process, Figure 2.10 shows images of for BTS/PTS when HSQ processing was simulated before varying UV/Ozone exposure times. The best perpendicular lamellae occurred with a UV/Ozone exposure time of 5 seconds. For higher exposure times, significant dewetting of the PS-b-PMMA thin film occurred. For PTS/BTS in Figure 2.11, samples were exposed to varying times of UV/Ozone exposure of 0-35 sec between the PTS and BTS SAM deposition steps. 15-20 seconds of exposure achieved the best perpendicular lamellae BCP assembly, though the thin film of BCP was considerably dewet from the substrate.

The three conditions above include PS-b-PMMA thin films with considerable amounts of dewetting. This was a common result in most experiments involving PS-b-PMMA on BTS or PTS SAM-coated substrates. Therefore, experimentally-measured contact angle vs. the degree of dewetting was tested. It was determined that a static contact angle of about 90° promoted wetting of PS-b-PMMA.

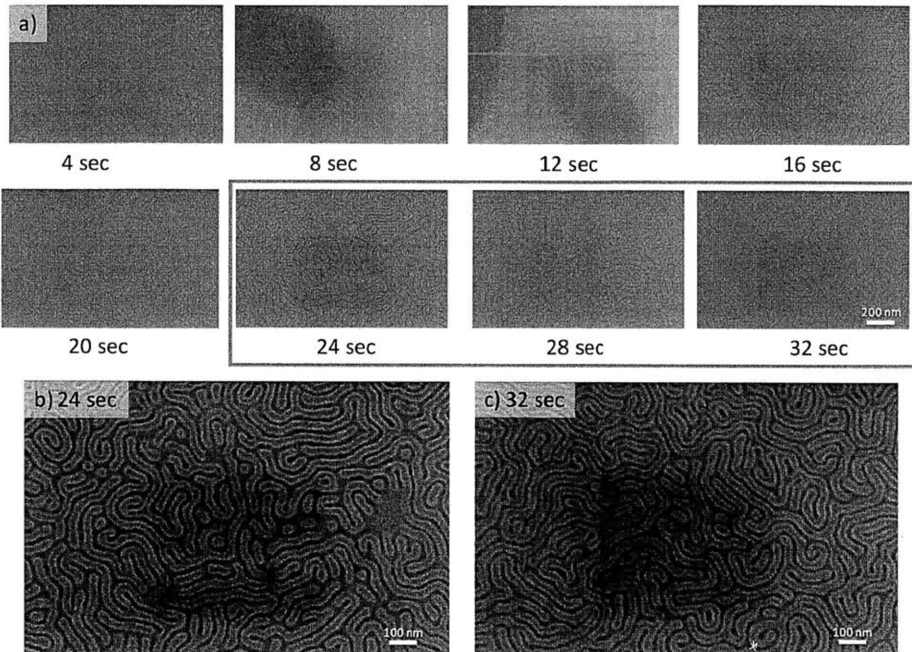

Figure 2.9: Top-down scanning electron micrographs of PS-block of PS-b-PMMA on SAM-coated Si substrate. a) Each sample was coated with BTS, exposed to UV/Ozone for the designated seconds, and coated with PTS. BCP was then spun on each sample and thermally annealed for self-assembly. BCP assembly for 24 (b) to 32 (c) seconds of UV/Ozone exposure had higher coherence length and less dewetting than lower exposure times. For the SEMs, thick light grey regions are PS-block, and dark grey interstitial regions the removed-PMMA-block.

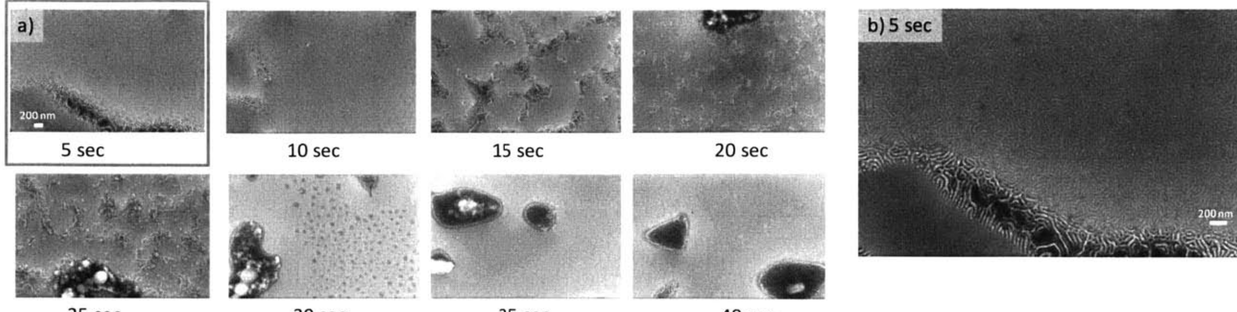

Figure 2.10: Scanning-electron micrographs of PS-block of PS-b-PMMA on SAM-coated Si substrate. (a) each sample was coated with BTS, HSQ process simulated, exposed to UV/Ozone for the designated seconds, and coated with PTS. BCP was then spun on each sample and thermally annealed for self-assembly. BCP assembly for 5 sec (b) of UV/Ozone exposure had higher coherence length and less dewetting than higher exposure times. For many samples, large regions are dewet of BCP for exposure times above 5 seconds, and the dark regions are agglomerated islands of BCP. For the SEMs, thick light grey regions are PS-block, and dark greay interstitial regions the removed-PMMA-block.

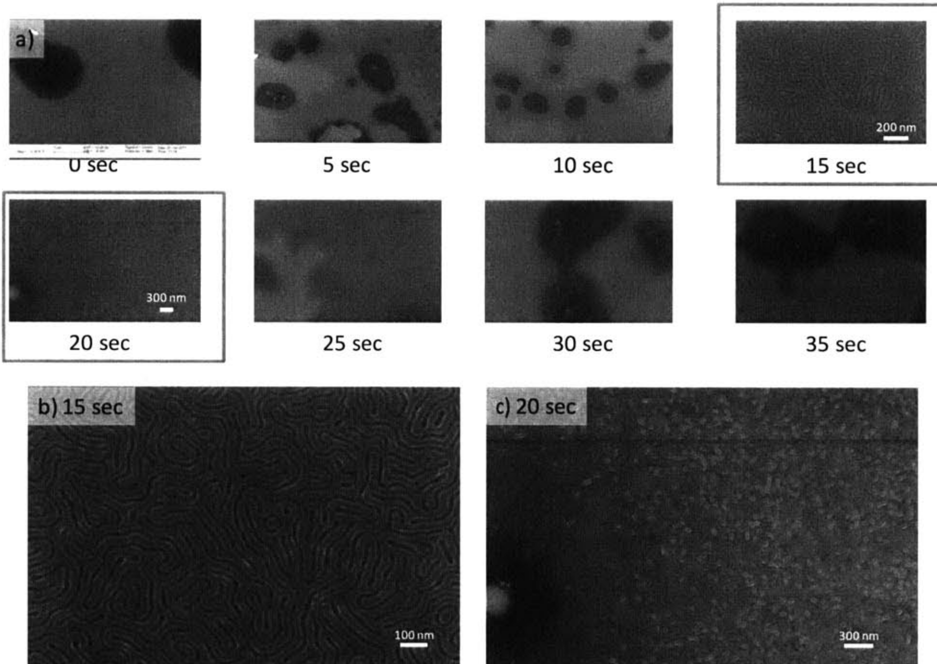

Figure 2.11: Scanning-electron micrographs of PS-block of PS-b-PMMA on SAM-coated Si substrate. (a) Each sample was coated with PTS, exposed to UV/Ozone for the designated seconds, and coated with BTS. BCP was then spun on each sample and thermally annealed for self-assembly. BCP assembly for 15 sec (b) and 20 sec (c) of UV/Ozone exposure had higher coherence length and less dewetting than other exposure times. For many samples, the very dark regions are agglomerated islands of BCP. For the SEMs, thick light grey regions are PS-block, and dark grey interstitial regions the removed-PMMA-block.

After determining the self-assembly characteristics on untemplated substrates, HSQ physical post templates were fabricated to achieve templated self-assembly with the BCP as is shown in Figure 2.12. Posts were fabricated in rectangular lattices and the templates were around 1 μm^2. These samples were coated with first and second SAM pairs of either BTS/PTS or PTS/BTS and the contact angle modified with varying times of UV/Ozone exposure as noted below. Generally, BCP thin film dewetting was a significant problem. A SE condition for adequate wetting of the substrate was achieved for substrates without physical post templates, but the introduction of the HSQ lithography process for the templates resulted in the BCP easily dewetting. Nonetheless, PS-b-PMMA was shown to be templated by arrays of HSQ posts at rectangular-periodic spacing.

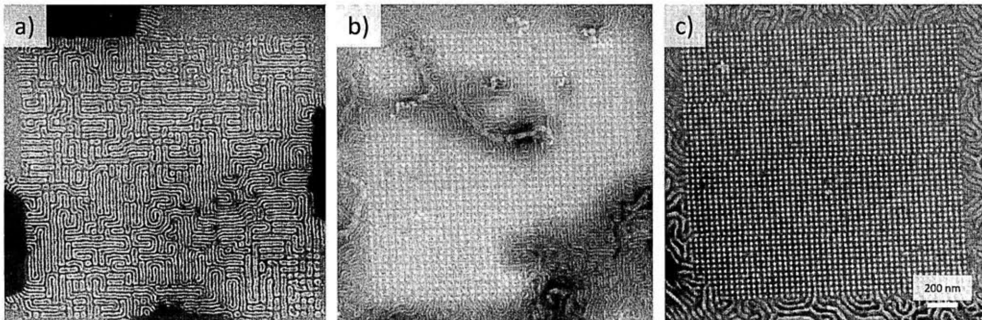

Figure 2.12: SEMs of templated PS-b-PMMA BCP self-assembly with various different templating schemes. a) Two SAM system of BTS/PTS with HSQ posts template in rectangular array (35 x 35 nm) (HSQ about 22 nm thick). The PS-b-PMMA is templated by the posts to align orthogonally to the template axes, though no long range order is observed. b) Two SAM system of PTS/BTS with HSQ posts template in rectangular array (47 x 47 nm) (HSQ about 20 nm thick) exposed to 17 seconds of UV/Ozone after the initial PTS deposition. The PS-b-PMMA is templated by the posts to align orthogonally to the template axes, though the templating effect is less than that in a). c) The PS-b-PMMA completely wets the templated region, though no order of the BCP is observed. It is possible that the template induced parallel orientation of the lamellae, whereas perpendicular orientation was observed in all surrounding regions. (42 x 40 nm) (HSQ about 25 nm thick) For all of these SEMS, the bright dots are HSQ templating posts, thick lighter regions are PS-block, and darker interstitial regions the PMMA-block. The larger "blobs" in b) are likely islands of thicker films of BCP compared to thinner surrounding regions.

2.4 Conclusion

HSQ templating posts were achieved on a SAM-coated sample by overcoming the issue of capillary collapse. Contact angle measurements were made for samples coated with different SAMs and modified

under a variety of conditions. The dewetting of a PS-b-PMMA thin film limited much of the experimentation to bare substrates, instead of including templates. To achieve wetted thin films, an adequate surface energy was determined for one- and two-SAM-coated samples. Post-array templated self-assembly was investigated for a number of different conditions. With these templates, PS-b-PMMA was successfully directed to align orthogonally to the template axes. Future work includes developing SAM modifications which results in full wetting of the PS-b-PMMA thin film as well as a larger variety of post-array patterns.

References

1. Ricardo Ruiz, Huiman Kang, Franois A. Detcheverry, Elizabeth Dobisz, Dan S. Kercher, Thomas R. Albrecht, Juan J. de Pablo, Paul F. Nealey, Density Multiplication and Improved Lithography by Directed Block Copolymer Assembly. *Science,* 321(5891) 936-939 (2008).
2. Kingsborough, Richard P. Goodman, Russell B. ; Fedynyshyn, Theodore H. Lithographically directed surface modification. *Journal of Vacuum Science & Technology B,* 27(6) 3031 - 3037 (2009).
3. Kingsborough, Richard P.; Goodman, Russell B.; Krohn, Keith; Fedynyshyn, Theodore H. Lithographically directed materials assembly. *Alternative Lithographic Technologies.* Ed. Frank M. Schellenberg & Bruno M. La Fontaine. San Jose, CA, USA: SPIE, 2009. 72712D-10.
4. Mark P. Stoykovich, Marcus Müller, Sang Ouk Kim, Harun H. Solak, Erik. Edwards, Juan J. de Pablo,Paul F. Nealey, Directed Assembly of Block Copolymer Blends into Nonregular Device-Oriented Structures *Science*, 308(5727) 1442-1446 (2005).
5. Sang Ouk Kim, Bong Hoon Kim, Kwanghyon Kim, Chong Min Koo, Mark P. Stoykovich, Paul F. Nealey and Harun H. Solak, Defect Structure in Thin Films of a Lamellar Block Copolymer Self-Assembled on Neutral Homogeneous and Chemically Nanopatterned Surfaces. *Macromolecules*, 39(16), 5466–5470 (2006).
6. Insik In, Young-Hye La, Sang-Min Park, Paul F.Nealey, and Padma Gopalan, Side-Chain-Grafted Random Copolymer Brushes as Neutral Surfaces for Controlling the Orientation of Block Copolymer Microdomains in Thin Films, *Langmuir*, 22 (18), 7855–7860 (2006).
7. Kim, S. O., Solak, H. H., Stoykovich, M. P., Ferrier, N. J., De Pablo, J. J., & Nealey, P. F. Epitaxial self-assembly of block copolymers on lithographically defined nanopatterned substrates. *Nature*, *424*(6947), 411–414 (2003).
8. Kingsborough, R. P., Goodman, R. B., & Fedynyshyn, T. H. Lithographically directed surface modification. *Journal of Vacuum Science Technology B Microelectronics and Nanometer Structures*, *27*(6), 3031–3037 (2009).
9. Joel K. W. Yang and Karl K. Berggren, Using high-contrast salty development of hydrogen silsesquioxane for sub-10-nm half-pitch lithography. *Journal of Vacuum Science and Technology B* 25, 2025 (2007).
10. Ion Bita, Joel K. W. Yang, Yeon Sik Jung, Caroline A. Ross, Edwin L. Thomas, and Karl K. Berggren, Graphoepitaxy of Self-Assembled Block Copolymers on Two-Dimensional Periodic Patterned Templates. *Science* **321**, 939 (2008).
11. Huigao Duan and Karl K. Berggren, Directed Self-Assembly at the 10 nm Scale by Using Capillary Force-Induced Nanocohesion. *Nano Letters* 10(9), 3710-3716 (2010).

Chapter 3: Assembly and Direction of a High-χ Polymer

Chapter 3 discusses the untemplated and templated self-assembly of a newly-synthesize BCP system. Fundamentally, for a BCP system with a given Flory-Huggins Interaction Parameter (χ), the BCP natural pitch (L_o) is a function of the degree of polymerization (N) and theoretically $L_0 \propto N^{2/3}$. L_0 can be reduced by decreasing N, though if N is decreased such that $\chi N < 10.5$, the BCP will not self-assemble[1]. By targeting a new BCP system with an increased χ, N can be decreased without $\chi N < 10.5$. If this is the case, L_0 of the new high-χ BCP can be driven below 20 nm for use in next-generation nanofabrication. This chapter discusses experimentation with a newly synthesized, potentially high-χ BCP system. The experiments 1) locally controlled the self-assembly of the new BCP system for complex nanopatterns and 2) led to a better understanding of the BCP's self-assembly characteristics.

In this chapter, a number of thin-film self-assembly processing parameters and templating schemes were tested and perfected. Due to the novel nature of the BCP system, some basic parameter set-points for the fabrication process had not been previously determined and were tested with a "clean slate". The thickness of the BCP thin film, temperature and time of the thermal anneal, process for block removal, and surface chemistry modification were all varied to determine the best self-assembly of each new BCP. The templated self-assembly of the new BCP system was also investigated, similar to Chapter 2. The template pattern-type, lattice, material, height and chemical modification were all tested parameters.

The objectives of the work in Chapter 3 were:

1) to determine ideal process parameters for adequate thin film self-assembly of the novel BCP system,

2) to determine the system's potential for complex or long-range-ordered nanostructures through template self-assembly,

3) and to achieve low L_0 through lower N polymers with possibly higher χ.

3.1 Discussion of High-χ

The Flory-Huggins Index, χ, is a measure of the chemical similarity/dissimilarity of two chemical materials[1]. For example, a conventional BCP such as poly(styrene-b-methylmethacrylate) has a positive χ-value of around 0.038[2], indicating that poly(styrene) (PS) and poly(methyl methacrylate) (PMMA) are chemically dissimilar. As a result, the L_0 of PS-b-PMMA has been typically reported around 25 nm[3]. This L_0 is possibly not low enough for next-generation nanofabrication[4], and is a result of the lower-χ nature of PS-b-PMMA compared to other BCPs. By targeting polymers with higher χ, there exists the potential to achieve thin film self-assembly with L_0 well below 20 nm for next-generation nanofabrication. An example of low L_0 as a result of high-χ is with an oligosaccharide/silicon-containing block copolymer MH-b-PTMSS or XGO-b-PTMSS that exhibited a feature size of 5 nm[5]. Furthermore, a high-χ BCP has the potential to achieve complex nanopatterns with complex templates[6-8].

The χ-value of a BCP is, among other factors, a function of the magnitude of the difference in the surface energy (SE) of the two polymer blocks. Therefore, a BCP can have a high χ-value when it is comprised of two blocks with significantly different SEs. Table 3.1 shows measured SEs for a number of common and of-interest homopolymers for BCP synthesis. Notably, the common BCP PS-b-PMMA has a measured SE difference of 6.7 dynes cm^{-1} (PS is 31.7 and PMMA is 38.4 dynes cm^{-1}). The table shows a large number of other potential homopolymers where the energy difference could be much higher than PS and PMMA.

Polymer	Polar Surface Energy (PSE) (dynes/cm)	Dispersive Surface Energy (DSE) (dynes/cm)	Total Surface Energy (SE) (dynes/cm)
poly(hydroxystyrene)	13.8	31.1	45
poly(methylmethacrylate)	7.4	31	38.4
poly(acetoxystyrene)	7.4	31	38.3
poly(2-vinyl-pyridine)	6.7	31	37.7
poly(methoxystyrene)	5.4	31.2	36.6
poly(styrene)	0.4	31.3	31.7
poly(FOHMAC)	6.9	18.9	25.8
poly(pentafluorostyrene)	2.4	17.7	20.1
poly(C6-ZFM)	2.4	10.7	13.1
Popular BCP ΔSE (dynes/cm) : PS-b-PMMA – 6.7 PS-b-P2VP – 6 PS-b-PEO - ~10 PS-b-PDMS – ~12			

Table 3.1: List of common and of-interest homopolymers and their respective measured surface energies. The pairing of two homopolymers with significantly different Total Surface Energy may result in a high-χ BCP. Popular BCPs are detailed at the bottom of the figure.

This research targeted two different homopolymers with different SEs, poly(octofluro pentamethacrylate) (OFPMA) and poly(hydroxystyrene) (HSM). To this end, OFPMA was fluoro-based, a characteristic that is linked to low SE. HSM was targeted because it is higher SE, and also is methacrylate-based such that it could be photolytically removed with a post-process. Table 3.1 shows that OFPMA-b-HSM has a SE difference of 18.2 dynes/cm, much higher than PS-b-PMMA (at ~6.7 dynes/cm) and higher than most conventional BCPs.

3.2 Description of Synthesize Polymers

Three different molecular weights (M_w) of OFPMA-b-HSM BCP, 51, 71 and 80 kg mol^{-1} were synthesized by collaborators at DuPont. Table 3.2 below summarizes the characteristics of the synthesized polymers. The BCPs had poly-dispersities close to 1.0 and the OFPMA:HSM volume ratio was targeted near 50:50 to achieve lamellar morphology.

Name	High ΔSE (dynes/cm)	Molecular Weight: M_w (kg/mol)	Poly-dispersity	Block Percentages – Volume %	Expected Morphology
ObAL50	18.2	92.4	1.154	43%-b-57%	Lamellae
ObAL60	18.2	151	1.339	44%-b-56%	Lamellae
ObAL80	18.2	175	1.159	47%-b-53%	Lamellae

Table 3.2: Characteristics of the different synthesized BCPs. The three different molecular weights were given experimental names ObAL50, ObAL60, and ObAL80. Each of the BCPs was synthesize from the same homopolymers, and therefore the ΔSEs were the same. Notably, the Poly-disperity is close to 1, and the Block Percentages were targeted for lamella morphology.

The major steps of the fabrication process are summarized in Figure 3.1. In order to produce hydrogen silsesquioxane (HSQ) physical template posts, a thin film of HSQ was first spun on the samples (in solution with methyl isobutyl ketone (MIBK), thicknesses of 25-33 nm) with no post-bake. Templates were exposed with scanning-electron-beam lithography (SEBL) on a Raith 150 system (30keV, 30 μm objective aperture, 6 mm working distance, ~275 pA). After exposure, the samples were developed with a salty developer (4% NaCl / 1% NaOH in deionized water) at 24°C for 4 minutes, then rinsed with deionized water for 2 minutes and blown dry under N_2. HSQ is a negative-tone resist and therefore the unexposed resist is removed by the developer solution.

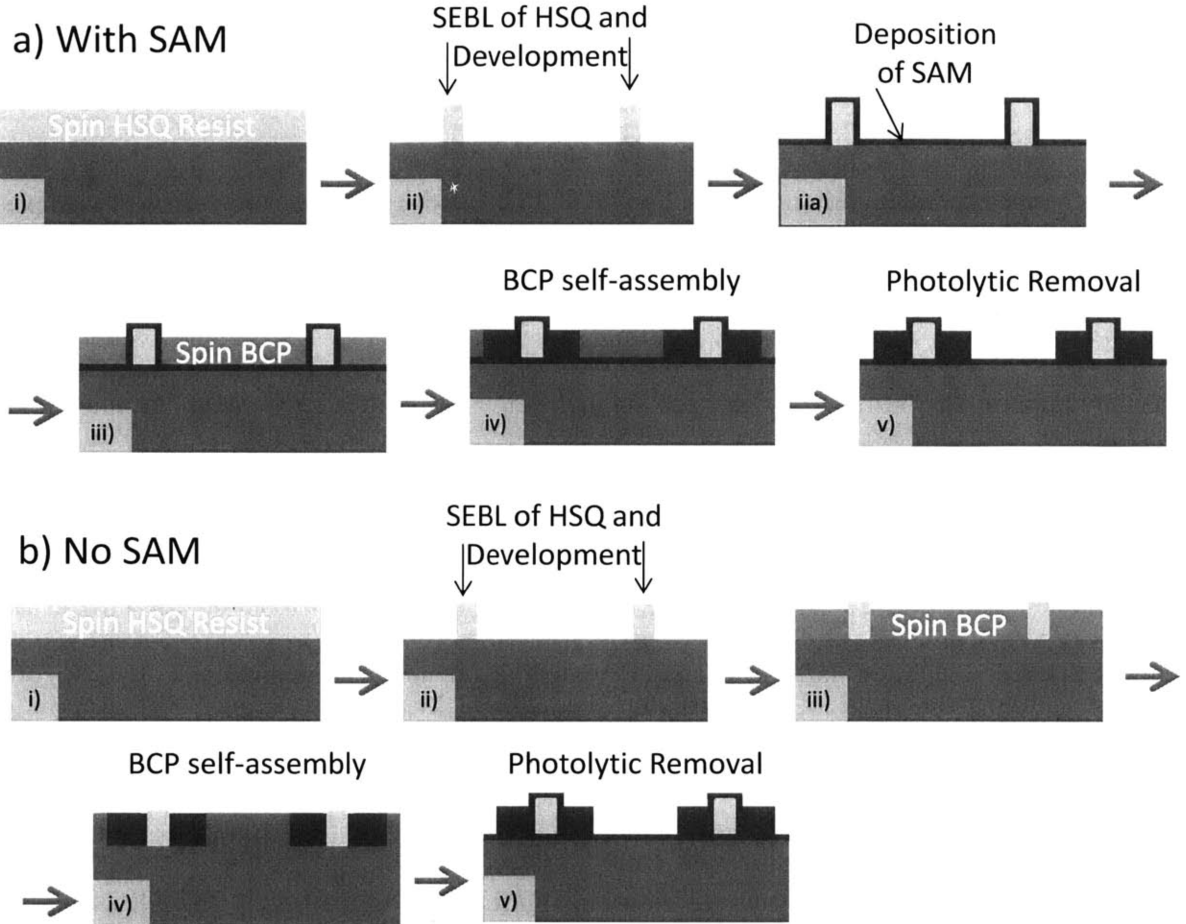

Figure 3.1: Major Steps of the fabrication process. a) includes the deposition of a self-assembled monolayer (SAM) after lithography of the HSQ templating features. b) does not include the SAM deposition. The steps include: i) spinning of HSQ resist to the desired thickness, ii) SEBL of the templating features that includes exposure in the SEBL system, as well as development, iia) deposition of the SAM for the applicable samples, iii) spinning of the BCP to the desired thickness, iv) self-assembly of the BCP with thermal annealing, and v) photolytic removal of the OFPMA block of the BCP.

A self-assembled monolayer (SAM) was deposited on some of the samples, as is shown in Figure 3.1a. Deposition was initiated by soaking a prime Si wafer in a bath of CD26 (MICROPOSIT MF -CD-26 DEVELOPER, Dow Corning, Inc.), which contains a solution of 2.5 wt. % tetramethylammonium hydroxide (TMAH) to fully hydroxyl-terminate the native silica surface. The wafer was rinsed with deionized water for 2 min, and blown dry under N_2. A SAM solution was prepared by mixing 100 μL of the desired SAM molecule in 100 mL toluene (J.T. Baker 99.9%) and letting set for 10 minutes. The wafer was immersed in this solution for 20 minutes to deposit the SAM, rinsed with toluene, and then

blown dry under N_2[9]. Samples were baked on a hotplate at 120°C for 5 minutes. Samples were exposed to UV/Ozone for varying periods of time (conditions noted in results below). Some of the samples were not deposited with a SAM (Figure 3.1b).

The synthesized lamellae-forming BCPs (2 wt. % in 2-heptatnone) were spin-coated on the samples at varying spin speeds of 1500-7500 rpm. In order to evaporate remaining solvent after spin coating, samples were baked on a hot plate at 120°C for 1 minute. The BCP-coated samples were thermally annealed by purging the oven with N_2 gas, turning the oven to the desired temperature, turning the oven off after the desired time (typically 2 hours), and venting the oven after cooling to room temperature over 6 hours. The removal of the methacrylate-based OFPMA-block was tested with a number of different methods and is described below. Imaging of the final BCP pattern was carried out on a Raith 150 SEBL system (a LEO SEM column, 10keV, 30 μm objective aperture, 6 mm working distance).

In order to increase the imaging contrast of the final BCP pattern, photolytic removal of the methacrylate-based OFPMA-block was tested with two different methods. Both 193-nm laser and 220-nm light exposure were tested and the results are shown in Figure 3.2. To exemplify the low-SEM-contrast of a non-removed BCP film, Figure 3.2a shows the final BCP pattern without any post-process photolytic removal. The imaging contrast between the blocks is not adequate to discern the resulting BCP nanostructures. Figure 3.2b shows the final BCP pattern after a 193-nm exposure dose of ~700 mJ/cm^2 and a 1 minute development in 1:1 isopropanol:methyl isobutyl ketone. This dose of 193-nm, as well as other doses led to the removal of almost all of the BCP. In Figures 3.2c and 3.2d, the BCP thin film was exposed to 200-nm light for two different amounts of time, and similarly solvent developed. A 5-minute exposure improved the imaging contrast (compared to the BCP pattern in Figure 3.2a), but a 15-minute exposure was ideal for photolytic removal and imaging contrast improvement.

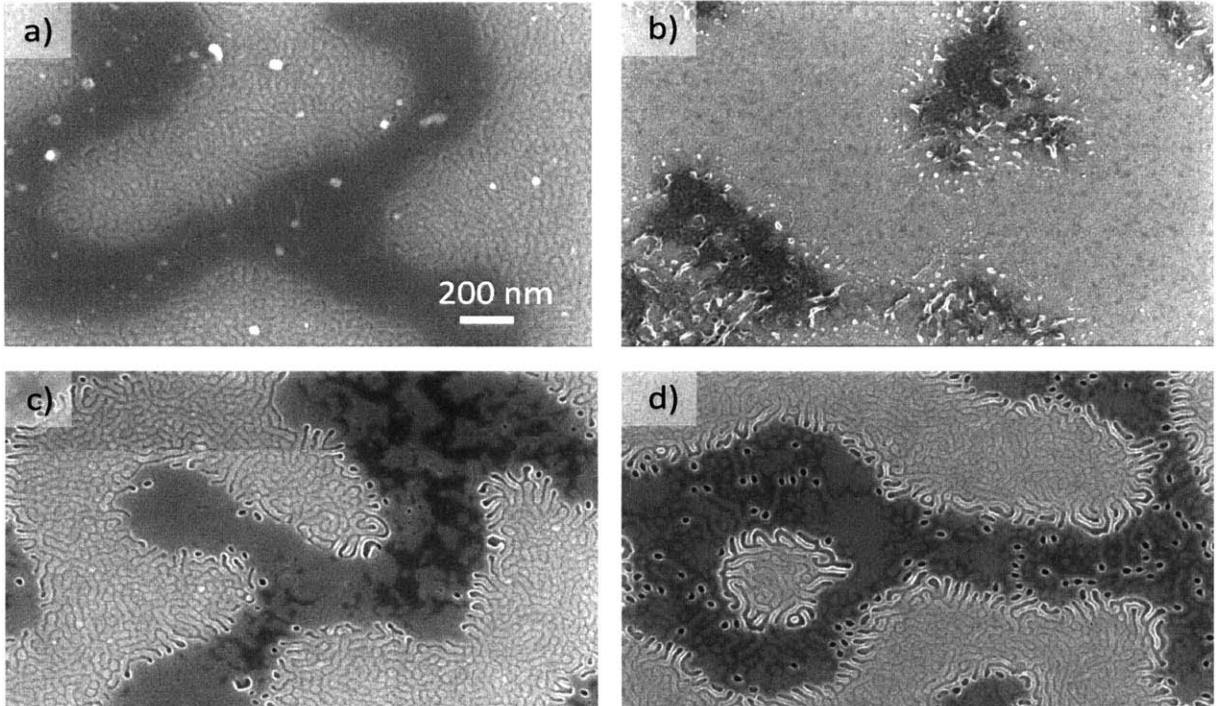

Figure 3.2: Top-down scanning-electron micrographs of ObAL60 BCP after different methacrylate-block removal steps. a) No removal step resulted in a small amount of contrast between the blocks. b) ~700 mJ/cm^2 dose of exposure to a 193-nm laser followed by 1 minute of development in 1:1 IPA:MIBK. For all reasonable doses and development times, the 193-nm laser exposure resulted in a completely removed BCP film. c) and d) 5 minutes and 15 minutes exposure to a 220-nm lamp followed by 1 minute of development in 1:1 IPA:MIBK. 15 minutes exposure resulted in the best photolytic removal of the methacrylate-based OFPMA block as can be noted from the high BCP contrast. For all images, the larger dark regions were likely regions of agglomerated BCP where a top-surface styrene-based-block was present and inhibited the phyotolytic removal. The light and dark gray color is the HSM-block and removed-OFPMA-block, respectively.

3.3 Thermal Annealing

Thin films of the BCPs were thermally annealed in a nitrogen-purge environment to achieve self-assembly. A number of the annealing parameters were tested and the best conditions were determined to achieve thin films of high-quality self-assembled BCP. Imperfections such as low coherence length and blobs/islands of BCP were observed and different annealing parameters were tested to reduce these imperfections. The temperature ramp-down rate and annealing time were tested and are presented below.

In an attempt to increase coherence length, the temperature ramp-down time of the thermal anneal temperature was increased. After the oven was turned off at the end of a typical thermal anneal, the temperature dropped from the maximum (around 230°C) to below 180°C in less than 30 minutes. The

ramp-down was tested by specifically controlling the temperature for a ramp-down time of over 1.5 hours. Figure 3.3 shows example BCP patterns from a typical ramp-down (less than 30 minutes), and a ramp-down of 1.5 hours. Figure 3.3a demonstrates the organization of ObAL60 with a typical ramp-down. Figure 3.3b illustrates the organization of the BCP with the controlled and longer ramp-down. In this example, no distinguishable improvement in BCP assembly was observed as a result of a controlled and longer ramp-down. Furthermore, the total time of the thermal anneal was increased in an attempt to increase the coherence length. Thermal annealing times of 4, 8 and 12 hours were tested in comparison to the typical 2 hours. This increase in thermal annealing time didn't result in a distinguishable improvement in ObAL60 assembly.

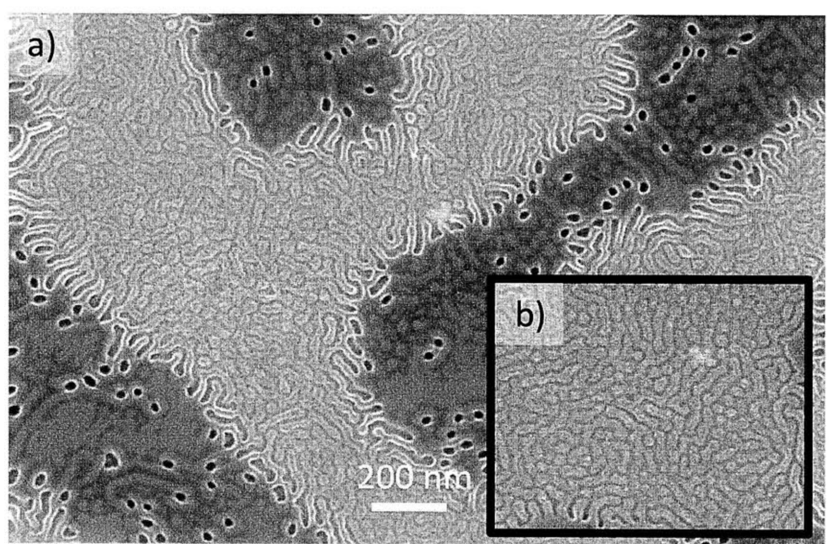

Figure 3.3: Top-down scanning-electron micrograph of ObAL60 BCP for different ramp-down times during thermal annealing. a) is a typical thermally annealed BCP thin film with a typical ramp-down time of less than 1 hour. b) is a thermally annealed BCP thin film with a longer ramp-down. This ramp-down did not seem to have a significant effect on the coherence length of the assembly or density of BCP defects. The light and dark gray color is the HSM-block and removed-OFPMA-block, respectively.

The natural pitch, L_0, of thin films of self-assembled was measured to be 31, 38 and 45 nm for ObAL50, ObAL60, and ObAL80, respectively (Figure 3.4). These values are not quite sub-20 nm for next-generation nanofabrication. Although these results did not achieve the objective of a low L_0, the synthesize BCPs were relatively high M_W compared to other conventional BCPs. Therefore, in the future the M_w can be decreased by an order of magnitude to further decrease L_0.

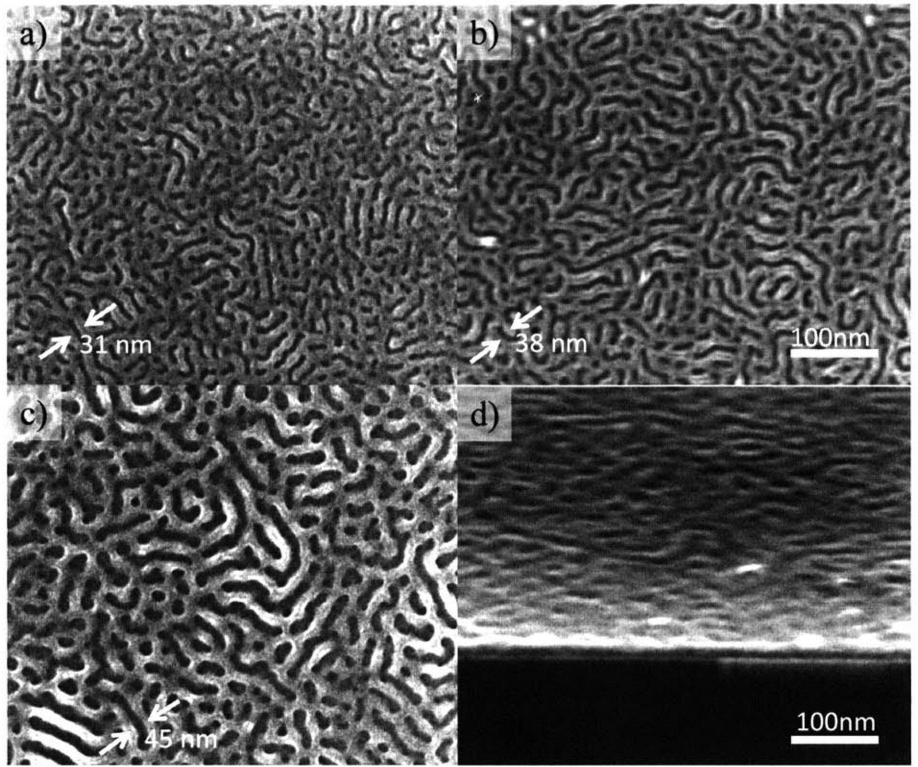

Figure 3.4: Scanning-electron micrographs of self-assembled thin films of all synthesized BCPs and measurements of the BCP nature pitches (L_0). a) ObAL50 BCP with a measured L_0 of 31 nm. b) ObAL60 BCP with a measured L_0 of 38 nm. c) ObAL80 BCP with a measured L_0 of 45 nm. d) Side view of ObAL60. The light and dark gray color is the HSM-block and removed-OFPMA-block, respectively.

3.4 Chemical Templating

Templating of the self-assembly of the BCPs was tested for a number of different templating schemes. All of the schemes were previously successful in directing the self-assembly of other conventional BCPs. Therefore, these schemes served as reasonable benchmarks to determine the ability of OFPMA-b-HSM self-assembly to be directed by templates. Chemical templating was initially tested, and is similar to that discussed in Chapter 2. (Physical templating reported later). A SAM of hexyltrichlorosilane was deposited on a bare Si substrate. The SAM was exposed with a patterning scheme similar to the line grating array in Figure 3.5. Grating pitches varied from 34 to 42 nm with SEBL linear-dose-densities of 1000 to 79500 pC cm^{-1}. Before self-assembling the BCP, the samples were exposed to 0-30 seconds of UV/Ozone. An example of the final BCP pattern is shown in Figure 3.6. Generally, chemical templating

did not result in direction of ObAL60 self-assembly (similar results expected for OBAL50 and ObAL80). Most notably, the image in Figure 3.6 seems to show an agglomeration of the BCP in the area of the chemical template (outlined in red). An interesting future investigation would be metrology of the agglomerated are to determine thickness changes from chemical templating.

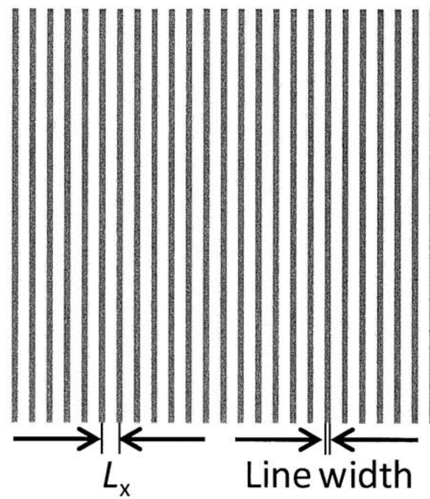

Figure 3.5: Schematic of line grating array used for chemical templating. The L_x, the distance between template lines, was widely varied. The line width was controlled by varying the linear-dose-density of the electron beam exposure.

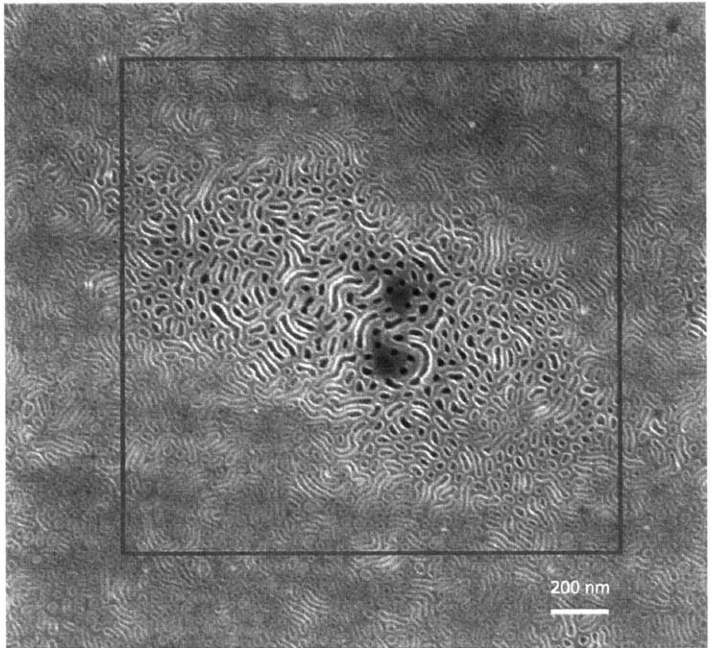

Figure 3.6: Scanning-electron micrograph of **ObAL60** templated by a chemical line grating array as outlined in red. The grating was written into the SAM underneath the BCP assembly. After SAM deposition, the sample was exposed to UV/Ozone for 15 seconds. No significant degree of directed self-assembly was observed for the varied L_x and linear-dose-density. There seems to be some agglomeration of the BCP in the templated region, though no further metrology was performed to determine the height of this region. The light and dark gray color is the **HSM**-block and removed-**OFPMA**-block, respectively.

3.5 Physical Templating

Physical templating of the BCPs was also performed and resulted in direction of self-assembly, in contrast to chemical templating. A wide variety of template schemes were patterned into HSQ resist and examples of these are shown in Figure 3.7. Templating schemes included line-grating arrays (Figure 3.7a) and rectangular-dot arrays (Figure 3.7b).

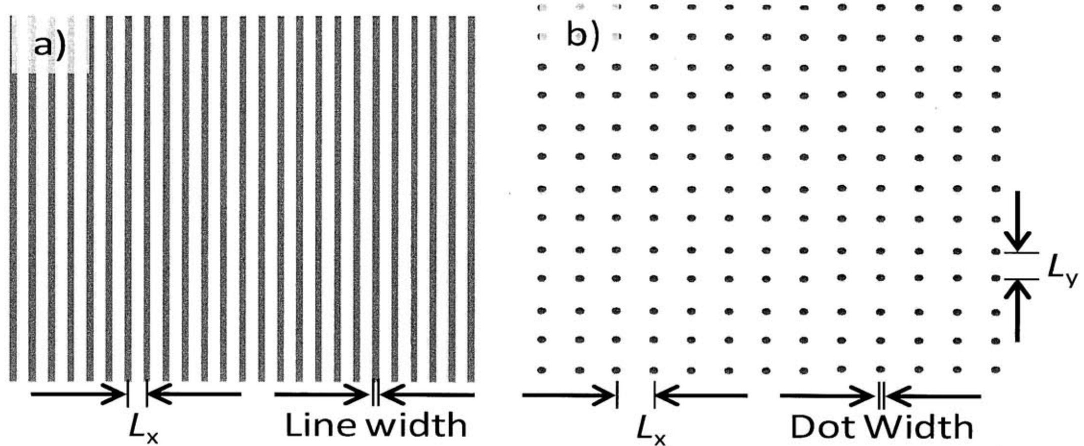

Figure 3.7: Schematics of template schemes (a) line-grating array and b) dot array. Schemes such as these were used for physical templating with HSQ resist written by scanning-electron-beam lithography (SEBL). For both, L_x and L_y were widely varied. The Line and Dot Widths were varied by controlling the linear dose density or dot dose of the electron-beam exposure, respectively.

Physical templates, coated with a SAM, directed the self-assembly of ObAL60 and results are shown in Figure 3.8. The SAM deposition was carried out after the development of the HSQ resist, and before the spin-coating of the ObAL60 thin film. Generally, this templating was not successful in significantly directing the self-assembly: the lack of direction seemed to results from the templating features interfacing with both blocks of the block copolymer, in contrast to previously reported physical templates that preferentially attracted only one of the blocks. Figure 3.8a is a close-up SEM that shows ObAL60 in a linear-grating-array template. The BCP is slightly directed to be parallel to the HSQ resist lines. Figure 3.8b shows ObAL60 in a rectangular-dot-array template. The HSM-block assembles around and webs between the templating posts. After initial experiments with SAM-modified templates, it was determined that the BCPs self-assembled better on substrates without a SAM coating, and therefore the above investigation was suspended.

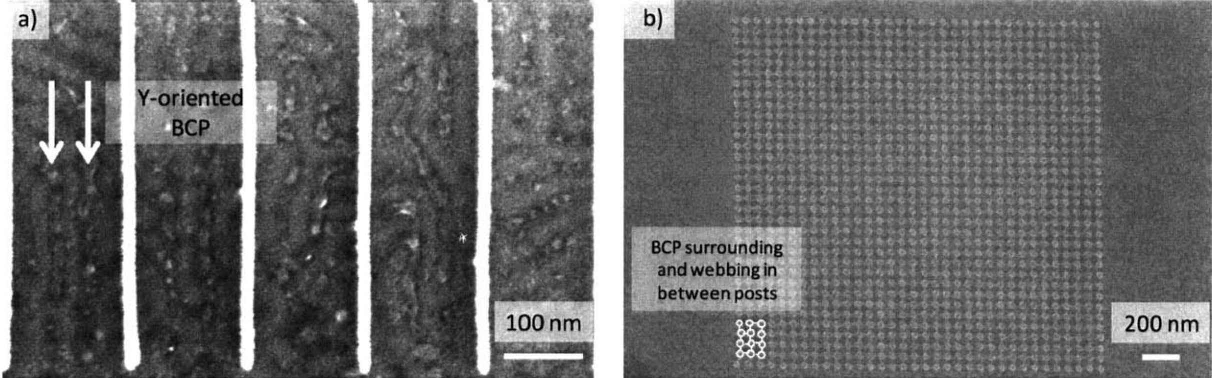

Figure 3.8: Scanning-electron micrographs of ObAL60 with HSQ physical templates. a) BCP self-assembled in a grating of lines. The bright y-oriented lines are HSQ templating fences making up the line-grating array. The contrast in between these lines is the HSM-block of ObAL60. On the leftmost side of the image, the BCP is shown to be oriented in the y-direction with the HSQ lines (highlighted by the white arrows). Generally, this orientation did not occur over a large portion of the templated area. b) ObAL60 self-assembled in a dot-array template. The bright dots are HSQ posts, and the HSM-block assembled to surround the posts. Furthermore, the HSM seems to "web" in between the posts, that is not the case in the more disordered region outside of the templated area, and the webbing is therefore a result of the post template. The surround and webbing BCP is highlighted with white lines.

In extension to the above work, the majority of the physical templating experimentation was carried out on bare Si substrates with bare HSQ templates (in contrast to SAM-coated templates). Figures 3.9 and 3.10 show the best of these templating results. The templates had one or two major axes (the x- and/or y-direction) and the BCP was templated to orient parallel to either or both of these axes. Figure 3.9 shows SEMs of templated ObAL80 patterns that exemplify these cases. In Figure 3.9a, the BCP pattern forms a grid that is oriented parallel to either of the major axes (x- and y-direction), while it is parallel to the template major axis (y-direction) in Figure 3.9b, and perpendicular to the template major axis (y-direction) in Figure 3.9c. The results shown in Figure 3.9c are most typical for linear-grating-array templates. The difference in grid orientation between Figure 3.9a and 3.9b are a result of difference in post pitch (32 vs. 80 nm) and BCP spin-speed (2500 vs 7500 rpm). The grid orientation in figure 3.9c is different because it is a result of a line-grating array instead of a dot-array template.

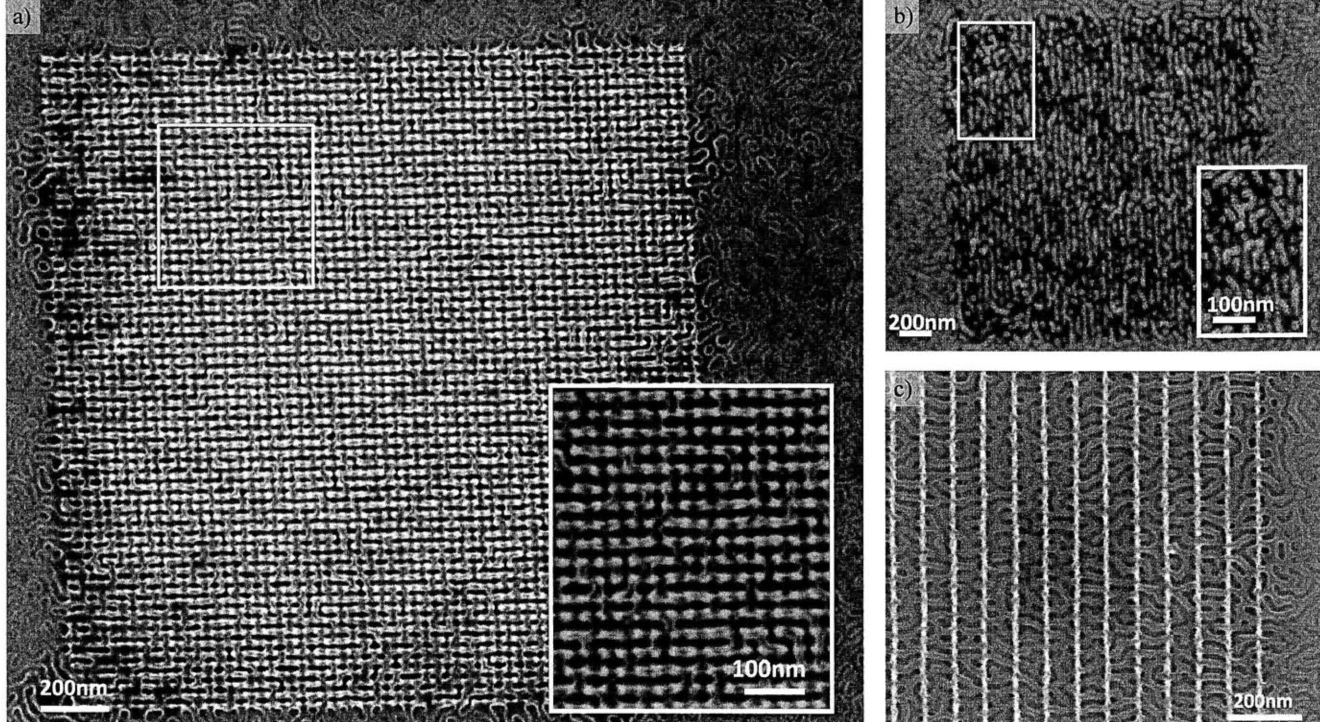

Figure 3.9: Scanning-electron micrographs of BCPs templated by various physical templates. a) ObAL80 templated by an HSQ-dot array with L_x and L_y of 32 nm. Posts were 29 nm tall and BCP was spin-coated at 2500 rpm. The BCP is directed to orient orthogonal to both the x- and y-directions in the template. The inset shows a close up of the highlighted region. b) ObAL80 templated by an HSQ line-grating-array with L_x of 80 nm. Fences were 26 nm tall and BCP was spin-coated at 7500 rpm. The BCP was directed to orient parallel the y-direction and the linear templating features. The inset shows a close up of the highlighted region. c) ObAL80 templated by an HSQ line grating array with L_x of 83 nm. Fences were 29 nm tall and BCP was spin-coated at 1500 rpm. The BCP is directed to orient parallel to the x-direction and perpendicular to the linear templating features. For all images, the bright objects are the templating features. The light and dark gray background is the HSM-block and removed-OFPMA-block, respectively. The light and dark gray color is the HSM-block and removed-OFPMA-block, respectively, and the white color is HSQ.

Physical templating comprised of short dot-arrays of thin HSQ (~15 nm thick, 1% in MIBK, 8000 rpm, 10 acceleration (a.u.), 60 sec) also templated BCP self-assembly. Generally, OFPMA blocks were attracted to the HSQ post with examples shown in Figure 3.10. Though ObAL80 and ObAL50 BCPs did not orient predominantly parallel to a major template axis as was the case with the results in Figure 3.9, the short dot-array templates seemed to interact with the BCP enough to change the self-assembly.

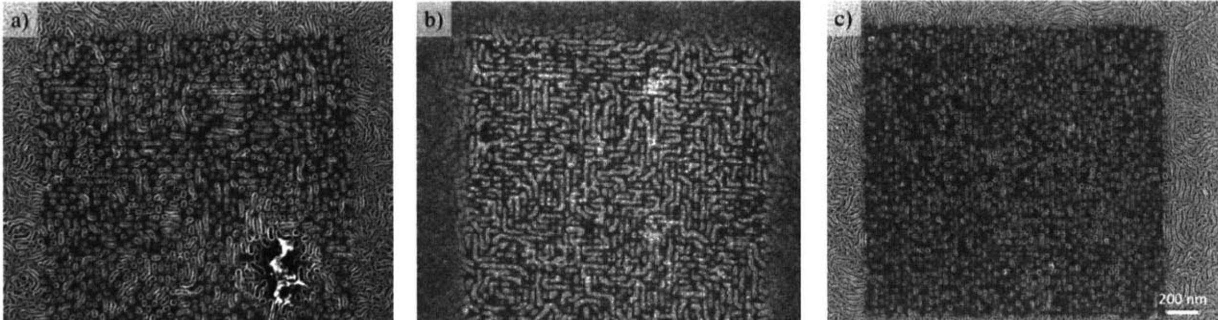

Figure 3.10: Top-down scanning-electron micrographs of ObAL80 and ObAL50 templated by short HSQ post-arrays. The posts were fabrication from 1% HSQ in MIBK at 8000 rpm for 60 sec and 10 acceleration (a.u.). The BCP patterns in (a), (b) and (c), are good examples of results achieved for a large variety of post-array pitches. a) ObAL80 is templated by a square array of HSQ Posts(~45 nm pitch, dose ~50 fC dot^{-1}, BCP spin-coated at 2500 rpm, 60 sec, 0 acceleration (a.u.)). b) ObAL80 is templated by a square array of HSQ Posts. (~42 nm pitch, dose ~50 fC dot^{-1}, BCP spin-coated at 7500 rpm, 60 sec, 0 acceleration (a.u.)) c) ObAL50 is templated by a square array of HSQ Posts. (~40 nm pitch, dose ~50 fC dot^{-1}, BCP spin-coated at 3000 rpm, 60 sec, 0 acceleration (a.u.)) All samples were thermally annealed at 160°C. The light and dark gray color is the HSM-block and removed-OFPMA-block, respectively, and the white color is HSQ.

Another significant templating result was the direction of ObAL60 and ObAL80 to form meshes of nanoholes as a result of dot-array templating (Figure 3.11). These templates were characterized by particular post pitches: the x-pitch was smaller than L_0 (eg. 20 nm in Figure 3.11 SEMs) and larger than L_0 (eg. 50-66 nm in Figure 3.10 SEMs). In this manner, a full natural pitch, L_0, of BCP was "restricted" from fitting in between the x-direction posts, but was "free" to fit in between the y-direction posts. Therefore, the centroids of the holes generally aligned in rows along the x-direction. There seemed to be little correlation between holes in the y-direction (the tightly-spaced posts in the x-direction limit the coherence of the holes from row to row). Furthermore, likely because of the rectangular nature of the post template, the shape of the nanoholes is also rectangular. Figures 3.11a-c show the results of directed self-assembly with rectangular post arrays for (L_x,L_y) pitches of (20,50), (20,60) and (20,66) nm. The diameter of the holes scaled with the y-pitch of the template in these cases, though this result was not quantified. Lastly, a number of defects existed in the meshes and are categorized as missing holes or conjoined holes. For the missing holes, it is speculated that a layer of HSM capped the hole and therefore the HSM was not removed during the photolytic removal. Conjoined holes seem to be local free-energy minimizations due to the strain imparted on the BCP as a result of the x-pitch being smaller than L_0.

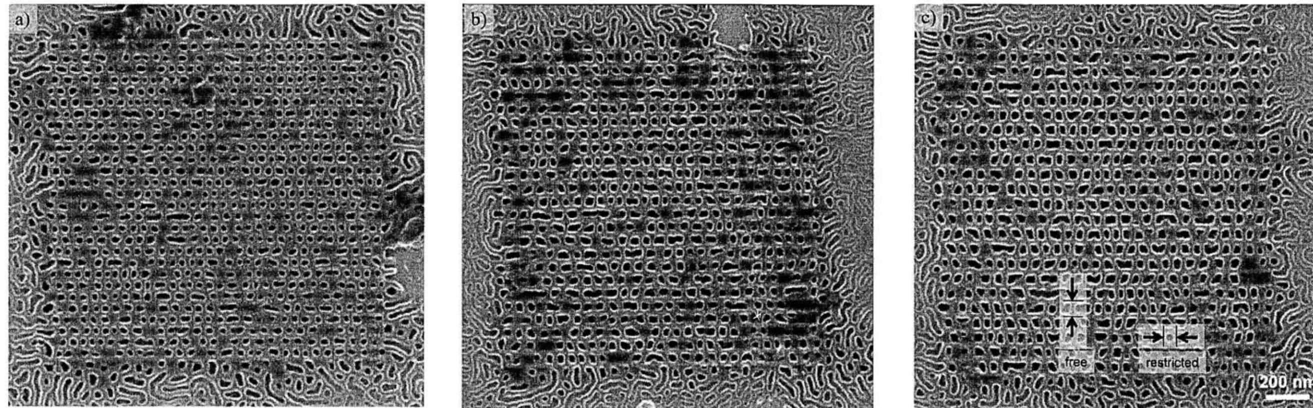

Figure 3.11: Top-down scanning-electron micrographs of BCPs templated by various physical templates. a-c) ObAL60 templated by an HSQ-dot array with (L_x,L_y) of (20,50), (20,60), and (20,66) nm, respectively. Posts were 33 nm tall and the BCP spun at 1500 rpm. The BCP is directed by the template to form meshes of holes. The holes align along the x-direction, perpendicular to the "free" direction. There is little correlation between holes in different rows, and therefore limited control in the y-direction, perpendicular to the "restricted" direction. The size of the holes increased as a function of L_y. These results are the best examples of DSA of the synthesized BCPs. Outside of the templated region, the BCP is not directed in any particular manner. The light and dark gray color is the HSM-block and removed-OFPMA-block, respectively. The HSQ template features are not visible underneath the HSM-block.

Furthermore, post-array templates in a hexagonal lattice, both of HSQ and cross-linked poly(methyl methacrylate) (PMMA) resist, and small-L_x line-grating array templates directed BCP self-assembly as is shown in Figure 12. A hexagonal array of HSQ posts produced ObAL80 nanoholes with widely-varying diameters (~50-100 nm) and shapes (circular to worm-like) (Figure 12a). When ObAL80 was tempalted by a line-grating array of HSQ fences with a small L_x, nanoholes aligned parallel to the templating features (Figure 12b). These results are very similar to those shown in Figure 3.11, though the shape of the holes were less consistent in the below Figure. Lastly, poly(methyl methacrylate) as a negative-tone resist[10] was used to fabricated templates for the direction of ObAL80 (Figure 3.12c). The results were also very similar to those in Figure 3.11. Generally, none of the results showed a higher degree of direction as compared to results in Figures 3.9 and 3.11.

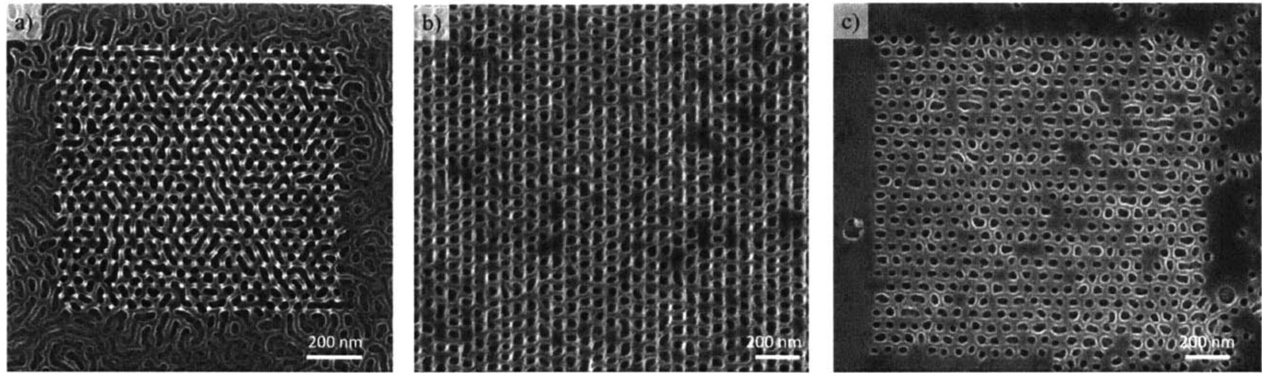

Figure 3.12: Top-down scanning-electron micrographs of BCPs templated by various physical templates. a) Hexagonal arrays HSQ posts also slightly order the ObAL80 assembly, though the nanoholes are of different shapes and sizes within the templated area. (18 fC dot^{-1}, 32 nm pitch, 2% HSQ spun at 4500 rpm, BCP spun at 1500 rpm). b) Line-grating array acting as a template for ObAL80. The y-direction HSQ fences align nanoholes in the y-direction, with no correlation from column to column. (1300 pC cm^{-1}, 50 nm pitch, 2% HSQ spun at 4500 rpm, BCP spun at 1500 rpm) c) Nanoholes were fabricated from ObAL80 with a dot-array template of poly(methyl methacrylate) (PMMA) posts. (72 fC dot^{-1}, PMMA spun at 3000 rpm, BCP spun at 1500 rpm). All samples were thermally annealed at ***°C. The light and dark gray color is the HSM-block and removed-OFPMA-block, respectively, and the white color is HSQ.

3.6 Summary and Conclusion

Templated self-assembly was achieved for newly synthesized, high-χ BCPs. The ramp-down time and annealing time were experimentally tested and it was found that these variations did not improve the final BCP pattern coherence length. As for templating, it was shown that chemical templating in a hexyltrichlorosilane SAM did not direct self-assembly. As opposed to chemical templates, physical templates of HSQ of dot- and line-grating array schemes were successful in directing the BCP self-assembly. The BCP self-assembled to align orthogonally to the major template axes or achieve nanohole meshes. In the end, the nanostructures fabricated by these templates were less ordered than reported nanostructures for PS-b-PMMA or other research BCPs.

References

1. Bates, F. S., & Fredrickson, G. H. Block Copolymer Thermodynamics: Theory and Experiment. *Annual Review of Physical Chemistry*, 41(1), 525–557 (1990).
2. Thomas P. Russell Rex P. Hjelm, Jr., and Phil A. Seeger, Temperature Dependence of the Interaction Parameter of Polystyrene and Poly(methyl methacrylate). *Macromolecules* 23, 890-893 (1990).
3. [A,-3] Liu, G. L., Nealey, P. F., Ruiz, R., Dobisz, E., Patel, K. C., & Albrecht, T. R. Fabrication of chevron patterns for patterned media with block copolymer directed assembly. *Journal of Vacuum Science Technology B*, *29*(6). (2011).
4. The International Roadmap for Semiconductors: *2011*
5. Cushen, J. D., Otsuka, I., Bates, C. M., Halila, S., Fort, S., Rochas, C., Easley, J. A. Oligosaccharide/Silicon-Containing Block Copolymers with 5 nm Features for Lithographic Applications. *ACS nano*, *6*(4), (2012).
6. Joel K. W. Yang, Yeon Sik Jung, Jae-Byum Chang, R. A. Mickiewicz, A. Alexander-Katz, C. A. Ross and Karl K. Berggren. Complex self-assembled patterns using sparse commensurate templates with locally varying motifs. *Nature Nanotech.* 5, 256-260 (2010).
7. Ion Bita, Joel K. W. Yang, Yeon Sik Jung, Caroline A. Ross, Edwin L. Thomas, and Karl K. Berggren, Graphoepitaxy of Self-Assembled Block Copolymers on Two-Dimensional Periodic Patterned Templates. *Science* **321**, 939 (2008).
8. Stoykovich, M. P., Müller, M., Kim, S. O., Solak, H. H., Edwards, E. W., De Pablo, J. J., & Nealey, P. F. Directed assembly of block copolymer blends into nonregular device-oriented structures. *Science*, *308*(5727), 1442–1446 (2005).
9. Joel K. W. Yang and Karl K. Berggren, Using high-contrast salty development of hydrogen silsesquioxane for sub-10-nm half-pitch lithography. *Journal of Vacuum Science and Technology B,* 25, 2025 (2007).
10. Huigao Duan, Donald Winston, Joel K. W. Yang, Bryan M. Cord, Vitor R. Manfrinato, and Karl K. Berggren, Sub-10-nm Half-Pitch Electron-Beam Lithography by Using PMMA as a Negative Resist. *Journal of Vacuum Science and Technology B,* 28 C6C58-C6C62 (2010).

Chapter 4: Lithographic Overlay of Negative-tone Resist Features

Chapter 4 discusses the overlay accuracy of lithographic features for the fabrication of combined templates with a Raith 150 scanning-electron-beam tool. Overlay of different lithographic write-steps is a common process step for many applications[1-4]. Typically, a given application has an overlay accuracy requirement of many tens or hundreds of nanometers. In the application of block copolymer (BCP) templated self-assembly, the overlay accuracy must be smaller than the BCP natural pitch, L_0, typically close to 10 nm. This requirement presents a significant challenge for scanning-electron-beam lithography systems (SEBL). In this chapter, the process used to obtain the best overlay accuracy is presented to achieve a final overlay accuracy of ~52 nm and 0°. This process contributed indirectly to the overall objectives and challenges of 1) locally controlling the self-assembly of BCPs for complex nanopatterns and 2) a better understanding of the self-assembly characteristics of BCPs.

4.1 Combined Templating Objective

As was discussed in previous chapters, combined physical and chemical templating for BCP templated self-assembly may achieve higher local control and long-range order than either physical or chemical templating individually. Double patterning, a process that involves two lithographic writes on the same substrate, can be used to fabricate a combined physical and chemical template. For example with scanning-electron-beam lithography, the first write can fabricate post or fence physical templates on top of the substrate from a negative-tone resist. The second write can deliver energy to a local spot on the surface and therefore modify the spot's chemical properties. With these two steps, both physical and chemical features will exist on the same substrate to act as a combined template. In Figure 4.1, a schematic is shown of this example.

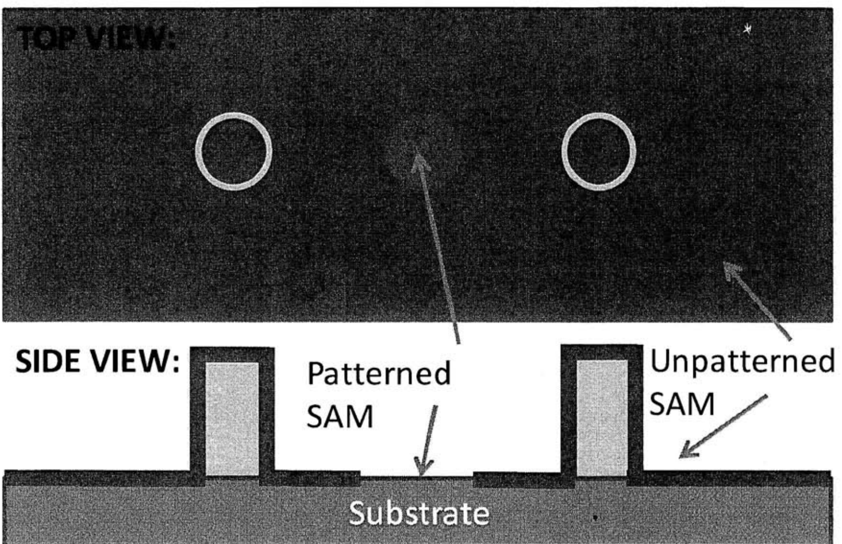

Figure 4.1: Schematic of a double pattern of combined chemical and physical templating. In this figure, there are both physical and chemical template features. The physical template features are the grey posts standing off the substrate surface. These can be patterned by electron-beam lithography in a first write step. The chemical template features are the contrast between the blue, unpatterned SAM and the grey, patterned SAM. The chemical template features can be patterned by electron-beam lithography in a second write step, and provide a chemical contrast different from the unpatterned portion.

A high degree of overlay accuracy between these two writes is needed in order to achieve a combined-templating effect. If the two writes do not have a high degree of overlay accuracy, the physical and chemical templating features may not interact with the BCP in the way that they were designed. A lack of direction of the self-assembly may result, or worse, may reduce the coherence length of the self-assembled BCP thin film. Hence, an overlay accuracy of 10 nm was targeted for this work.

4.2 Investigation of Overlay

When two different patterns, denoted as the first write and the second write in Figure 4.2, are overlayed, there are a number of issues that can arise that decrease the accuracy. Translation, rotation, and dilation are the three most important. The first write includes the desired nanopatterns in the middle of the write area, as well as alignment markers on the left and bottom sides. The second write only includes the desired nanopattern in the middle of the write area. Figure 4.2a-d shows the first write and second write

with perfect overlay accuracy, a rotated overlay, a translated overlay, and a dilated overlay, respectively. For this chapter, translation and rotation were the most common overlay errors. Dilation was well controlled by the scanning-electron-beam system software on the Raith 150.

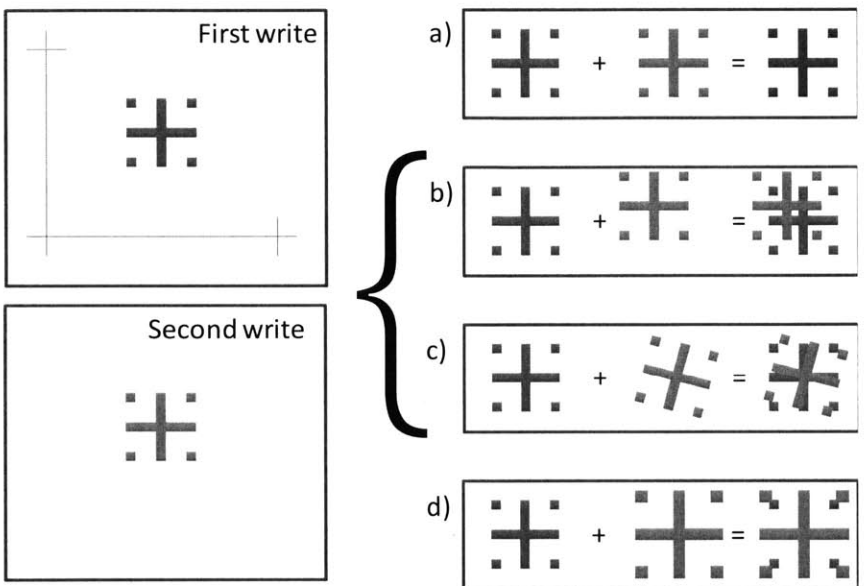

Figure 4.2: Schematics of the first and second write-patterns, and common overlay errors. On the left, the first write is shown in blue and the second write is shown in red. (a-d) depict the common overlay errors after the first and second writes are performed on top of each other. Each are (a) a perfect overlay with no error, (b) translational error in which the patterns are shifted in the same plane, (c) rotational error in which the patterns are rotated on a major axis, and lastly (d) dilation error in which one pattern is larger or smaller than the other.

4.3 Process Description

The process details of the overlayed nanopatterns are described below and are summarized in Figure 4.3. Generally, resist was spun on a bare Si wafer, lithographically patterned with the first write, developed, spun with a second layer of resist, the second write patterned in the new resist after aligning to makers on the first nanopattern, developed, and finally imaged.

For SEBL, a bare Si substrate was spun with a ~54 nm thick layer of hydrogen silsesquioxane (HSQ) with no post bake (2% in MIBK, 1000 rpm, 60 sec). This resist layer was patterned with the first write in a Raith 150 scanning-electron-beam-lithography (SEBL) system at 30keV with a current of about 275 pA

and linear-dose-density of 1 to 1.1 nC cm^{-1}. After exposure, samples were developed in a 4% NaCL / 1% NaOH salty developer solution at 24°C for 4 minutes, rinsed with deionized water for 2 minutes, and blown dry under N_2 flow[5]. A second, thinner, ~19 nm thick layer of HSQ was spun on the samples with no post bake (1% in MIBK, 5000 rpm, 60 sec). An iterative alignment process (detailed below) was performed with the SEBL system, and then the second write was exposed into this resist layer. The samples were developed in the same manner as after the first write, and imaged with the same Raith system (10keV, 30 μm aperture and 6 mm working distance). As is shown in Figure 4.3, the second HSQ spin was thinner than the first, and therefore the nanofeatures were also shorter. Furthermore, the second HSQ feature is shown in the middle of the first HSQ features. This work targeted perfect overlay, and therefore, this offset of the second HSQ feature is solely for this schematic.

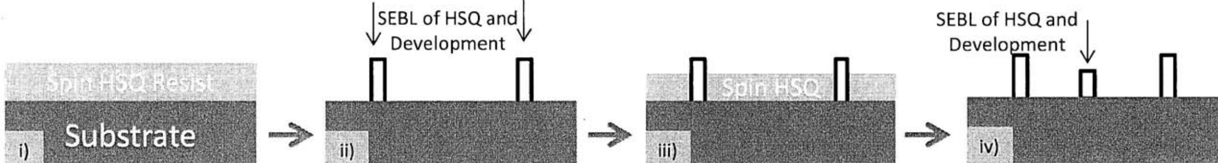

Figure 4.3: Major steps of the fabrication process. i) A prime Si Substrate is ii) spun with a ~54 nm thick layer of HSQ. iii) The first write by SEBL is performed and the sample developed in the salty developer. iv) Another layer of ~19 nm thick HSQ was spun over the first write patterns. v) Lastly, the second write by SEBL was performed, and the samples again developed in salty developer. After all the processing, the final patterns were imaged via SEM.

The first and second write were patterned with slightly different nanopatterns, and are shown in Figure 4.4. The patterns included lines and dots because these types of features are typically used as templates in BCP directed self-assembly. The lines were in a crossed mesh (1 μm long, 200 nm pitch), oriented in both the x- and y-directions. In each quadrant of these crosses were square arrays of dots (100 nm pitch, 3x3 μm arrays). The first write also included alignment markers of crossed-line features at the four corners of the write-field. For these writes, the dose was not varied and low enough to achieve small line and dot features (0- and 1-dimensional features).

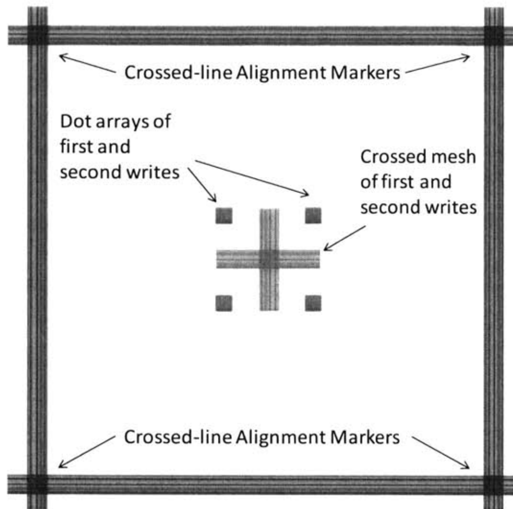

Figure 4.4: Snapshot of the design for the first and second writes. Noted are the crossed-line alignment markers around the edge of the write-field (first write only), and the crossed mesh patterns and dot array patterns of both the first and second writes.

The key steps of the overlay process on the Raith SEBL system such that the second write was overlayed to the first write (previously written and developed on the sample surface). This process included finding the first write-nanopattern in the scanning electron microscope (SEM), locating the alignment marker patterns (which were part of the first pattern), following iterative 3-point and write-field alignment processes, and then writing of the second write. Processes like current measurement, focusing, stigmating, and loading of design were carried out in the typical manner and not described below. All of the steps were performed in as quick succession as possible.

An iterative process of 3-point alignment and write-field alignment was developed to map the second write to the first write-nanopatterns. The bottom-left alignment crossed-line feature of the first write-nanopattern was located and the location recorded so it could be moved to later in the procedure. Write-field alignment (a typical step carried out for scanning-electron-beam lithography (SEBL) in the Raith 150) was performed for a 100 μm write-field. During this step, the imaging field used was the edge of a dried droplet of colloidal gold nanoparticles (acting as an imaging artifact, and located 150 μm from the first write). This point was also recorded so the location could be moved to later in the process steps. The

stage was then moved in succession to all three alignment points on the alignment marker, with the (X,Y,Z) and (U,V,W) coordinates of each recorded. The coordinate location of each point was determined by centering the SEM-screen crosshairs over the middle of the features. The 3-point alignment script was used in the Raith 150 software to align the Raith coordinate system (X,Y,Z) with the coordinate system of the first-write nanofeatures (U,V,W). A write-field alignment step was next performed at the gold colloid location, and then again a 3-point alignment step with the alignment features from the first write. These two alignment procedures (write-field and 3-point) were iterated many times (as is noted in the discussion below). Finally, the second write was written.

4.4 Results

The overlay process was poor early in the investigation, but improved as the investigation was carried out. Improvements to the process that were made include: 1) performing the whole overlay process at 30 keV instead of 10 keV (before switching to 30 keV for the second write), 2) the write-field alignment was included as the last step in the alignment process, not the 3-point alignment, and 3) the two alignment processes were iterated 10 times. With these improvements, the overlay error was reduced from ~14 μm of translation and 18° of rotation early in the investigation, to <50 nm of translation and about 0° of rotation late in the investigation. An example overlay is shown in the image in Figure 4.5 where the translation and rotation are large (about 4.15 μm and 18° respectively). Other examples are shown in Figure 4.6a-b, in which the translational and rotational error has been reduced to near 1 μm and about 0° respectively.

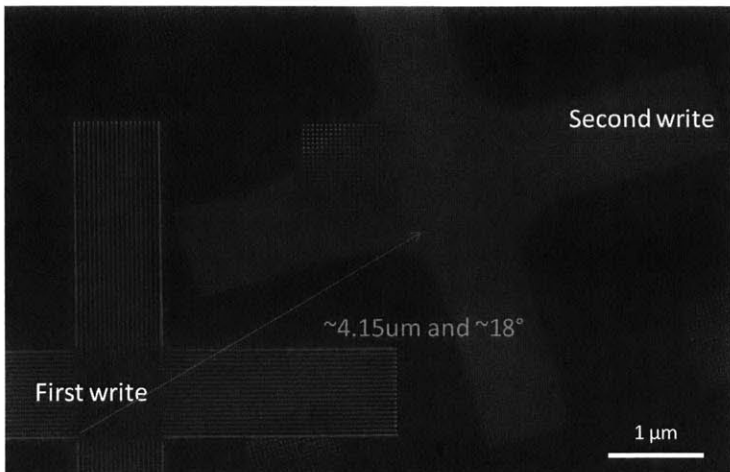

Figure 4.5: Top-down scanning-electron micrograph example of an overlay of the first and second write patterns in HSQ without process improvements. The crossed-line features at the bottom-left are from the first write and the top-right from the second write. Notably, the features, which are ideally on top of each other, are translated about 4.15 µm. Furthermore, the second write is rotated about 18° counter-clockwise from the first write. No dilation was noticeable. This is an example of many results from many samples in which the translation was >1 µm and rotation >0°. Also pictured are the dot arrays that were written in each of the 4 quadrants of the first and second writes.

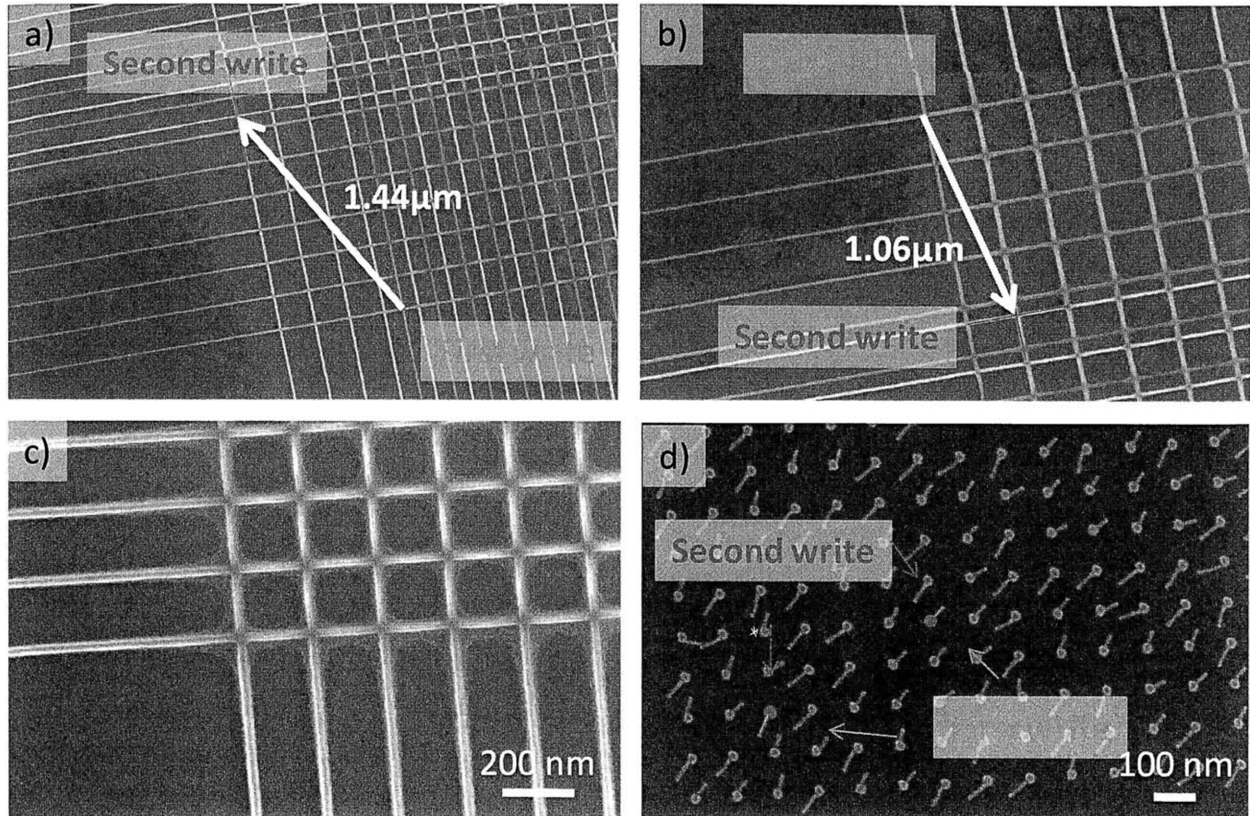

Figure 4.6: Top-down scanning-electron micrograph examples of overlays of the first and second writes in HSQ after process improvements. a) and b) show two example overlay patterns with close-ups of the crossed-lines portion of the nanopatterns. Intersections for the first and second writes are highlighted in green and red respectively. In these two examples, the process had been improved such that the overlay error was reduced to around 1 µm and the rotational error roughly 0°. c) and d) show an example of the same first and second write overlay in which the nanopatterns seem to be perfectly on top of each other. In c), only one set of crossed-line nanopatterns is observable, suggesting that the second write was on top of the first write. In d), the post features from the first write have fallen over due to capillary collapse. At the base of each post is another standing post feature from the second write. Therefore, it suggests that the second write was overlayed on the first write with no error.

After the process improvements, the final statistical characterization of the overlay error of the Raith 150 system was determined. Figure 4.6c-d shows nanopatterns from the first and second writes overlayed on the top of each other. From these images, the first and second writes are overlayed with ~0 nm of translational error. The overlay error was sampled 5 other times by completing all of the alignment process, and this perfect overlay was not henceforth observed.

The overlay errors were minimized to a large extent, but they were still far away from the 10-nm target for BCP templated self-assembly. The mean translational distance was determined to be 52 nm

(standard deviation of ~28 nm) and the mean rotational angle was determined to be <5°. Though these metrics are much lower than early experimental results, and low enough for typical overlay applications, they are not low enough for BCP templated self-assembly. In order to be applied to BCP templated self-assembly, the overlay error needs to be much smaller than the BCP L_0 (~35 nm). Furthermore, the direction of the translation and rotations was not consistent; the overlay error was considered to be a random error and nearing on the systematic limit of the Raith 150 SEBL system.

4.5 Conclusions

In conclusion, a process was determined to minimize overlay error and the overlay error was finally minimized. The alignment patterns used for 3-point alignment in the first write were determined to be adequate for the established process. Iterations of the alignment steps decreased the overlay error. After about 10 iterations, the absolute error saturated, and the overlay accuracy was largely determined by random error. Finally, ~50 nm accuracy was not high enough to use for combined physical and chemical templating for block copolymer directed self-assembly. It was speculated that a part of the 3-point alignment step was not adequate: the location of each of the three points was determined by positioning the crosshairs of the SEM over each of the alignment points. It would have been more accurate to image and determine the location of the alignment points with the Raith software itself (on the SEBL side, not the SEM side). This change was not made to the step, and therefore can be considered a future improvement. Another future improvement involves the use of the Elionix SEBL system which was recently installed at the Massachusetts Institute of Technology. This system has higher grid resolution and interferometric accuracy than the Raith 150 and therefore should result in better overlay accuracy.

References

1. Goodberlet, J. G., Hastings, J. T., & Smith, H. I. Performance of the Raith 150 electron-beam lithography system. *Journal of Vacuum Science Technology B Microelectronics and Nanometer Structures*, *19*(6), 2499 (2001).
2. Chang, T. H. P., Mankos, M., Lee, K. Y., & Muray, L. P. Multiple electron-beam lithography. *Microelectronic Engineering*, *57-58*, 117–135 (2001).
3. Choi, Y., Lindert, N., Xuan, P., Tang, S., Ha, D., Anderson, E., King, T., Sub-20nm CMOS FinFET Technologies. *IEEE International Electron Devices Meeting*, 00(100), 421–424 (2000)
4. Choi, Y.-K. C. Y.-K., Ha, D. H. D., King, T.-J. K. T.-J., & Hu, C. H. C. Nanoscale ultrathin body PMOSFETs with raised selective germanium source/drain. 22 IEEE Electron Device Letters 447–448 (2001).
5. Joel K. W. Yang and Karl K. Berggren, Using high-contrast salty development of hydrogen silsesquioxane for sub-10-nm half-pitch lithography. *Journal of Vacuum Science and Technology B,* 25, 2025 (2007).

Chapter 5: Sacrificial Templates PS-b-PDMS Self-Assembly

Templated self-assembly of BCPs, based on the results in the previous chapters, as well as previously published reports, has been able to produce nanopatterns with local complexity or long-range order[1-5]. Though these results are promising, the nanopatterns are typically not used directly in technology applications. When the nanopatterns are to be transferred to another material, different transfer characteristics of different materials in the nanopatterns have the potential to present a problem. Some of the areas of the nanopattern may permit faster pattern transfer than other areas, leading to a non-uniformity problem with the pattern transfer. Sacrificial templates have been applied to overcome this potential problem, though previous techniques did not show a wide variety of final BCP nanopatterns[6-9]. This chapter discusses a physical templating method with sacrificial posts that mitigates the pattern transfer problem and is capable of producing a wide variety of final BCP nanopatterns. The sacrificial-post templating method was shown as an effective means of: 1) increasing the long range order of the BCP, 2) developing locally complex nanopatterns, and 3) contributing to the understanding of how BCP self-assembles.

5.1 Prior work: DSA of PS-b-PDMS

Other researchers investigated different sacrificial-trench templating schemes with a variety of different BCPs. These approaches were able to direct BCP for long-range order and the templates were removed after annealing of the BCP, though complex local control, or 3-dimensional control, were not reported. Spherical PS-b-PFS BCP was templated by a template of BARLi ARC[6]. After removal of the BARLi ARC by O_2 reactive ion etch, the templated final BCP nanopattern remained behind. In order to template lamella PS-b-PMMA, a similar sacrificial-trench template scheme was used, though extended to template a second BCP thin film by the original BCP nanopattern[7]. With a related idea, BCP nanopatterns were

templated from a reusable, PDMS, trench template[8]. Although the sacrificial-trench templating method does not have the problem of nonuniform transfer characteristics, if patterning of a whole substrate is necessary, the method is limited by patternless regions (the regions that are covered by the trench mesa) or extra patterning steps.

5.2 Processing Steps

The main steps of the fabrication process are shown in Figure 5.1. Si samples were coated with a thin film of poly(methyl methacrylate) (PMMA) and the templating pattern was exposed by scanning-electron-beam lithography (SEBL). After development of the exposed samples, they were spin coated with PS-b-PDMS BCP. Cosolvent annealing of the BCP was performed in a solvent flow system. The PS-block and PMMA templating features were removed in a post-process reactive ion etch (RIE) before scanning-electron microscope (SEM) imaging.

For SEBL, a Si substrate was first spin-coated with 40 nm of PMMA (950K from MicroChem Corp, 1.8 PMMA:Anisol ratio, 4000 rpm) and baked for 2 minutes at 200°C to remove excess spinning solvent. SEBL was carried out in a Raith 150 system at 30keV. A large variety of template patterns were written with different pitches, lattices, and sizes. PMMA is typically positive tone resist, but this research overexposed the PMMA to use it as a negative-tone resist[10]. The local area near the highly-exposed pixels was cross-linked, and therefore remained behind after all development steps to serve as the templating features. The region in close proximity to the highly-exposed pixels was removed by development of MIBK for 2 minutes at room temperature, IPA rinse for 1 minute, drying under N_2 flow. Another step, used to remove the unexposed PMMA far from the highly-exposed pixels, included sonication in acetone for 2 minutes, rinsing with IPA for 1 minute, rinsing with deionized water for 1 minute, and blowing dry under N_2. PMMA is a negative tone resist.

Before depositing and assembly the BCP, the template samples were spin coated with a 1% short-chain PS-brush (1 kg mol^{-1}, Polymer Source from PGMEA (6000 rpm, 30 sec, 10 acceleration (a.u.)). The

attachment of the PS-brush was assisted by a 14-hour, 170°C thermal anneal, after which samples were soaked in toluene for 15 minutes. A 2% solution of PS-b-PDMS (M_w = 45.5 kg mol^{-1}, f_{PDMS} = 0.32, L_0 = 35 nm, Polymer Source) from PGMEA was then spin-coated on the samples. To achieve 2-dimensional nanopatterns, the BCP was spun to about 30 nm, and to achieve 2-dimensional (2D) nanopatterns, the BCP was spun to about 42 nm. The samples were annealed in a chamber with a 5:1 toluene:heptane saturated solvent vapor pressure for 1 hour (2D) or 1.5 hours (3D). After annealing, the samples were put through an RIE process. The top PDMS-layer was removed by a 5 sec CF_4 (50 W) etch, and the PS-block and PMMA templates were removed with a 22 sec O_2 (90 W) etch. Finally, the samples were imaged in the Raith 150 SEBL microscope at 10 keV, 30 μm objective aperture and 6 mm working distance.

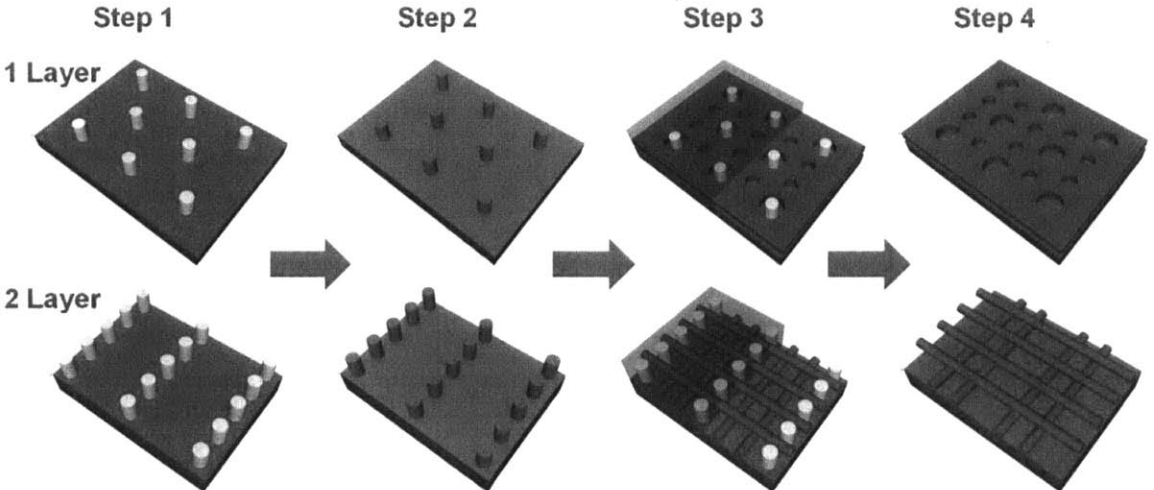

Figure 5.1: Major Steps of the fabrication process. Two different processes are shown for single and bilayers of BCP as a result of different thicknesses of BCP. The PMMA posts were first fabricated in a template lattice on the Si substrate surface. The template was coated with a PS-brush to assist self-assembly. Next, the PS-b-PDMS cylindrical BCP thin-film was spin-coated and annealed to results in self-assembled nanostructures. Lastly, a reactive ion etch was used to remove the PMMA template posts as well as the PS-block and leave behind the PDMS-block as the final BCP nanopattern.

5.3 PMMA Resist

The use of PMMA as a negative-tone resist, previously shown to crosslink under high electron-beam exposure to act as a negative-tone resist[10] was central to the sacrificial-post templating method. PMMA posts, shown in Figure 5.2a, were fabricated by exposing single points to high doses. The sacrificial

templates were arrays of such posts, arranged in a wide array of pitches, sizes, and lattices. The posts were measured to be 17 to 30 nm in diameter, and around 30 nm in height. When posts were exposed to O_2 reactive-ion etch, they were removed. PMMA posts are experimentally more likely to fall, as a result of capillary collapse, as oppose to HSQ posts. Studies have reported the controlled collapse of PMMA posts for nanofabrication[11]. In this work, capillary collapse, shown in Figure 5.2b, limited the fabrication of post templates to diameters larger than 17 nm.

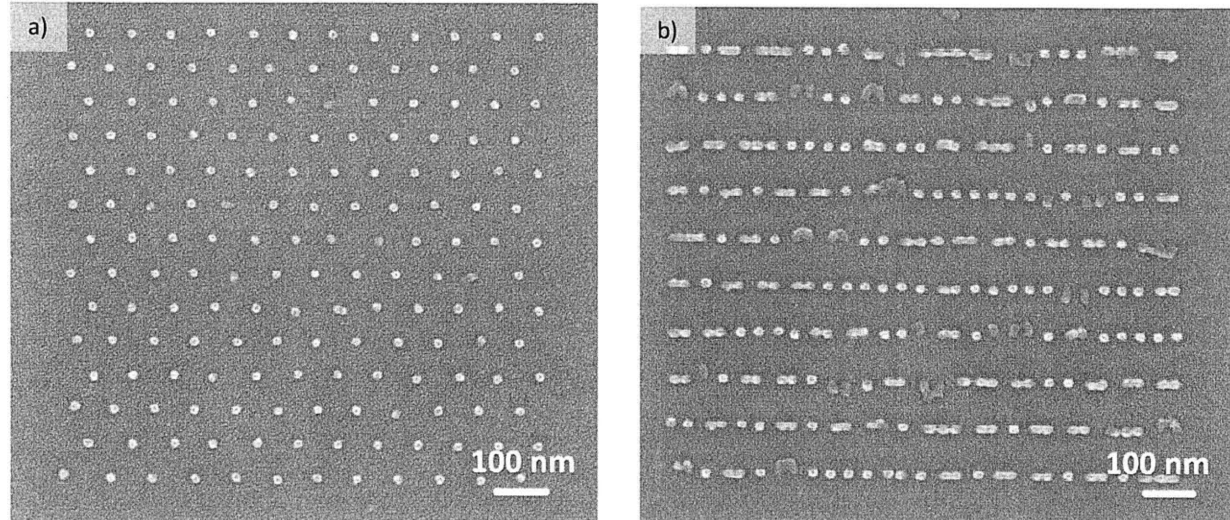

Figure 5.2: Top-down scanning electron micrographs of PMMA post features. A) PMMA posts are arranged in a hexagonal lattice on the Si substrate. B) PMMA posts were arranged in a rectangular lattice. Due to the high aspect ratio of the posts, many of them fell due to capillary collapse. This phenomenon limited the fabrication of smaller PMMA posts. In these images, the brighter spots are the posts and the darker background is the substrate. The samples were coated with a thin layer of Au/Pd to enhance imaging contrast and limit PMMA degradation while imaging.

In order to compare the sacrificial-post templating method with other common templating techniques, an array of BCP nanoholes templated by hydrogen silsesquioxane (HSQ) posts is shown in Figure 5.3a. In this example, the PDMS-domain is repelled by the templating posts, and therefore forms a network of nanoholes. If the shown pattern were to be transferred to another material, the PDMS layer and HSQ nanoposts would etch at different rates, and there provide nonuniformity in the transferred material. Figure 5.3b shows a similar BCP, though without the HSQ posts. In this example, PMMA, sacrificial

posts were used to template the BCP nanopattern, and subsequently removed in the RIE process. The PDMS-block is the single material to be used for pattern transfer, and therefore may results in more uniform etching.

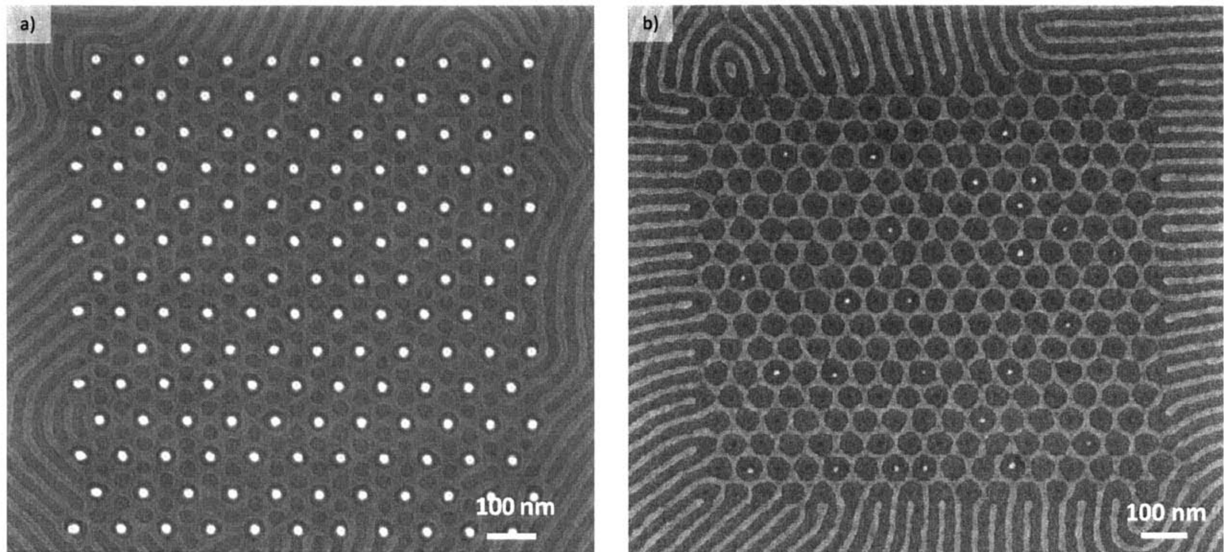

Figure 5.3: Top-down scanning electron micrograph of a final BCP nanopattern from hexagonal post template arrays. a) with the sacrificial-post templating method. The PDMS-block is templated to for nanoholes in a hexagonal array. The posts used for this templating are no longer present, and therefore the final nanopattern is comprised of a homogenous material. B) with a conventional post templating method. The PDMS-block is templated to form nanoholes in a hexagonal array. The posts used for this templating remain behind and occupy the middle of some of the nanoholes. Therefore the final nanopattern is not comprised of a homogenous material. In this image, the white, light grey and darker grey regions are HSQ resist posts, PDMS-block and substrate respectively.

5.4 Templating for 2D Nanostructures

A large variety of final PS-b-PDMS BCP nanopatterns were generated by the sacrificial-post templating method. These patterns are separated into two categories, 2D and 3D patterns, as a result of different thicknesses of BCP. For 2D, arrays of nanoholes, nanodots, and generated nanoholes were fabricated, and are shown in Figure 5.4 and 5.5. Nanohole arrays were fabricated with posts in square (Figure 5.4a) (90-734 fC dot^{-1}, x-pitch = 52-29 nm, y-pitch = 46-64) and hexagonal lattices (Figure 5.5) (90-954 fC dot^{-1}, pitch = 48-74 nm). The diameter of the nanoholes scaled with the dot dose used to write each templating post. Nanodot arrays were fabricated with posts in square lattices (Figure 5.4b) (90-734 fC dot^{-1}, x-pitch =

41-50 nm, y-pitch = 36-47 nm). In Figure 5.4(c-d), arrays of post-holes and generated-holes are shown. Posts were fabricated in square (Figure 5.4c) (152-734 fC dot^{-1}, pitch 65-72 nm) and hexagonal (Figure 5.4d) (198-1613 fC dot^{-1}, pitch = 80-92 nm) arrays, but with a larger pitch than in Figure 5.4a. Post-holes were formed around each of the posts, and generated-holes were formed in between the posts. In these cases, the number of final nanohole per templating post was 2 and 3 times, for the square and hexagonal arrays respectively. Furthermore, a wide variety of other morphologies were observed in Figure 5.6. These included elliptical nanodots (Figure 5.6a) (734-1241 fC dot^{-1}, pitch = 44-51 nm), periodic superstructure (Figure 5.6b) (90-434 fC dot^{-1}, x-pitch = 50-59 nm, y-pitch = 36-39 nm) and line gratings (Figure 5.6c) (pitch = 36-46 nm).

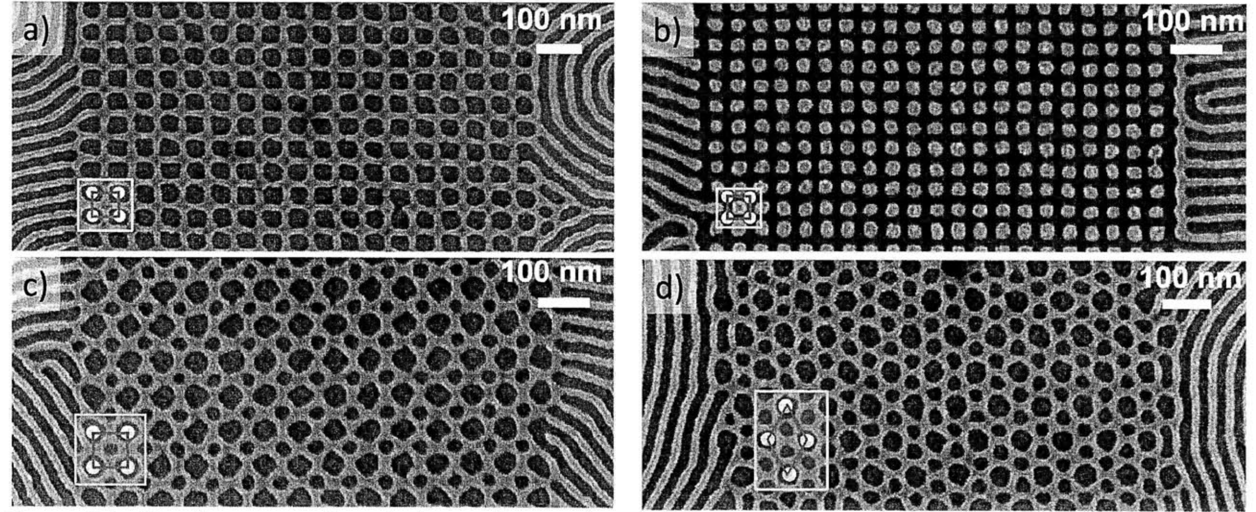

Figure 5.4: Top-down scanning electron micrographs of different 2D nanopatterns formed by the sacrificial-post templating method. All of these images show the final BCP nanopattern where the original posts have been removed by RIE. a) A square array of nanoholes in which each templating post resulted in a single nanohole (post-hole). (734 fC/dot, x-pitch = 67 nm, y-pitch = 64 nm) b) A square array of spherical dots in which the stress of closely-spaced posts forced the BCP to break into individual nanofeatures instead of a mesh. (434 fC/dot, x-pitch = 42 nm and y-pitch = 41 nm) c) A square array of nanoholes in which each templating post resulted in two nanoholes (a post-hole and generated-hole). (734 fC/dot, pitch = 72 nm) d) A hexagonal array of nanoholes in which each templating post resulted in three nanoholes (a post-hole and two generated-holes). (954 fC/dot, pitch = 88 nm) The lighter and darker grey regions represent the PDMS-block and substrate respectively.

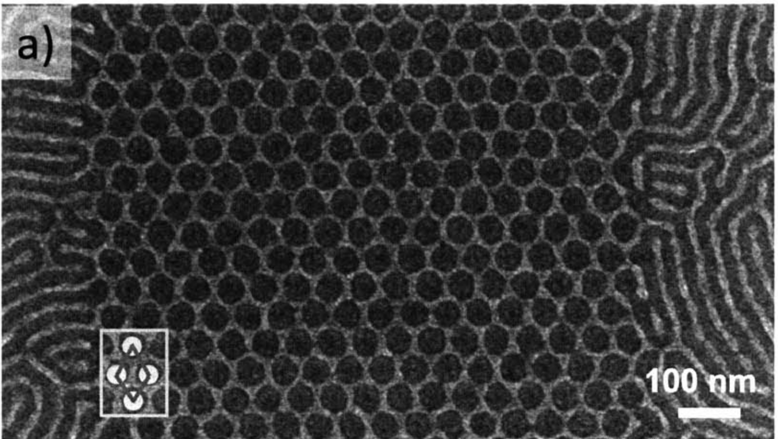

Figure 5.5: Top-down scanning electron micrograph of hexagonal array of nanholes formed by the sacrificial-post templating method. (954 fC/dot, pitch = 60 nm) All of these images show the final BCP nanopattern where the original posts have been removed by RIE. The image shows a hexagonal array of nanoholes in which each templating post resulted in a single nanohole (post-hole). The lighter and darker grey regions represent the PDMS-block and substrate, respectively.

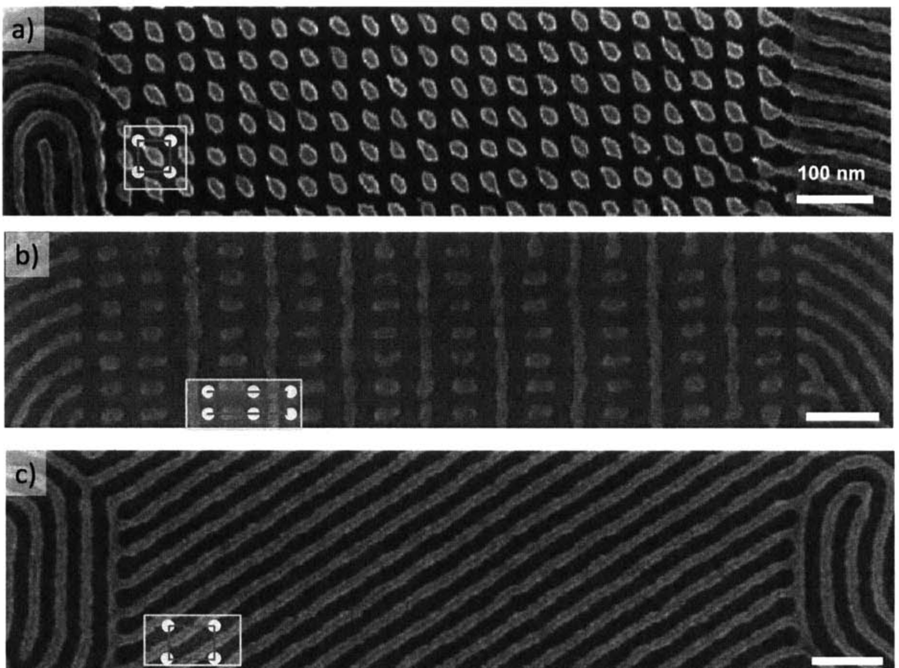

Figure 5.6: Top-down scanning electron micrographs of different 2D nanopatterns formed by the sacrificial-post templating method. All of these images show the final BCP nanopattern where the original posts have been removed by RIE. a) A square array of elliptical dots in which each templating post resulted in a single dot. (post 954 fC/dot, pitch = 44 nm) b) A periodic superstructure of lines and dots templated by a rectangular array of templating posts. (257 fC/dot, x-pitch = 54 nm and y-pitch = 39 nm) c) A grating of lines templated by a hexagon array of templating posts. (2481 fC/dot, pitch = 60 nm) Lighter and darker grey regions represent the PDMS-block and substrate respectively.

As was noted above, the size of the holes can change as the size of the posts change and for the generated-hole arrays, this relationship was analyzed. A Matlab program was used for image processing, and the size of each post-hole, generated-hole, and post was determined (in this work, HSQ posts were analyzed, but the results can be applied to PMMA posts as well). The resulting data is presented in the graph in Figure 5.7. The process used for this image analysis is shown in Figure 5.8 and described in the caption. Notably, the diameter of post-holes scales with the diameter of template posts, whereas the diameter of generated-holes remains about constant as a function of template-post size. It is possible that the generated-holes do not increase in size because they are bound by the natural pitch length (L_0) of the PS-b-PDMS BCP. Furthermore, the perimeter of the post-hole is likely a constant distance from the perimeter of the templating post, and therefore the post-hole's diameter scales with the templating post's diameter. These relationships were found to be the case over the full range of the tested templating post diameters. Also, the same relationship was found for post- and generated-hole versus templating post pitch. The size of the post- and generated-hole versus interpost distance was not determined, and in conclusion may have been a better metric for this investigation.

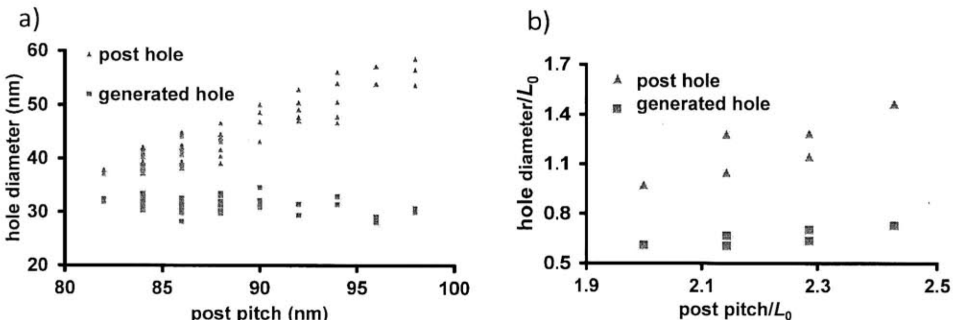

Figure 5.7: Graph of nanohole diameter versus post diameter and pitch. A) Post-hole and generated-hole diameter vs. post diameter. B) post-hole and generated-hole diameter vs. post pitch.

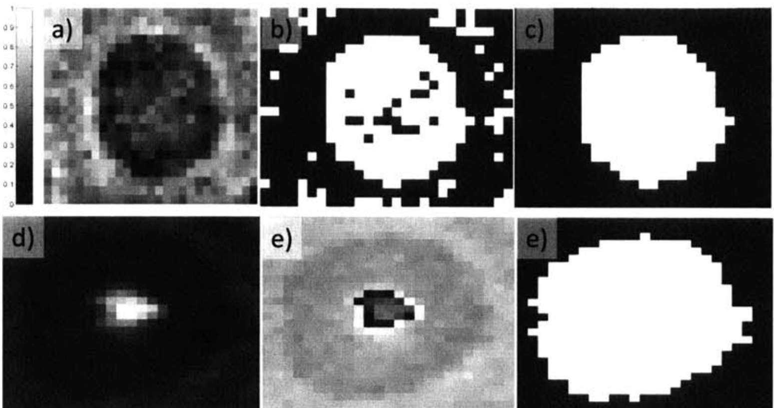

Figure 5.8: Examples of Matlab steps for determining the size of a-c) generated-holes and d-f) post-holes. a) SEM image of a generated-hole as determined by Matlab program. Pixel values are scaled for 1 to 0, where 0 is dark for the hole. b) Binary image of the hole generated from statistical clustering, where a value of 1 indicates potential hole-pixels. c) Morphological operations used to select the hole-only pixels. From this image, the area of the hole was determined. d) SEM image of a post-hole as determined by Matlab program. Pixel values are scaled for 1 to 0, where 1 is light for the post. e) The post is determine, and subtracted from d). f) Binary image of the post-hole as determined by statistical clustering and morphological operations. From this image, the area of the hole was determined.

It should be noted that most of these final BCP nanopatterns were previously reported, but it is important to show that they can similarly be fabricated with the sacrificial-post templating method[13]. The PS-b-PDMS BCP was cylindrical morphology in bulk, but these varying templates induced varying morphologies. The discussion on this difference was also previously discussed. Most interesting for this work was the fabrication of different size post-holes. The nanoholes in Figure 5.4a and (c-d) could vary in diameter as was previously discussed. Therefore, including different templates on a single substrate may allow for the fabrication of a wide variety of nanopatterns, including different morphologies as well as different nanofeatures sizes.

With regards to the repeatability of the fabrication of the PMMA templates, two important considerations were found: the removal of the unexposed PMMA and the etching of the final PMMA pattern. During the resist development step of the fabrication process, samples were sonicated in acetone. This removed the unexposed PMMA far away from the templated regions. Without this removal, the following spinning of the BCP was not uniform. Also, high-dose PMMA posts required longer O_2 RIE to

be fully removed. Examples of incomplete removal of the PMMA posts were observed for many templates with very high exposure dose.

5.5 Templating for 3D Nanostructures

For 3D nanopatterns, meshes of nanoholes fabricated with rectangular arrays of PMMA posts (pitches and doses) are shown in Figure 5.9. These nanoholes are formed by the crossing of two gratings of cylinders, the first in the y-direction and the second in the x-direction (where the first is on the bottom and the second is on the top). The crossing of these two gratings fabricates rectangular lattices of rectangularly-shaped 3D nanoholes. In cases when the x-pitch was 60-85 nm and dose was 257-565 fC dot^{-1}, nanoholes were fabricated in the same position as each PMMA post as is shown in Figure 5.9a. In cases when the x-pitch was larger, 99-110 nm, and dose was 117-434 fC dot^{-1} nanoholes were fabricated in the same positions as each PMMA post (post-holes), and also extra nanoholes was fabricated in between each post (generated holes) (Figure 5.9b). This generation of nanoholes in between posts is similar to the case for 2D nanoholes in Figure 5.4(c-d).

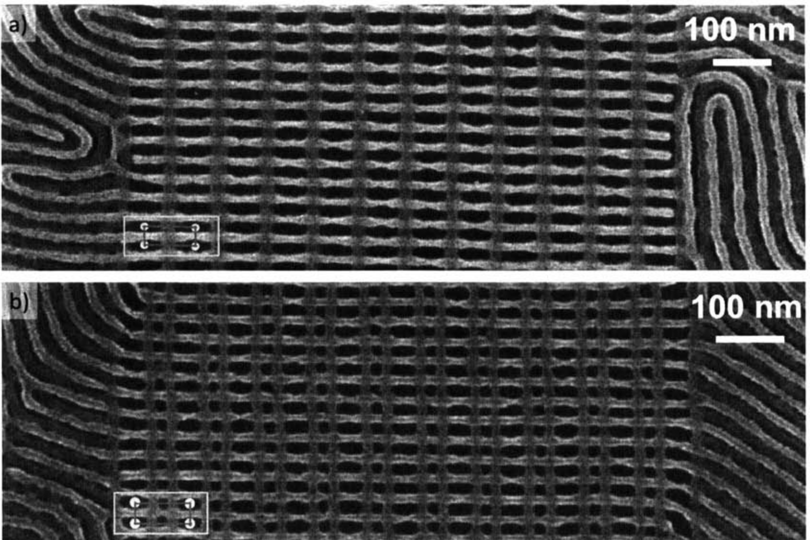

Figure 5.9: Top-down scanning electron micrographs of 3D nanoholes meshes templated by the sacrificial-post templating method. All of these images show the final BCP nanopattern where the original posts have been removed by RIE. a) A square array of rectangular nanoholes in which each templating post resulted in a single nanohole (post-hole). (x-pitch = 83 nm and y-pitch = 37 nm) b) A square array of rectangular nanoholes in which each templating post resulted in two nanoholes (a post-hole and generated-hole). (x-pitch = 96 nm and y-pitch = 36 nm) The lighter and darker grey regions represent the PDMS-block and substrate respectively.

The size of the nanoholes was not statistically determined as was the case with the 2D nanoholes. Generally, the x-direction size of the holes increased with the x-pitch of the template. The y-pitch of the templates didn't vary significantly, and therefore neither did the y-direction hole size. The generated-holes were smaller than the post-holes and didn't change size significantly with varying template pitches.

5.6 Conclusions

In conclusions, a variety of nanopatterns were fabricated with the sacrificial-post templating method. Most notably, nanoholes arrays were fabricated in both 2D and 3D. In extension, the size of different nanoholes can be controlled by varying the templating post size or pitch. Fundamental to the process, PMMA posts, which are removable post-process, function similarly to HSQ posts for the templating of BCP self-assembly. This allows for the fabrication of a large variety of different nanopatterns that have not been shown by other sacrificial templating methods. After post-process removal, only the PDMS-block remains as the final BCP nanopattern. This homogenous pattern mitigates any potential pattern

transfer problems. This method has potential for functional nanopatterns in the technologies of bit-patterned media, water filtration, via fabrication in the semiconductor industry, photovoltaics, and virus filtration[14-16].

References

1. Sang Ouk Kim, Harun H. Solak, Mark P. Stoykovich, Nicola J. Ferrier, Juan J. de Pablo & Paul F. Nealey, Epitaxial self-assembly of block copolymers on lithographically defined nanopatterned substrates. *Nature* 424, 411-414 (2003).
2. Joel K. W. Yang, Yeon Sik Jung, Jae-Byum Chang, R. A. Mickiewicz, A. Alexander-Katz, C. A. Ross and Karl K. Berggren, Complex self-assembled patterns using sparse commensurate templates with locally varying motifs.*Nature Nanotech.* 5, 256-260 (2010).
3. Ion Bita, Joel K. W. Yang, Yeon Sik Jung, Caroline A. Ross, Edwin L. Thomas, and Karl K. Berggren, Graphoepitaxy of Self-Assembled Block Copolymers on Two-Dimensional Periodic Patterned Templates, *Science* **321**, 939 (2008).
4. Park, S., Lee, D. H., Xu, J., Kim, B., Hong, S. W., Jeong, U., Xu, T. Macroscopic 10-terabit-per-square-inch arrays from block copolymers with lateral order. *Science*, *323*(5917), 1030–1033 (2009).
5. Ruiz, R., Kang, H., Detcheverry, F. A., Dobisz, E., & Kercher, D. S. Density multiplication and improved lithography by directed block copolymer. *Science,* 321, 936-939 (2008).
6. Ilievski, F., & Ross, C.A. Graphoepitaxy of block copolymers using selectively removable templates. *Journal of Vacuum Science & Technology B: Microelectronics and Nanometer Structures*, *28*(1), 42 (2010).
7. Moon, H.-S., Shin, D. O., Kim, B. H., Jin, H. M., Lee, S., Lee, M. G., & Kim, S. O. Large-area, highly oriented lamellar block copolymer nanopatterning directed by graphoepitaxially assembled cylinder nanopatterns. *Journal of Materials Chemistry*, *22*(13), 6307 (2012).
8. Wang, C., Mao, Y., Wang, D., Qu, Q., Yang, G., & Hu, X. Fabrication of highly ordered microporous thin films by PS-b-PAA self-assembly and investigation of their tunable surface properties. *Journal of Materials Chemistry*, *18*(6), 683(2008).
9. Jae Won Jeong Woon Ik Park Lee-Mi Do Jong-Hyun Park Tae-Heon Kim Geesung Chae Yeon Sik Jung, Nanotransfer Printing with sub-10 nm Resolution Realized using Directed Self-Assembly. *Advanced Materials*, 24(26) 3526–3531 (2012).
10. Huigao Duan, Donald Winston, Joel K. W. Yang, Bryan M. Cord, Vitor R. Manfrinato, and Karl K. Berggren, Sub-10-nm Half-Pitch Electron-Beam Lithography by Using PMMA as a Negative Resist, *Journal of Vacuum Science and Technology B,* 28, C6C58-C6C62 (2010).
11. Huigao Duan and Karl K. Berggren, Directed Self-Assembly at the 10 nm Scale by Using Capillary Force-Induced Nanocohesion. *Nano Letters* 10(9), 3710-3716 (2010).
12. Huigao Duan, Donald Winston, Joel K. W. Yang, Bryan M. Cord, Vitor R. Manfrinato, and Karl K. Berggren, Sub-10-nm Half-Pitch Electron-Beam Lithography by Using PMMA as a Negative Resist. *Journal of Vacuum Science and Technology B*, 28, C6C58-C6C62 (2010).
13. Amir Tavakkoli K. G. ,Adam F. Hannon, Kevin W. Gotrik, Alfredo Alexander-Katz, Caroline A. Ross, Karl K. Berggren, Rectangular Symmetry Morphologies in a Topographically Templated Block Copolymer, 24(31), 4249–4254 (2012).
14. Hamm, S. *Business Week* 2007, IBM's chip breakthrough
15. Jackson, E. A., Hillmyer, M. A. Nanoporous membranes derived from block copolymers: From drug delivery to water filtration. *ACS Nano*, 4, 3548–3553 (2010).
16. Yang, S. Y., Park, J., Yoon, J., Ree, M., Jang, S. K., Kim, J. K. Virus filtration membranes prepared from nanoporous block copolymers with good dimensional stability under high pressures and excellent solvent resistance, *Adv. Funct. Mater.,* 18, 1371–1377 (2008).

Appendix I – Contrast Measurement of Neon-Ion-Beam-Lithography with Hydrogen Silsesquioxane

Particle-beam-lithography is a common tool for top-down nanofabrication, and has been highly employed in many applications such as optical-lithography mask inspection and research development of nanoelectronic devices. While scanning-electron-beam-lithography was predominantly used in this thesis, this appendix outlines the investigation of neon-ion-beam-lithography (NIBL) as a new method for high-sensitivity and resolution top-down nanofabrication.

A.1 Background

Particle-beam-lithography has been researched in the form of electron- and ion-field-lithography, scanning-electron-beam-lithography, and scanning-ion-beam-lithography. In particular, ion-beam-lithography with He^+ and Ga^+ have common with the introduction of commercial systems. A helium microscope with a gas-field-ionization source (GFIS) (Zeiss Orion) was adapted to accelerated Ne^+ particles instead of helium[1]. Neon has a higher atomic mass, and therefore should achieve a higher lithographic sensitivity than helium[2]. This new microscope was used to investigate NIBL and this chapter outlines some of the results from the original report by Winston et.al.[3].

A.2 Results

In this experiment, the contrast curve of NIBL for HSQ was determined for dose densities of about 8.5-50 $\mu C\ cm^{-2}$. A prime Si sample was spin-coated with HSQ with a thickness of 20 nm. The adapted Zeiss Orion helium-ion-microscope was used to expose ~1 μm^2 pads at a 3 μm spacing (20 keV, 10 μm aperture, 0.3 pA). After exposure, the samples were developed with a salty developer (4% NaCl / 1% NaOH in deionized water) at 24°C for 4 minutes, then rinsed with deionized water for 2 minutes and blown dry

under N_2. HSQ is a negative-tone resist and therefore the unexposed resist is removed by the developer solution.

After development, the height of the pads was measured by atomic-force microscopy (AFM) (Digital Instruments D3000). Full pad-size micrographs were taken, leveled, and the pad-height averaged for each exposed feature. Examples of a micrograph, height profile graph, and height profile metric are shown in Figure A1(a-c).

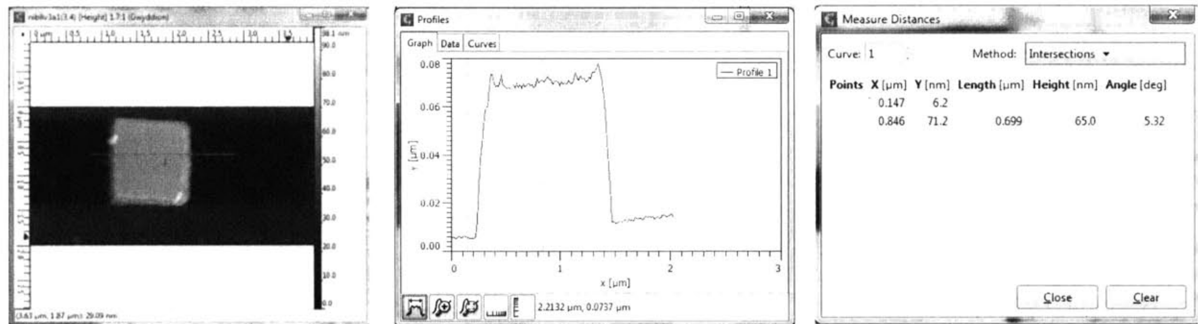

Figure A1: Measurements of the height of HSQ remaining for an example pad feature. a) AFM image of a pad (light gold in the middle), leveled such that the substrate (dark background) is considered to be at a height of 0 nm. b) A height profile along the line in the image in (a). c) A single-point measurement of the HSQ remaining based on the profile in (b). Gwydion software was used for all image processing and post-AFM measurements. Height metrics were an average of the measured height over the whole pad area.

The height of the remaining HSQ was obtained for each HSQ pad on the same substrate. The measured heights scaled with the delivered areal-dose-density as is shown in Figure A2. An onset areal dose of ~10 µm cm^{-2} was observed, noted as less than 1 ion nm^{-2}.

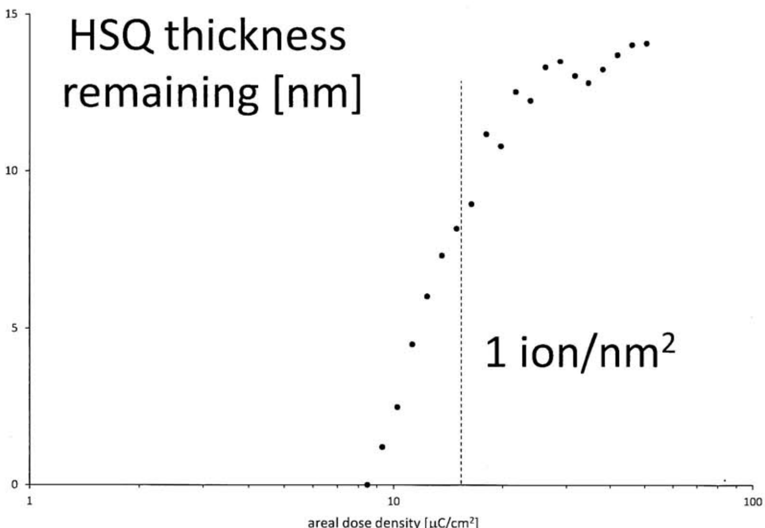

Figure A2: Height of HSQ remaining as a function of areal dose density. For each pad, the height of the HSQ remaining was determined (nm) and plotted as a function of the areal dose density ($\mu C/cm^2$) delivered to that pad. The onset dose was determined to be less than 1 ion nm^{-2}.
Figure from: "Neon Ion Beam Lithography (NIBL)," Donald Winston , Vitor R Manfrinato , Samuel M Nicaise , Lin Lee Cheong , Huigao Duan , David Ferranti , Jeff Marshman , Shawn McVey , Lewis A Stern , John A Notte , and Karl Berggren. *Nano Letters* **11**(10) 4343-4347(2011). © 2011 American Chemical Society

A.3 Discussion

The onset dose was found to be lower than many other scanning-particle-based lithography methods. Similar exposures by 30 keV helium ions or 5 keV electrons would require ~2x[4] and 50x[5] higher dose, respectively This results was enabled by the high brightness of the neon GFIS ($B > 4x10^9$ A cm^{-2} sr) focusing to a sub-nm spot size[6]. Furthermore, the stopping power of the neon ions, (230 eV nm^{-1}), over 3x higher than 30 keV helium ions and 50x higher than 5 keV electrons.

A.4 Summary

The fabrication of nanoscale HSQ pads was accomplished by NIBL with the new neon-adapted Zeiss Orion. The height of the remaining HSQ resist for varying areal dose densities was measured by AFM. These measurements were plotted, and the sensitivity of the method was determined to be less than

1 ion nm^{-2}. This sensitivity is higher than both scanning-electron-beam lithography and scanning-helium-ion-lithography. As this system is commercialized, further investigation of lithography will be investigated. Furthermore, at high sensitivities, this system may enable fundamental research on the limits of shot-noise in lithography and imaging.

References

1. Tan, S., Livengood, R., Shima, D., Notte, J., & McVey, S. Gas field ion source and liquid metal ion source charged particle material interaction study for semiconductor nanomachining applications. *Journal of Vacuum Science and Technology B: Microelectronics and Nanometer Structures*, 28(6), C6F15 (2010).
2. Ziegler, J. F., Ziegler, M. D., & Biersack, J. P. SRIM – The stopping and range of ions in matter (2010). *Nuclear Instruments and Methods in Physics Research Section B: Beam Interactions with Materials and Atoms*, 268(11-12), 1818–1823 (2010).
3. Winston, D., Manfrinato, V. R., Nicaise, S. M., Cheong, L. L., Duan, H., Ferranti, D., Marshman, J., Neon Ion Beam Lithography (NIBL). *Nano Letters*, 11(10), 4343–4347 (2011).
4. Sidorkin, V., van Veldhoven, E., van der Drift, E., Alkemade, P., Salemink, H., & Maas, D. (2009). Sub-10-nm nanolithography with a scanning helium beam. *Journal of Vacuum Science & Technology B: Microelectronics and Nanometer Structures*, 27(4), L18.
5. Yang, J. K. W., & Berggren, K. K. Using high-contrast salty development of hydrogen silsesquioxane for sub-10-nm half-pitch lithography. *Journal of Vacuum Science & Technology B: Microelectronics and Nanometer Structures*, 25(6), 2025 (2007).
6. Ward, B. W., Notte, J. a., & Economou, N. P. Helium ion microscope: A new tool for nanoscale microscopy and metrology. *Journal of Vacuum Science & Technology B: Microelectronics and Nanometer Structures*, 24(6), 2871 (2006).